Performance of Wide Band Gap Switching Devices in DC/DC Converters of Electric Vehicles

By

Yosra Attia

A Thesis Submitted in Partial Fulfillment

of the Requirements for the Degree of Master of Science

in

Electrical, Computer, and Software Engineering

Faculty of Engineering and Applied Science

University of Ontario Institute of Technology

Oshawa, Ontario, Canada

Yosra Attia

© October 2016

Abstract

Low losses fast switching wide band gap (WBG) semiconductors, such as Gallium Nitride (GaN) and Silicon Carbide (SiC), are becoming viable candidates for DC/DC converters switches in the powertrain of electric vehicle (EV). Thanks to the technology advancements, WBG power transistors are available now in the market with competing loss levels. In this research, the need for such devices to boost the system efficiency for extended vehicle mileage is justified. Case studies comparing the performance of the available options are presented, for the first time. The performance, motoring and regenerative braking, is studied at different junction temperatures. The results reported higher power density and increased car mileage using WBG semiconductors. These findings were consistent in automotive Nissan Leaf electric vehicle (NLEV) case and a Bombardier metro rail car, to provide the authentication of the developed plug-and-play model. Simulation and Experimental results were given to highlight the merits of the work.

key words: *Electric vehicles, WBG semiconductors, GaN on Si cascode, SiC ACCUFET, hybrid module, SiC Schottky barrier diode, bidirectional DC/DC converter, PMSM, MTPA, field weakening, powertrain, switching losses, conduction losses, conversion efficiency.*

Acknowledgements

I thank God the most merciful, for the success of this thesis.

I attribute the success of this research to the guidance of my supervisor Prof. Mohamed Youssef, who inspired me to complete the thesis with correctness and consistency.

The support of my family is beyond words. I owe my life for my family; parents, husband, siblings and children. Also, I am really grateful for all my friends who supported the success of this thesis.

Finally, I would like to express my gratitude to the UOIT for the proper study environment that it provides.

TABLE OF CONTENTS

List of Tables

List of Figures

Chapter 1 : Introduction

Electric vehicles (EV) industry is currently in the pace of revolutionary advancements. The market is flooded by many new manufacturers; like Tesla, Ford, Chevrolet, and even Google. This trend puts a lot of pressure on the electric grid due to the huge power demand of these cars. The real race nowadays is to cut short on the energy consumption of these cars. There is a relentless effort from the researchers around the globe to work on this issue. Also, batteries are one of the main components of the EV that have gone through a great deal of development during the last decade. However this topic seems to get stabilized and frozen as companies like Tesla and google buyout the whole supply of Lithium Ion (Li-ion) of the globe, which means there is no expectation for a better alternative from now-on. Also, advancements in the traction motor's structure and energy efficient control techniques is stabilized.

1.1 Background and Motivation

Better EV performance can be achieved through better component efficiency. There is no better candidate in EV than the DC/DC converter in the powertrain to achieve efficiency gain. It is an important stage between the battery and the motor DC link bus of the EV. The DC/DC converter is alive as long as the car is moving; working whether motoring or braking; its efficiency, size, and power density are critical for a better EV performance. This converter boosts the battery voltage in motoring mode. In the regenerative mode of braking, it returns energy back into the battery thus a bidirectional converter is needed. The power density of the DC/DC converter can be made higher through reductions in its power loss and weight. In a hybrid electric vehicle (HEV) system, power conversion unit (PCU) loss represents 20% approximately of the total powertrain loss. For EV, this percentage is higher. Reducing this loss can dramatically improve efficiency [1]. Lower converter's power losses will not only maximize the power transfer, but also decreases size and weight of the heat sink required for converter cooling. This way, the power density of the converter can be improved. DC/DC converters have plenty of topologies, there are more than 500 topologies of power DC/DC converters existing. All existing prototypes of the power DC/DC converters are categorized into six generations [2,

3]. Many topologies were already investigated to improve the power density and efficiency of the boost converter. Therefore, the development in the topology is saturated and is not the candidate for power density improvement. A key point in the design of the EV DC/DC converter is the selection of the material and structure of the switch to reduce the losses, both conduction and switching, for the same frequency and even higher frequencies. Present power semiconductor EV converters are all made of Si. But now, the performance of Si power devices is approaching its limit due to physical properties, energy bandgap, and we cannot expect dramatic development in Si power devices [4].

In order to assess available switching options, the study starts, by choosing the right system parameters, surveying the market for the most advanced candidate switching peers, followed by system calculations and simulation, during which the maximum switching frequency is determined according to the thermal dissipation limits. Then, converter's switching efficiency is calculated and compared for each WBG option. In addition, heat sink size reduction is estimated, while reducing filter components size as a result of the high frequency switching. Finally, the best switching selection is nominated based on the previous mentioned comparison.

The ultimate goal of this thesis is to highlight the merits of WBG materials for converter switching within the EV powertrain. WBG materials combined with advanced semiconductor structures are expected to result in extended mileage for EVs with huge energy and cost savings. While many studies investigated the high voltage WBG power transistors performance as seen in the literature. However, this work presents, for the first time, the utilization of WBG devices, GaN E-HEMT cascode and SiC Trench MOSFET, for the high power high voltage application of DC/DC converter for EV powertrain.

GaN on Si Enhanced mode High-Electron-Mobility-Transistor (E-HEMT) cascode switches is the most advanced technology in GaN devices whereas SiC Trench MOSFET is the counterpart in SiC devices. Another competitor is the hybrid module that utilizes a SiC Schottky barrier diode (SBD) anti-parallel to the traditional used Si IGBT. Alternatively, low loss automotive qualified Si MOSFET is an option included in the comparison.

Device I under comparison in this study is a GaN E-HEMT cascode in one package. It incorporates a normally-off low-voltage (LV) Si MOSFET at the input and a normally-on high-voltage (HV) GaN HEMT at the output in a cascode configuration. Device II is a SiC accumulated gate field effect transistor (ACCUFET) MOSFET that belongs to the family of SiC Trench power MOSFETs produced for the first time in 2015. This group is designed for high frequency high power ultra-low loss applications. Device III is a hybrid module. It consists of a Si IGBT with anti-parallel SiC SBD to cut the tail current from the IGBT and reduce diode recovery loss substantially. Device IV is a traditional power MOSFET belongs to the series of low loss Si automotive qualified technology with integrated fast body diode.

The switching characteristics of WBG materials semiconductors, mainly GaN and SiC, allow power electronic engineers to benefit from lower switching losses and higher switching frequencies. These benefits permits the flexibility to use the same switching frequency while increasing converters efficiency, or to increase the switching frequency and minimize the size, weight and cost of inductive and capacitive components [5]. Using these WBG low losses fast switching switches, will result in low both conduction and switching losses. These WBG devices are the current viable candidate for better EV power density, mileage and energy costs. Using GaN-on-Silicon Enhanced mode High-Electron-Mobility-Transistor (GaN on Si E-HEMT), 99% 1:2 boost efficiency at 100 kHz could be achieved for computer power supplies. Low On-resistance, low reverse recovery charge and high switching speed contributed to this high efficiency as reported by Fujitsu semiconductors [6]. A case study of a 1-MW motor drive for a shipboard in [7] showed that SiC based inverter could reduce the device loss to 30% and cooling system size to 15% of the counterpart Si based design. With the shrinking cost gaps and enhanced reliability, analysts predict that WBG devices will replace Si in mainstream applications in the 600 to 1700 V range in the next five years onward [8]. WBG materials offer greater efficiency in operating the electric traction drive during vehicle use. The fact that these semiconductors can reduce power losses contribute to reduction in the size of an automotive cooling system by 60% or even eliminate the secondary liquid cooling system [9]. The following paragraph provide a glimpse about WBG switches history and characteristics. After that, the WBG devices under study in this research are introduced.

1.2 History and characteristics of WBG Devices

History of semiconductors began around 1950 with the introduction of the point contact germanium transistor. Few years later, silicon (Si) has become commonly used due to its excellent characteristics. Si devices have dominated for power management since the late 1950s. However, material properties of Si are becoming nowadays the limiting factor to produce more promising semiconductors [10]. Although the Si-based power converters today are already highly efficient, with efficiencies above 95% depending on the application, the relatively high loss and limited switching speed of the Si devices in electronic converters limit further improvement on power density. The reason is primarily the need for a heat sink and filters to dissipate losses, mainly semiconductor loss, and smoothen the high ripples of low switching frequencies respectively. This increases the system size and weight; hence reduce power density. Due to Si limitations in terms of its voltage blocking capability, switching frequency and high losses, a new generation of power devices is required for power converters in applications where Si power systems cannot operate. Here, the new WBG power devices can step in for more energy efficient systems. Among the possible candidates to be the base materials for these new power devices, GaN and SiC present the better trade-off between theoretical characteristics (high voltage blocking capability, high temperature operation and high switching frequencies), and real commercial availability of the starting material (wafers) and maturity of their technological processes [11].

In recent years, GaN and SiC based semiconductors called the "Next Generation Power Semiconductors" have been receiving much attention. Between the late 1980s and early 1990s, SiC was recorded as a superior power switches material [12]. GaN High Electron Mobility Transistor (HEMT) first appeared in about 2004 with depletion-mode transistors made by Eudyna Corporation in Japan [13]. In 2005, Nitronex Corporation introduced the first depletion mode HEMT transistor made with GaN grown on silicon wafers. In June 2009, Efficient Power Conversion Corporation (EPC) introduced the first enhancement-mode GaN on silicon power transistors designed to substitute power MOSFETs [13]. The switching frequency of GaN has been continuously pushed up to several MHz, depending on application ratings, to both reduce passive components size

and increase power density [10]. Table 1-1 summarizes the main material properties of the WBG semiconductors candidates to replace Si. Also, Fig. 1-1 presents a map comparing the properties of GaN and SiC materials to Si. These equal higher breakdown voltage, lower on-resistance, and lower drain leakage current than Si. Compared to Si, GaN and SiC have a wider band gap, therefore they are called "Wide Band Gap Semiconductors". Also, the Baliga's figure of merit (BFOM) ($\varepsilon\mu eEc^3$) is 440 and 1130 times higher than Si for SiC, and GaN respectively.

Table 1-1. Main material parameters of GaN and SiC compared to Si [14, 15].

Characteristic	Unit	GaN	Si	SiC
Bandgap	eV	3.49	1.1	3.26
Electron mobility	cm^2/Vs	2000	1500	700
Peak electron velocity	$x10^7 cm/s$	2.1	1.0	2.0
Critical (breakdown) electric field	MV/cm	3.0	0.3	3.0
Thermal conductivity	W/cm^oK	>1.5	1.5	4.5
Relative dielectric constant		9.0	11.8	10.0

Fig. 1-1. Si, SiC, and GaN relevant material properties [14].

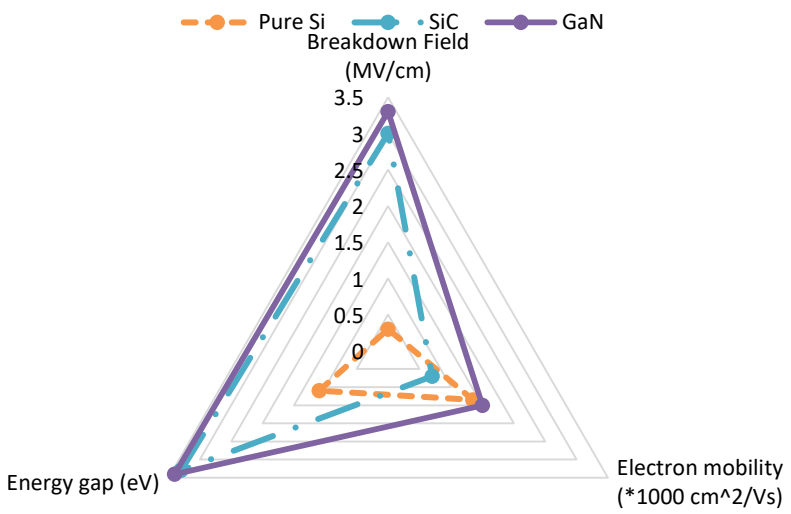

The emerging market for WBG power semiconductors is predicted by market researcher HIS to grow by a factor of 17, during the next 10 years, energized by growing demand for power supplies, hybrid and electric vehicles, and photovoltaic inverters [16]. GaN and SiC are to claim 22% of the $15 billion global market for discrete power electronic components by 2020 [9]. The following paragraphs introduce the three promising WBG semiconductor options for the DC/DC converter of EV powertrain, ordered by their potential superiority according to this thesis results and recommendation.

1.3 GaN on Si E-HEMT Cascode

In this research, a GaN on Si substrate E-HEMT cascode in one package shown in Fig. 1-2 is under investigation. It consists of a normally off low voltage (LV) Si MOSFET at the input and a normally on high-voltage (HV) GaN HEMT at the output in a cascode configuration [10, 17, 18, 19]. The lack of bulk GaN source material led to the need for GaN growth on mismatched substrates such as Si, SiC and sapphire. The first generation of 600 V GaN HEMT is intrinsically normally on (depletion mode HEMT) device. To

easily apply normally off (enhancement mode) GaN HEMT, a low-voltage Si MOSFET is in series to drive the GaN HEMT, which is well known as cascode structure [18]. When the gate of the Si FET is turned on, both devices are on with a total on-resistance (R_{dson}) as the sum of the two. When the Si FET is off, the Si FET sustains the whole bias voltage until it reaches the pinch off voltage of the GaN HEMT. At that point, the HEMT is turned off and will block all remaining voltage. As a result, the combined device is normally off having a gate threshold of the Si MOSFET and a blocking voltage equal to the GaN HEMT gate-drain breakdown voltage. Normally off devices are essential in terms of reliability for fail-safe reasons [20] [21]. The selection of the LV Si FET is based on: 1) its on-state resistance to be a small fraction of the GaN HEMT resistance; and 2) its breakdown voltage to be greater than the GaN HEMT pinch-off voltage, which is about 18 V. Any high-speed Si MOSFET with breakdown voltage >25 V and appropriate on-resistance is suited for this configuration. The safe operation area (SOA) of the cascode is the same as MOSFETs [17, 22]. GaN on Si E-HEMT cascode has a body diode that has a very low reverse recovery charge compared to Si MOSFETs as shown in Fig. 1-3 [23].

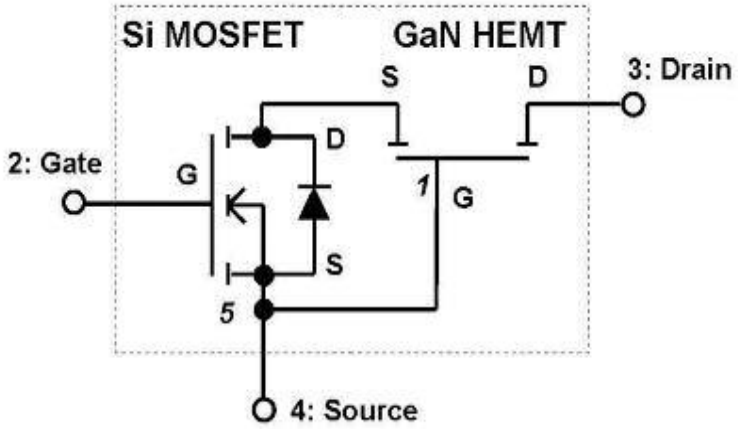

Fig. 1-2. GaN on Si substrate E-HEMT cascode in one package [17]

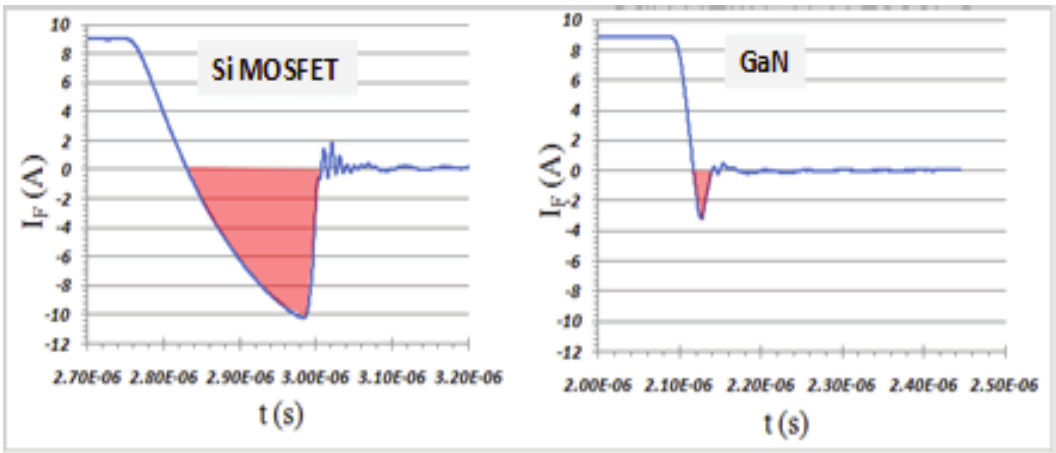

Fig. 1-3. Transphorm's GaN on Si cascade's body diode reverse recovery compared to Si MOSFET [23]

Article [24] discusses the status of the technology of this structure in terms of device performance, cost, and product reliability on two commercially available devices. Also, it announced that this cascode demonstrated both transistor performance enhancement and lower cost production than its silicon peers on the scale of low voltage transistors [24]. In the work of [19], several 600 V class GaN on Si HEMT prototypes were presented. Thanks to its large advantages in performances and cost, this paper expected that GaN on Si will most likely be the common technology over the next decade. Also in this work, 600 V class GaN on Si HEMTs have been characterized. Research in [25] investigated the dynamic capabilities of the 650 V GaN cascode power devices. Paper [26] presented the development of a simulation model for GaN transistors. In [27], Engineers of EPC developed the 500 W and 40-60 V / 12 V GaN-based 1/8th Brick DC/DC Converter, instead of a Quarter Brick, as shown in Fig. 1-4. Fig. 1-5 presents the 99% efficiency true bridgeless 3.5 kW Totem-Pole PFC based on GaN HEMTs developed by Transphorm. Another competitor in the market is Texas Instruments with its recent 600 V 10 A GaN device shown in Fig 1.7.

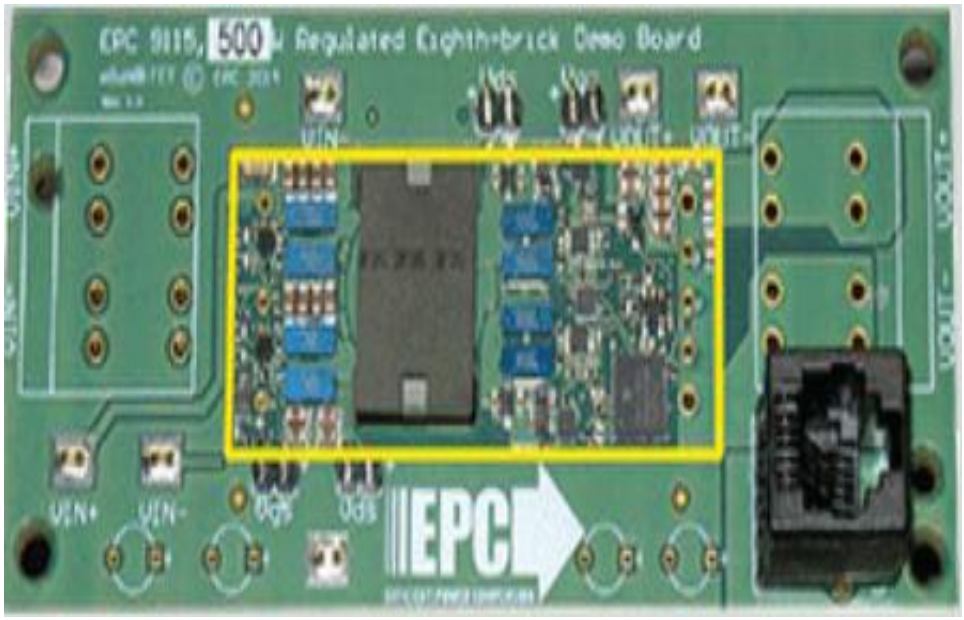

Fig. 1-4. The EPC9115, a demonstration board for the E-HEMT GaN based 500 W isolated eighth-brick DC/DC converter with fully regulated 12 V output at 42 A from an input range of 40 to 60 V [28]

Fig. 1-5. 99% efficiency true bridgeless 3.5 kW Totem-Pole PFC based on GaN HEMTs developed by Transphorm [23]

Fig. 1-6. LMG34XX GaN Power Stage Breakout Evaluation Module Board from Texas Instruments [29]

Fig. 1-7. LMG3410 GaN Evaluation Module Board from Texas Instruments [29]

According to GaN material properties and devices already available in the market, benefits of high voltage, low loss, and high speed GaN on Si switches are:

1. Increased bandgap giving higher blocking voltage with thinner material.
2. Higher critical breakdown field capability resulting in a thinner more highly doped drift layer; hence, lower on-resistance.
3. Higher electron mobility than Si and SiC resulting in higher switching speed.
4. Increased efficiency as a result of properties in points 1 and 2.
5. Smaller inductors/capacitors, heatsinks and PCB for overall system size, weight and cost reduction even against SiC as a result of 3 and 4.

Thanks to these better properties, the GaN on Si E-HEMT cascode has emerged as a promising device for high frequency, high efficiency, and high density power conversion in recent years.

1.4 SiC Trench MOSFET

The SiC transistor used in this research belongs to the family of SiC Trench ACCUFET devices [30] [31] at voltages from 400 V to 1700 V. Trench Structure refers to a type of structure wherein a MOSFET gate is formed on the sidewall of a groove created on the chip surface. As a result, switching performance is improved as shown in Fig. 1-8 (approx. 35% lower input capacitance) and on-resistance reduced by 50% over planar type SiC MOSFETs [30]. These devices are optimized for high-frequency power-electronics applications, including EV. Available devices in the market offer lower switching losses over peer Si devices as well as stability over the complete operating temperature range and long short circuit withstand rating. Table 1-2 below summarizes the main advantages of SiC over Si power devices [32].

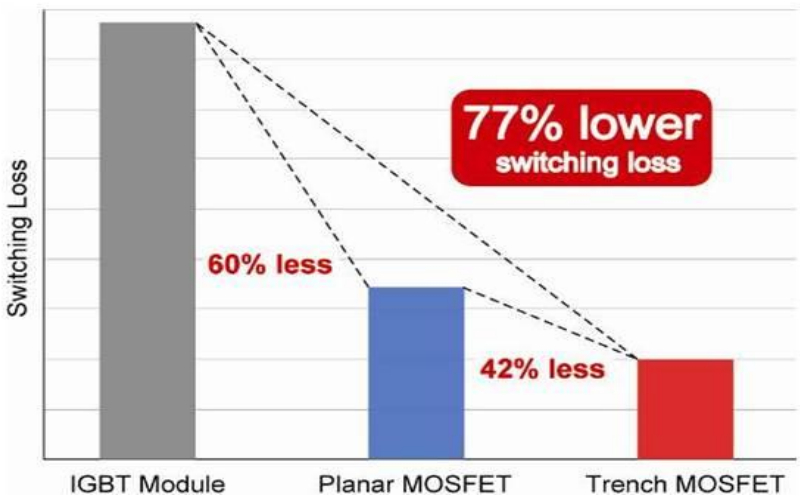

Fig. 1-8. Trench type SiC MOSFETs switching loss reduced by approximately 42% vs. planar type. [For the 1200 V/180 A class] [30]

Table 1-2. Main advantages of SiC vs Si power devices [32]

Characteristics	SiC vs. Si	Results	Benefits
Breakdown Field	10x Higher	Lower On-Resistance	Higher efficiency
Band Gap	3x Higher	Higher operating temperature	Improved cooling
Thermal conductivity	3x Higher	Higher power density	Higher current capabilities

1.5 Hybrid Module with SiC Schottky Barrier Diode (SBD)

High switching speed enables the use of smaller inductors and transformers, which can significantly reduce the size and cost of power systems. The size reduction is important because it increases the EV mileage. This requirement sets a very strong preference for unipolar devices to avoid long switching delays due to the need to recombine accumulated minority carriers. In the case of diodes, this means a very strong preference for the unipolar Schottky diodes over the bipolar p – n junction diodes. Moreover, SiC SBDs are known

for their very low reverse recovery loss. Fig. 1-9 shows that with a SiC SBD, switching losses are reduced by 2/3 compared to a silicon fast recovery diode (FRD) [33]. Additionally, SiC Schottky diodes can operate at much higher temperatures than Si [12]. These factors give a preference to SiC SBDs. A hybrid module that utilizes SiC SBD anti parallel to the traditional Si IGBT used in EV powertrain DC/DC converters can reduce the converter loss and size substantially than Si IGBT /bipolar p – n junction diode module.

Fig. 1-10 presents a Phase Shift DC/DC Converter setup utilizing SiC Trench MOSFET and SiC SBD developed by ROHM [34].

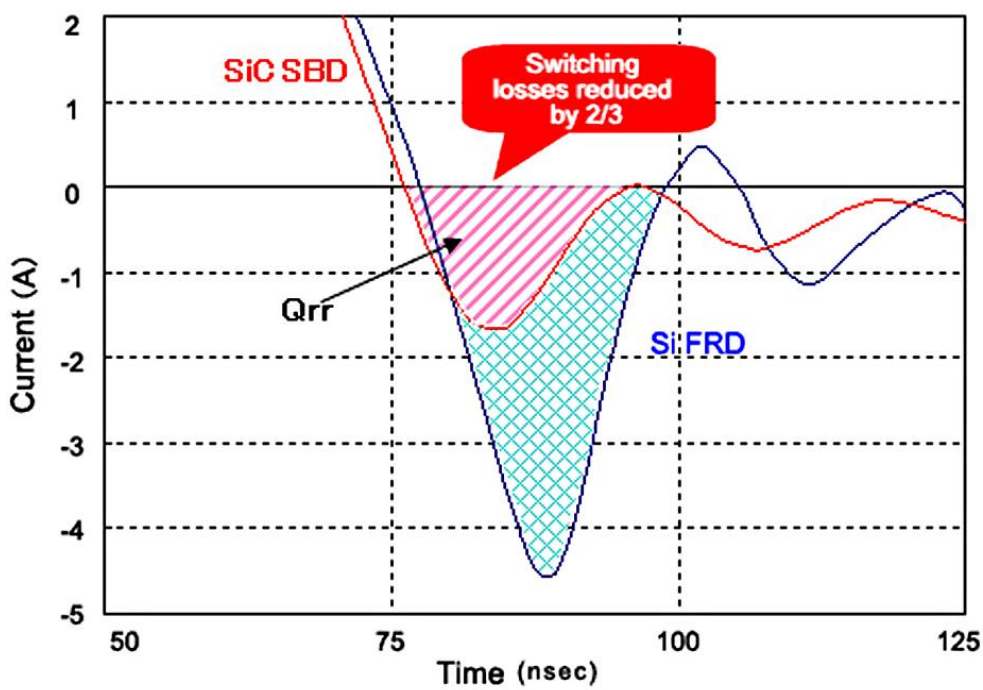

Fig. 1-9. With a SiC Schottky barrier diode (SBD), switching losses are reduced by 2/3 compared to a silicon fast recovery diode (FRD). The Si FRD is used for comparison since it has a comparable voltage rating to the SiC SBD. Qrr is the reverse recovery charge [33]

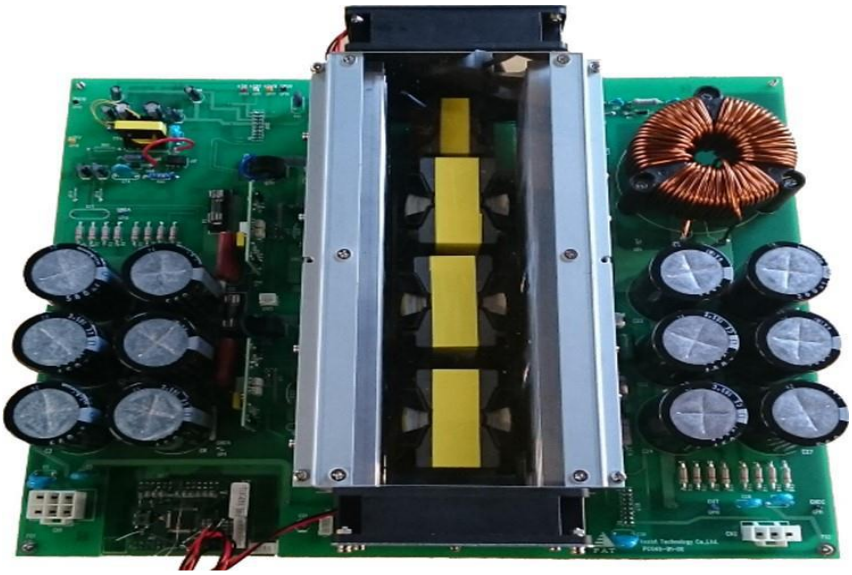

Fig. 1-10. Phase Shift DC/DC Converter Setup utilizing SiC Trench MOSFET and SiC SBD developed by ROHM [34]

Chapter 2 : Literature Review

Few papers studied the application of GaN in EV, and only for battery chargers not the powertrain. On the other hand, a lot of research is done on SiC in EV powertrain and battery chargers. Therefore, the focus of this research is the utilization and comparison of WBG devices options in the medium to high both power and voltage application of EV powertrain, with the GaN for the first time. Many studies, in the literature, focused on efficiency, size and power density improvements of converters utilizing excellent features of WBG devices. The following paragraphs categorize and summarize these papers' findings.

2.1 GaN in EV Battery Chargers

Paper [35] built a level-2 onboard charger (OBC) with the 650 V GaN E-HEMTs. The input voltage was 80–260 V AC, the battery voltage was 200–500 V and the rated power was 7.2 kW with the bidirectional power-flow capability. The overall system efficiency achieved was over 97% and the power density reported to be 2.5 kW/L; with the active filter and 3.3 kW/L without the active filter. In paper [36], the authors studied the design of high power density transformer and inductor for a high frequency dual active bridge (DAB) GaN charger. Thanks to the GaN properties, this charger has operated at 500 kHz. Accordingly, the inductance needed to achieve zero voltage switching (ZVS) for the DAB converter was reduced to as low as 3 μH. Consequently, it was possible to utilize the leakage inductor as the series inductor of the DAB converter. The designed transformer had 99.2% efficiency while delivering 3.3 kW. As a result, the power density of the designed transformer was 6.3 times of the lumped transformer and inductor in 50 kHz Si Charger. The detailed design procedure and loss analysis were discussed. The state of the art transformer design scored 2.2 kW/in^3 power density. The same converter structure at 500 kHz , a high frequency bi-directional battery charger for Plug-in Hybrid Electric Vehicle (PHEV) was optimally designed in [37] with high voltage normally-off GaN-on-Si. This design considered the wide battery voltage range and sinusoidal charging, to eliminate large DC link capacitor. Experimental results showed a 500 kHz DAB converter with discrete inductor and transformer could reach 97.2% efficiency at 1 kW and 96.4%

efficiency at 2.4 kW. By integrating the inductor into the transformer, 98.2% efficiency were scored at 1 kW.

2.2 SiC in EV Powertrain

Speaking of SiC, research in [6] presented a comparison of Si and SiC device technologies for the use in HEV traction inverters with a conclusion that the SiC devices, both JFETs and MOSFETs, can lead to a reduction in chip area and semiconductor losses by more than 50%. A bidirectional DC/DC converter that is suitable for HEV or EV applications were studied in [38] based on three sets of device combinations; all Si [Si (IGBT) and PN diode], hybrid (Si IGBT with SiC SBD), and all SiC (SiC MOSFET with SiC SBD). It was found that the 150 kHz all SiC converter is about 4.72 L smaller and 4.60 kg lighter than the 20 kHz all Si converter, while still maintaining a 0.14% higher efficiency. Paper [39] proposed an isolated quasi switched capacitor (QSC) DC/DC converter to serve as an auxiliary power supply in EV and HEV, managing a bidirectional power flow between the battery and the DC bus. SiC MOSFETs were selected for the proposed converter to increase the efficiency, cut the size of magnetics, and decrease the heat sink size. The authors in [40] tested a 1200 V, 880 A all-SiC dual module for 1,000 hours, in a HEV of 10-ton. This study documented stability of device characteristics and the performance capabilities of these SiC modules along with high reliability of paralleled devices. Paper [41] presented a comparative analysis between 1.2-kV SiC MOSFET/SBD and Si IGBT/PND technologies for EV powertrain performance. The devices' performance were evaluated between −75 °C and 175 °C at different switching speeds modulated by a range of gate resistances. According to the results, the SiC unipolar technologies outperformed Si bipolar technologies showing an average of 80% reduction in switching losses, 70% reduction in operating temperature and improved conversion efficiency.

2.3 SiC in EV Battery Chargers

A bidirectional integrated OBC and accessory power converter using SiC MOSFETs and SBDs is presented in [42]. Paper [43] proposed an isolated vehicular OBC that utilizes SiC power devices to achieve high density of 5.0 kW/L and high 2 stage efficiency of 95% for application in EVs with a switching frequency of 200 kHz.

2.4 Issues with WBG devices

Some papers addressed the issues and claims against SiC and GaN. The breakthrough performance of switching using GaN has been demonstrated. These issues include high temperature operation, unclamped inductive-switching (UIS) capability, reliability, packaging and simulation.

The authors of [44] investigated the variation of GaN devices turn on loss with junction temperature due to decreased transconductance. A detailed and simplified models relating temperature and turn-on loss was successfully developed for GaN HEMT, and verified with experimental results. This should help prevent thermal runaway for a more robust GaN power electronics systems designs. In [1] the current situation and future prospects for onboard SiC power devices and the development of practical automotive technologies are described. Also, this paper covers issues and topics such as SiC crystal growth, process technologies, defect analysis, and test results of actual onboard SiC applications. Research in [10] presented an accurate analytical model to calculate the power loss of a high voltage GaN HEMT in cascode configuration. The proposed model considered the package and PCB parasitic inductances, the nonlinearity of the junction capacitors along with the transconductance of the cascode GaN transistor. The switching process is illustrated in detail, including the interaction of the low voltage Si MOSFET and the high voltage GaN HEMT in cascode configuration. The results verified that the turn on loss is dominant in total switching loss at hard-switching conditions. However, turn on loss is minimized at soft-switching operation, and there is consequently some conduction loss. The authors concluded that this characteristic makes the cascode GaN transistor very suitable for high frequency operation as long as ZVS turn on is achieved. Paper [25] demonstrated that GaN power devices can have UIS capability comparable with their Si counterparts without the negative dynamic on specific resistance. Moreover, this work addressed important issues associated with 650 V GaN power devices, UIS capability and stable high-temperature dynamic R_{dson}, with over 1,000 hours at 520 V and 150 °C. Robust performance is demonstrated along with reliability of cascode GaN power devices in PFC tests. This is done at high power, at high frequency, and in a totem-pole circuit. In [45], technological advances on GaN HEMTs have been described and recent results for improving DC and

pulsed performance of GaN HEMTs have been reported. Focuses were placed on the progress toward enhancing the breakdown voltage, lowering R_{dson}, suppressing current collapse, and reducing the leakage current by introducing free-standing GaN substrates. Paper [46] presents a more general understanding of commercially available E-HEMT GaN primary failure modes under voltage and temperature stress. The authors also enumerated the reliability advantages of wafer level chip scale (WLCS) packaging compared to conventional MOSFET packages. Also, this study have further shown that GaN FETs are able to operate with very low probability of failures within the reasonable lifetime of end products manufactured today. In [47], a field programmable gate array (FPGA)-based real time (RT) platform for simulation of power converters with WBG devices is presented. The aim was to introduce these new devices to the current market, as RT simulation plays a fundamental role in the design and testing of these converter/machine drives.

2.5 WBG Semiconductors in General DC/DC Converters application

2.5.1 GaN

In [48], a simple SEPIC converter using a normally-off GaN-on-Si cascode switch was introduced. Operating with a switching frequency around 1.5 MHz, and with 100 W load, the compact circuit was measured to have a conversion efficiency of 94.25%. A high frequency high efficiency GaN device based interleaved critical conduction mode (CRM) bi-directional buck/boost converter with a coupled inductor was presented in [49]. Experimental results of this work validated the theoretical analysis, and the coupled inductor prototype efficiency was 98.5% at 1 MHz. A dead time optimization technique was tested for a soft-switched isolated GaN active-clamp flyback 15 V/ 6 V 2 W power supply in [50] and verified experimentally. In [22] True kV-class GaN HEMTs on Si were developed. Hard-switched operation was tested with outstandingly high efficiency of 99% in 400 V to 800 V boost converter hard-switched at 100 kHz.

Paper [51] reported that while GaN transistors show great advantages in hard switched converters, they still have advantages in soft switched converters, such as the LLC, with reduction of loss in the whole circuit of 15–30% across the load. The research in [51] focused on LLC converters with a 350–400 V input range and an isolated 12 or 48 V DC

output. The characteristics and operation principles of a 600 V cascode GaN HEMT were studied in [18] . Evaluations of its performance based on buck converter at hard-switching and soft-switching conditions were presented in detail. The cascode GaN HEMT was applied to a 1 MHz 300 W, 400 V to 12 V LLC converter. A comparison of experimental results with a state of the art Si MOSFET is provided to validate the advantages of the GaN HEMT. Experimental results proved that the cascode GaN HEMT is superior to the Si MOSFET, but it still needs soft switching in high frequency operation due to considerable package and layout parasitic inductors and capacitors. A high-power density quasi-resonant converter is proposed in [52] using GaN HEMT devices. In [53], A 2.5 kW T-type inverter design was studied under three 600 V switch choices; Si IGBT, SiC MOSFET and GaN HEMT. The comparison included gate driver and switching losses, inverter footprint in terms of both heat sink and output filter, and dead time effect.

2.5.2 SiC

The research of [54] quantified the merits of utilizing SiC power MOSFETs and diodes in a 10 kW interleaved hard-switched boost converter. Simulation and experimental study in [55] demonstrates that SiC semiconductors are more efficient in power conversion than Si MOSFETs. This comparison held considered a 1.2 kW DC–DC converter switched over a frequency and temperatures ranges up to 300 kHz and from 25 to 150 °C respectively. Paper [56] presented a comparison of Si and SiC device technologies for the use in HEV traction inverters. SiC JFETs and SiC MOSFETs are characterized and a scalable thermal modeling approach was used to find the optimum chip area for each Si or SiC traction inverter. It was concluded that SiC can lead to a reduction in chip area and semiconductor losses by more than 50%.

2.6 Regenerative braking of EVs

Regenerative braking in any adjustable speed drive system is generally used when a short deceleration time is needed, a high inertia is present and a recovery of energy can be economically justified according to NEMA Standards Publication ICS 7.2-2015 [57]. During regenerative braking, the kinetic energy of the car wheels is converted by the electric machine, working in the generator mode then so achieve braking, into electrical energy recovered and restored back into the battery for later usage. In this way some of the energy which is normally lost as frictional heat during braking is utilized [58]. This section lists the up to date published work in the area of regenerative braking in EV drives.

An EV IPMSM drive were developed in [59] along with its control. The driving performance was enhanced using techniques of DC link voltage boosting and commutation tuning. This drive utilized a two-leg interleaved bidirectional front-end DC/DC buck–boost converter and a three phase inverter. Results indicated good performance in terms of starting, acceleration/deceleration, regenerative braking, and reversible operation.

Paper [60] compares between three control systems for energy recovery during EV braking based on simulation results. This research concludes that the optimized fuzzy control strategy can capture more braking energy and is much safer. The authors of [61] successfully applied an algorithm to optimally search the train braking speed trajectory for maximum regenerative braking energy under different constraints with a high level of robustness.

A modular multilevel DC/DC converter for regenerative applications with supercapacitors (SCs) was proposed in [62]. The authors were successful, through simulations and hardware, in lowering output inductor size and weight while balancing SCs voltage. Paper [63] proposes an algorithm to recover braking energy of a multi tram system and store it in capacitive banks which are global among trams, with two stages one of them contains super capacitors.

A regenerative burn-in test system for high-power DC/DC converters is developed in [64] to reduce power supply and load testing requirements. A regenerative braking system (RBS) mathematical model were described and simulated using Matlab in [65]. This RBS components are a three-phase PMSM, a diode based three-phase full-wave rectifier and a

DC/DC bidirectional converter. The developed model is effective in accessing the effectiveness of utilizing RBS in an EV.

Chapter 3 : System Modeling and Simulation

3.1 Problem Statement and Solution Methodology

This research aims to choose the best semiconductor candidate for the switches in the EV powertrain's DC/DC converter. The objective is to minimize the total switch losses and consequently, increase the efficiency, reduce the converter size and weight; hence, enhance power density and boost car mileage.

To solve this problem, a model was built in PSIM to model the EV powertrain, both power and control circuits as will be shown in the next section. This model considered, for the first time, the recent next generation WBG power semiconductor devices available in the market, both the GaN on Si E-HEMT Cascode and SiC Trench MOSFET (ACCUFET). This model also considers the Hybrid switch; Si IGBT with antiparallel SBD, which appeared as a competitor to the existing Si IGBT with p-n diode option last few years. The pure Si MOSFET switch has been considered too. The model is able to calculate the values of each power and control circuit variable, including each switch type losses, both conduction and switching. The lower these losses, the more the switching frequency can be pushed up for reduced filtering components footprint.

First, each powertrain component was rated according to the under study EV specifications and market components. Secondly, the DC/DC converter design calculations were carried out accordingly. After that, the model was tested successfully with ideal switches and the control parameters were determined by trial and error to get the required transient response. As soon as the stable response was reached ideally, the switch type has been considered. Finally, the DC/DC converter efficiency is calculated for each switch option and the most efficient candidate option is promoted accordingly. The best candidate switch for the DC/DC converter is selected based on the higher efficiency which conforms to the smaller footprint, hence, higher power density and mileage.

3.1.1 Assumptions

This study was carried out based on the following assumptions:

- The vehicle environment conditions are fixed; so that the driving or braking torque commands don't vary with time.
- A cooling environment is assumed to be successful in maintaining the tested junction temperatures.
- A gate turn on and off resistances of 5 ohms is used in simulation. Lower values may be insufficient in turning on the switching devices and higher values may cause excessive ripples.

3.1.2 Case Studies

In addition to changing the switch type in the DC/DC converter, the following sensitivities are considered.

3.1.2.1 Vehicle Load

Two load types are considered in this research, a road passenger vehicle and a railway metro car. The model built simulates the Nissan Leaf EV parameters in the first category and the Bombardier's Advanced Rapid Transit (ART) in Vancouver in the second category. The relative specifications for each vehicle are illustrated under the following two chapters.

3.1.2.2 Motor/ Generator mode

Both traction (motoring) and forward regenerative braking are tested in a simple reference speed step change. The model was tested against a simple drive cycle of 3 steps as shown in Fig. 3-1 for road vehicle. These steps, by order, are:

1. Acceleration to normal speed from standstill,
2. Braking to 1% of the first step speed,
3. Acceleration to the speed of the first step again.

The railway system is tested against a wider driving cycle of the same shape; because of higher inertia.

3.1.2.3 Junction Temperature

The switching semiconductor options are tested at both 25 ºC and 150º C junction temperatures assuming that cooling methods are able to maintain these two levels. The choice of 25 ºC and 150º C is based on the fact they are the start and end of the derating range of the semiconductor devices under test respectively. The devices parameters are given usually at these temperatures in the manufacturer datasheets.

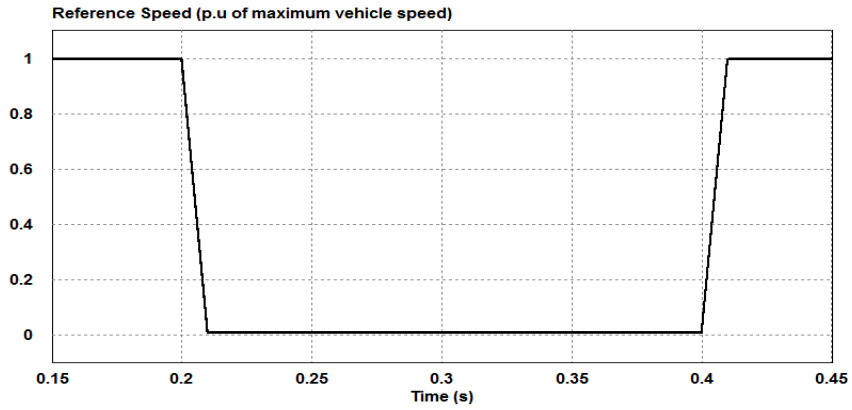

Fig. 3-1. The tested simple drive cycle for the road passenger vehicle case

3.2 EV Powertrain Architecture Modelling in PSIM

The EV powertrain produces the power of the car in place of an engine. The motor is the source of the mechanical power and the battery is the electrical supply to the motor. Powertrain architecture is still under improvement in research community, looking for increased efficiency architectures, by several researchers [66] [67] [68] [69]. Any EV powertrain system can be modeled as seen in Fig. 3-2. The following subsections describes each block in detail along with the associated parameters and input and output signals.

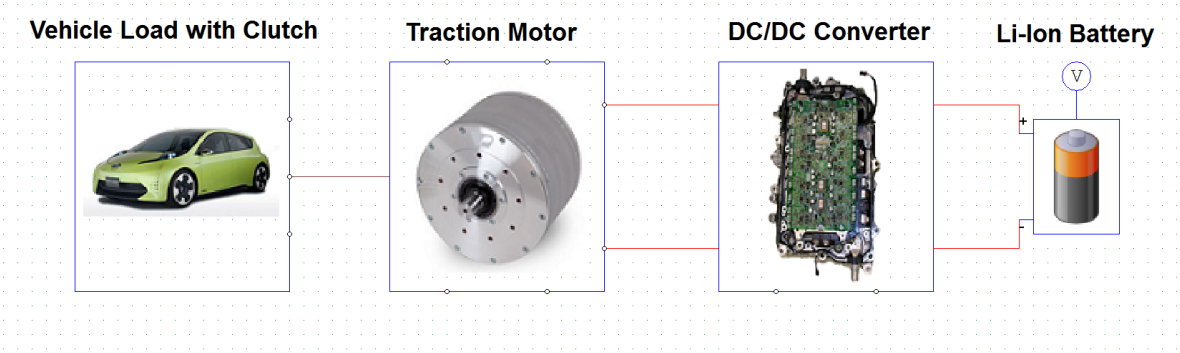

Fig. 3-2. EV powertrain Model Block diagram in PSIM

3.2.1 Vehicle Load with Clutch

The vehicle load with clutch, like any traction load, is modelled as a constant torque load. This constant value doesn't depend, for the same environment, on speed. If the delivered torque is away from this value, undesired behaviours appear in the tire movement. The value of this torque depends on many factors and differs for the same vehicle with many factors; e.g., vehicle loading, road and tire conditions, whether the vehicle is on drive or brake modes, and whether the vehicle is front, rear or all wheel driven. Depending on the wheel diameter of the vehicle and its transmission system, its required linear speed setting is translated into a rotary speed setting for the traction motor drive to follow. The powertrain design for the vehicle traction is totally dependent on the vehicle load value. Fig. 3-3 presents the vehicle load with clutch model in PSIM.

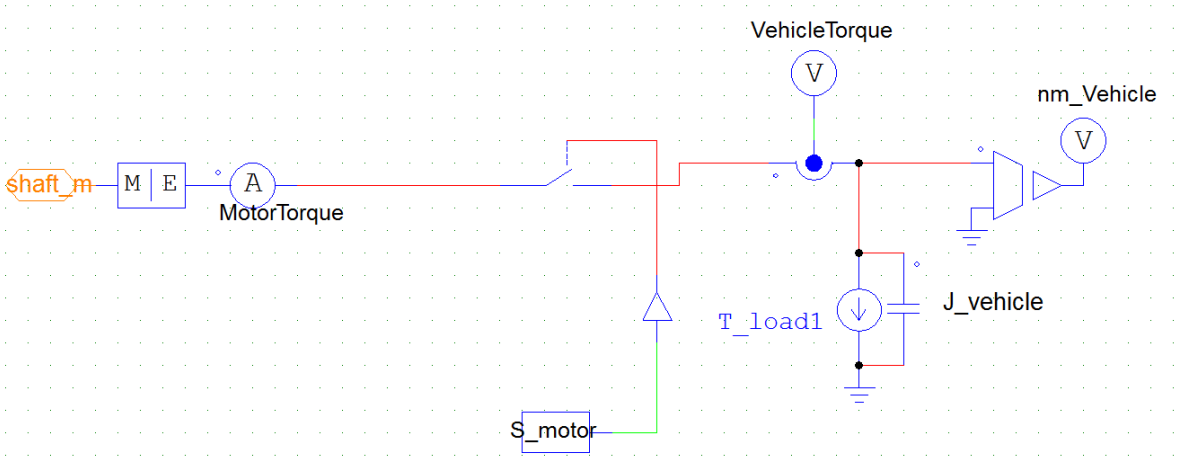

Fig. 3-3. Vehicle load with clutch model in PSIM

The required specifications of the vehicle load to be entered to the PSIM simulation environment are:

- T_load1: Vehicle load torque, in N.m
- J_vehicle: Vehicle moment of inertia, in kg*m^2

3.2.2 Traction Motor

An IPMSM block is used in PSIM to model the traction motor of the NLEV. The IPMSM is used in the EV powertrain in this study for its advantages as illustrated in Appendix I. The IPMSM allow a wide field weakening range due to its high saliency. This makes it the best choice for EV application. The schematic diagram of this traction motor drive is shown in Fig. 3-4.

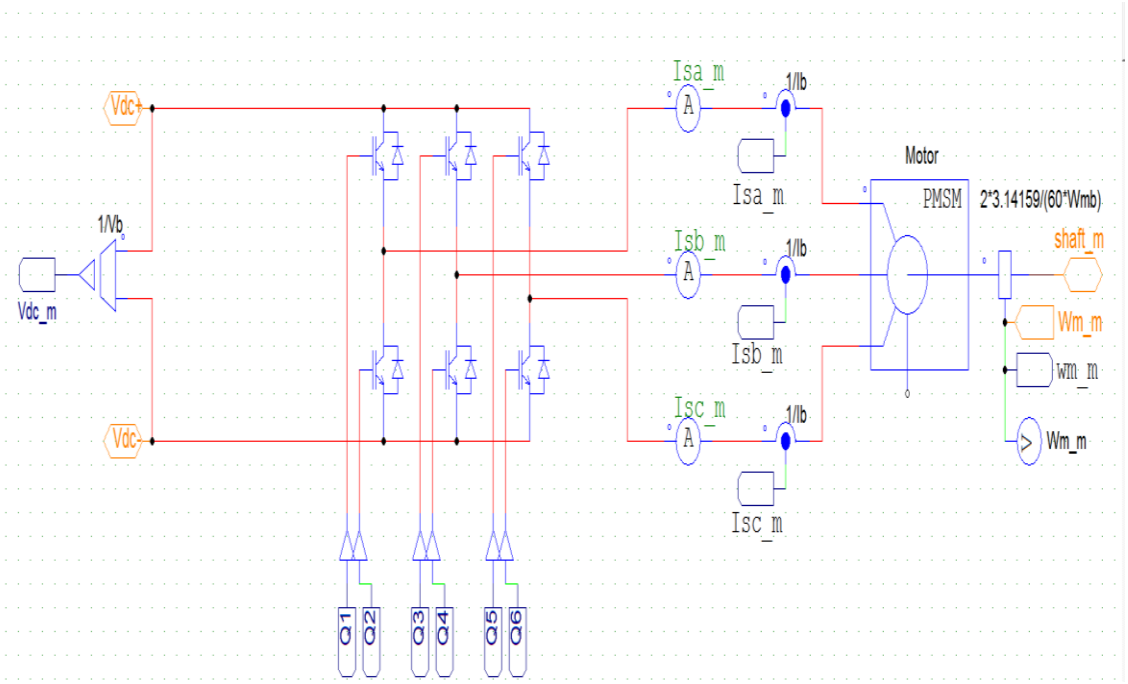

Fig. 3-4. Power circuit modelling of motor drive in PSIM

The required motor Parameters to be entered to the PSIM Model are as follow:

1. Number of Poles.
2. Peak line-to-line back EMF constant in Vpk/krpm.
3. Stator winding resistance in ohms.
4. d-axis inductance at rated conditions in H.
5. q-axis inductance at rated conditions in H.
6. Moment of inertia in kg.m^2.
7. Shaft time constant in sec.
8. Maximum motor torque in N.m.
9. Maximum motor power in kW.
10. Maximum motor speed in kW.

3.2.2.1 3-phase Inverter Control

A 3- phase inverter is used as a VSI to the traction motor as seen in Fig. 3-4. The traction motor operates in speed control mode as the motor torque is constrained by the constant load torque. A torque reference is established by the speed control block. After that, the

DTLC block determines the threshold speed. Below the threshold speed, the motor operates in Maximum Torque per Ampere Control (MTPA) control. Beyond the threshold speed, the motor operates in the constant power region in field weakening control, and the DTLC block will limit the torque reference accordingly. The torque reference, whether limited by DTLC or not, is then converted to a current reference by the torque constant (K_TA_m) calculated from the Line-to-line back EMF constant. This current reference is used by the MTPA block or the field weakening control block to generate the current references for direct and quadrature axis components; i.e. i_d and i_q. These current references are then fed to the inner current control loop. The inner current loops and the outer speed loops can operate at different sampling rates. The control flow through these blocks are shown in Fig. 3-5.

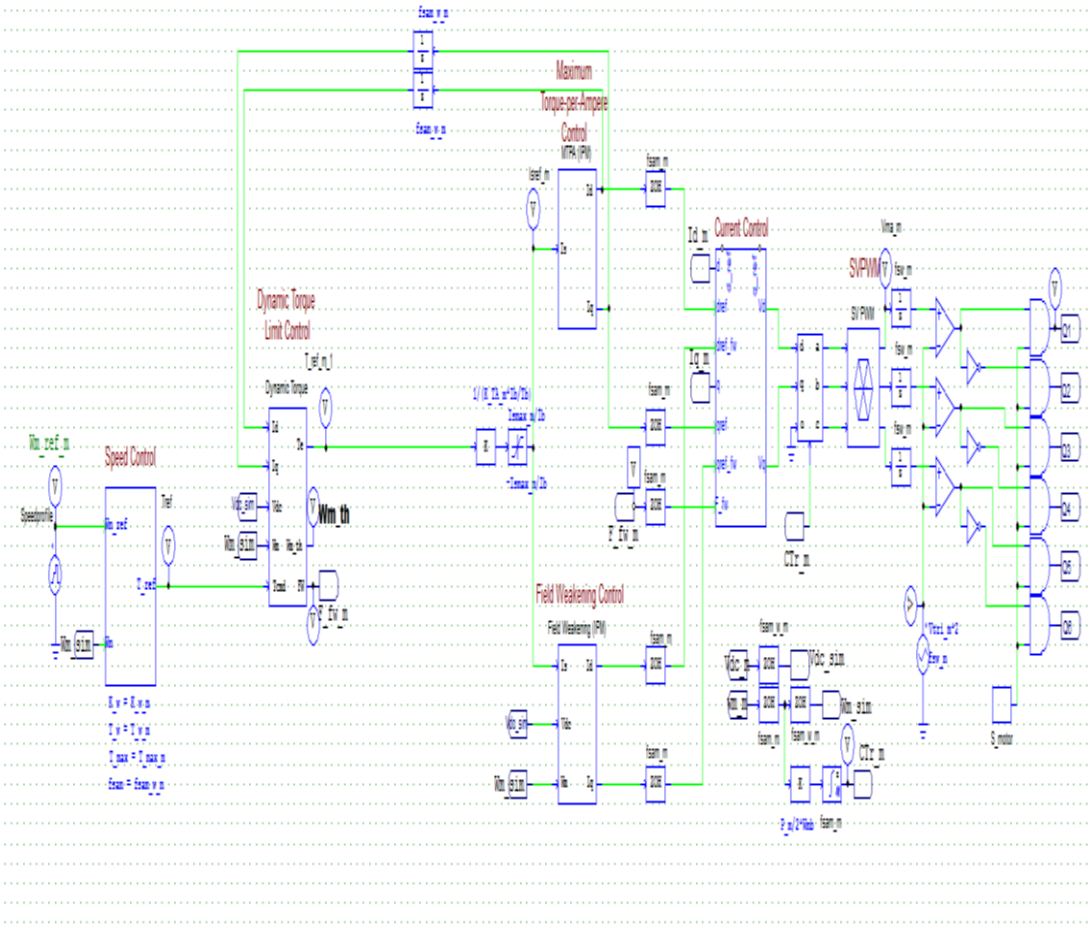

Fig. 3-5. The motor Control circuit in PSIM

The required specifications of the inverter control to be entered to the PSIM simulation environment are:

1. Inverter switching frequency in Hz.
2. PWM carrier peak amplitude.
3. Inner current loop sampling frequency in Hz.
4. Outer speed loop sampling frequency in Hz.
5. Maximum inverter output current amplitude in A.

Moreover, the following subsections present the functions of these milestone blocks along with their inputs and outputs.

3.2.2.1.1 Speed Control

This block uses a digital PI controller to regulate the motor speed. The PI output is limited to the maximum torque T_max that the motor can provide. The inputs and outputs of this block are listed in Table 3-1.

Table 3-1. The inputs and outputs of the Speed Control block

Input	Wm_ref	Motor mechanical speed reference
	Wm	Motor mechanical speed feedback
Output	T_ref	Torque command

3.2.2.1.2 Dynamic Torque Limit Control (DTLC)

This block calculates the threshold speed of the MTPA region; i.e. constant torque motor operation region as in Appendix I. When the motor speed is less than this speed limit, the motor operates under MTPA control. Otherwise, it operates in the constant power region with field weakening control. The inputs and outputs of this block are listed in Table 3-2.

Table 3-2. The inputs and outputs of the Dynamic Torque Limit control block

Input	Id, Iq	d-axis and q-axis currents feedback
	Vdc	Measured DC bus voltage
	Wm	Motor mechanical speed feedback
	T_cmd	Torque command
	T_ref	Torque command
Output	Te	Torque reference
	Wm_th	Calculated base speed of the MTPA region
	FW	Flag of field weakening (1: in field weakening region; 0: not in the field weakening region)

3.2.2.1.3 Maximum Torque per Ampere (MTPA) Control

This block uses the motor parameters and the current reference to calculate the d-axis and q-axis current reference values such that the maximum efficiency and torque output are achieved. The inputs and outputs of this block are listed in Table 3-3.

Table 3-3. The inputs and outputs of the MTPA control block

Input	Is	Inverter current amplitude reference
Output	Id_ref, Iq_ref	MTPA d-axis and q-axis current references

3.2.2.1.4 Field Weakening Control

In case the reference speed is higher that the base speed determined by the DTLC, this block uses the motor parameters and the current reference I_s to calculate the d-axis and q-axis reference values to achieve the constant power operation; i.e. field weakening (FW). The inputs and outputs of this block are listed in Table 3-4.

Table 3-4. The inputs and outputs of the Field Weakening control block

Input	Is	Inverter current amplitude reference
	Vdc	Measured dc bus voltage, in V
	Wm	Motor mechanical speed in rad/sec.
Output	Id_ref_fw, Iq_ref_fw	FW d-axis and q-axis current references

3.2.2.1.5 Current Control

The current control contains two loops, one for i_d and another for i_q, to generate the voltage references. Both loops are digital PI control based. When the field weakening flag (F_fw) is 0, the current references Idref and Iqref, output from the MTPA control, are used. When the flag is 1, the current references Idref_fw and Iqref_fw, from the field weakening block, are used. The inputs and outputs of this block are listed in Table 3-5.

Table 3-5. The inputs and outputs of the Current Control block

Input	Id, Iq	d-axis and q-axis currents feedback
	Id_ref, Iq_ref	d-axis and q-axis current references from the MTPA control block
	Id_ref_fw, Iq_ref_fw	d-axis and q-axis current references from the field weakening block
	F_fw	Field weakening flag from the Dynamic Torque Limit Control block
	Vd, Vq	d-axis and q-axis voltage references

3.2.2.1.6 Speed and MTPA PI Control

The PI controller constants of motor control with other dependent parameters depend on the load and are to be tuned using trial and error. These required parameters are listed in Table 3-6.

Table 3-6. Required parameters of motor control

	Definition	Symbol
Motor	Torque constant, in N.m/A	K_TA_m
	Maximum torque based on current limit Ismax_m	Te_max_m
Inverter	Max inverter ac voltage (phase peak)	Vsmax_m
d-axis current control loop	PI gain	K_d_m
	PI time constant	T_d_m
d-axis current control loop	PI gain	K_q_m
	PI time constant	T_q_m
Speed control loop	PI gain	K_w_m
	PI time constant	T_w_m

3.2.3 DC Bus

The DC bus is located between the 3 phase inverter of the traction motor drive and the DC/DC converter at the battery side, as seen in Fig. 3-6. Its voltage is regulated by the DC/DC converter and characterizes the motor drive. The required parameters of the DC bus to be entered to the PSIM model are:

1. Nominal DC Bus Voltage in V.
2. Minimum DC Bus Voltage in V.
3. Maximum DC Bus Voltage in V.
4. DC bus capacitance in F.

3.2.4 DC/DC Converter

EV DC-DC Converter is located between the high voltage battery and the motor drive. It is a bidirectional drive that has the capability to work in both the motoring (traction) and the regenerative braking modes. It enables the generation of a controlled output dc voltage from any input dc voltage. The schematic diagram of the bi-directional DC-DC converter block is shown in Fig. 3-6. Its function is to regulate the DC link voltage during acceleration, fixed speed and deceleration operations. Its control, as shown in Fig. 3-7, consists of a discharge controller, charge controller, and regeneration controller.

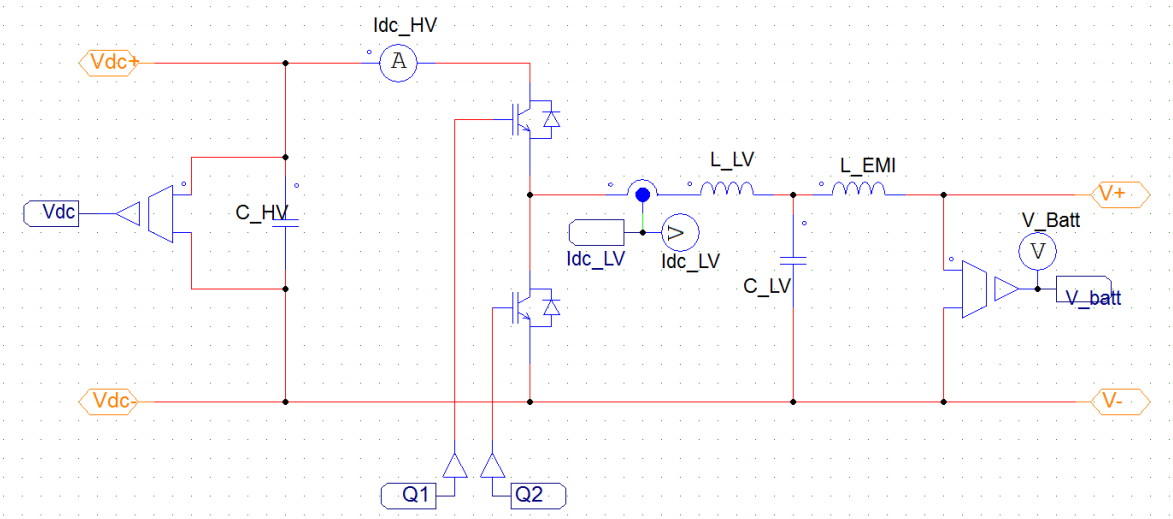

Fig. 3-6. Bidirectional DC/DC converter between DC link and battery

The required parameters of the DC bus to be entered to the PSIM model are:

1. Maximum battery charging power in kW.
2. Maximum battery discharging power in kW.
3. Converter switching frequency in Hz.
4. Low-Voltage Side Inductance in H.
5. Low-Voltage Side Capacitance in F.
6. Carrier peak amplitude.

3.2.4.1 Inductor Selection

The inductor value (L_LV) selection is dependent on the converter's switching frequency, Input battery voltage (V_{batt}) and output DC bus voltage (V_{dc}) ratings, the load power command, and the allowed current ripple. The minimum inductor value corresponds to a current ripple twice the average inductor current (I_{batt}). The maximum allowed inductor current ripple is 5%. The design for L_LV is based on the motoring mode. During motoring, this bidirectional DC/DC converter works as a boost converter where the ideal input output relation is:

$$V_{dc}/V_{batt} = 1/(1-D) \quad (1)$$

The inductance value for a certain allowed current ripple is governed by the following equation:

$$\Delta I_L = D\, V_{batt} / L\_LV\ f \quad (2)$$

$$= (1- V_{batt}/V_o)\, V_{batt} / L\_LV\ f \quad (3)$$

$$L\_LV\ f = (1- V_{batt}/V_o)\, V_{batt} / \Delta I_L \quad (4)$$

$$\text{or} \quad L\_LV\ f = (1- V_{batt}/V_o)\, V_{batt} / \Delta I_L\%*I_{batt} \quad (5)$$

$$\text{or} \quad L\_LV\ f = (1- V_{batt}/V_o)\, V_{batt}^2 / \Delta I_L\%*\text{load power} \quad (6)$$

The load power command, and the allowed current ripple are the constraints governing the selection of the inductor value L_LV in a DC/DC converter at a certain voltage ratings for a given switching frequency. The less the L_LV value the better, as long as it satisfy these constraints.

3.2.4.2 DC/DC Converter Control

The DC/DC Converter Control is responsible for the switching of the converter's transistors and adjusting the transistors' firing signals according to the required mode of operation; charging the battery or discharging it. It consists of, a charge controller, discharge controller, and regeneration controller. The following sections illustrate the

functions of these controllers. The modulation signal is taken, either from the charge or the discharge controllers depending on the regeneration controller output. These connections between the 3 controllers are presented in Fig. 3-7.

3.2.4.2.1 Charge Control

This block implements Constant Voltage Constant Current battery charging. When the battery voltage is less than the battery float voltage, it is constant current charging. This means that the outer voltage loop is disabled and the inner current loop charges the batteries at a constant current rate. When the battery voltage reaches the battery float voltage, it is constant voltage charging. This means that the outer voltage loop generates the current reference for the inner current loop. The inputs and outputs of this block are listed in Table 3-7.

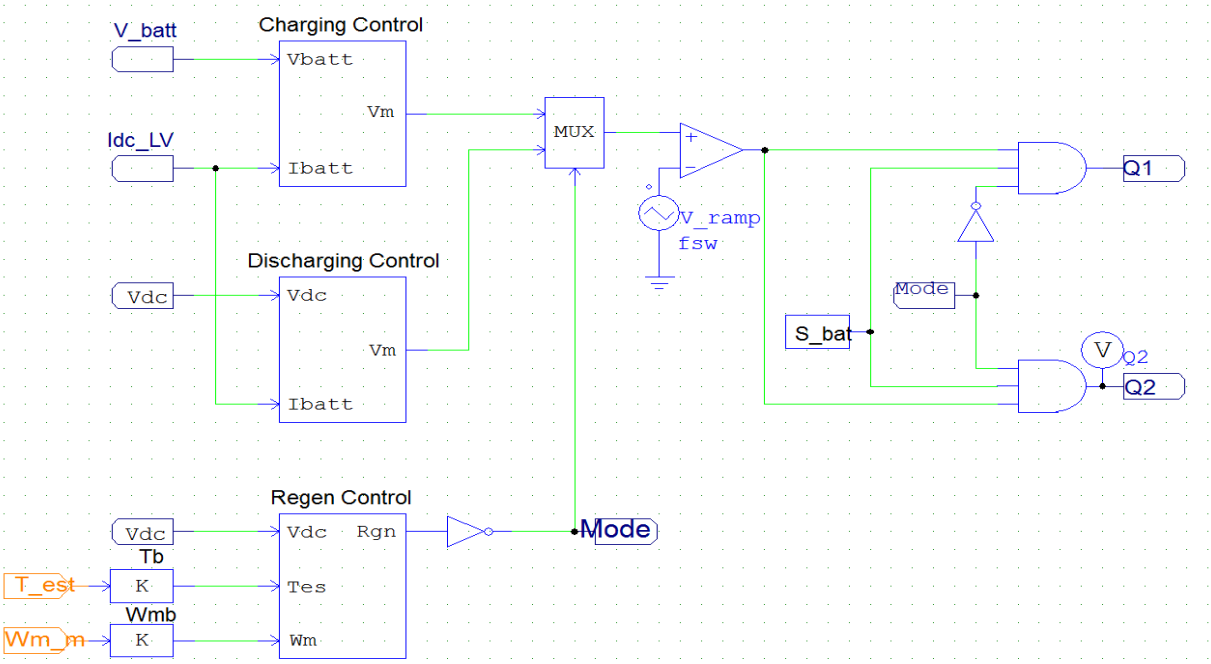

Fig. 3-7. DC/DC converter control circuits

Table 3-7. The inputs and outputs of the Charge Control block

Input	Vbatt	Battery side voltage feedback
	Ibatt	Current into the battery feedback
Output	Vm	Modulation signal for PWM generator

3.2.4.2.2 Discharge Control

This block implements constant-voltage battery discharging. The DC/DC converter regulates the DC bus voltage, and the outer voltage loop generates the reference for the inner current loop. The inputs and outputs of this block are listed in Table 3-8.

Table 3-8. The inputs and outputs of the Discharge Control block

Input	Vdc	DC bus voltage feedback
	Ibatt	Current into the battery feedback
Output	Vm	Modulation signal for PWM generator

3.2.4.2.3 Regeneration Control

This block generates the regeneration flag based on the motor power. When the motor power is negative and it exceeds the regeneration power threshold level, and if the dc bus voltage exceeds the maximum voltage, the regeneration flag will be set. The inputs and outputs of this block are listed in Table 3-9.

Table 3-9. The inputs and outputs of the Regeneration Control block

Input	Vdc	DC bus voltage feedback
	Wm	Vehicle speed feedback
	Tes	Estimated traction motor torque
Output	Rgn	Regeneration flag (1: regeneration; 0: no regeneration)

The required DC/DC converter parameters and associated symbols are as seen in Table 3-10.

Table 3-10. DC/DC converter parameters and associated symbols

Current loop	PI gain	K_ca_up
	PI time constant	T_ca_up
Voltage loop	PI gain	Kv_up
	PI time constant	Tv_up
Regen mode control	regen power limit	P_regen

3.2.4.3 Switch losses calculation

3.2.4.3.1 Transistor Losses

The transistor conduction losses is calculated as follow depending on whether it is a MOSFET or IGBT as the related parameters given for each in the datasheet are different.

Transistor Conduction Losses (MOSFET) = $I_D^2 * R_{DS\ on} * D$ *(11)*

Where

- I_D is the MOSFET drain current.
- $R_{DS\ on}$ is the static on-resistance.
- D is the switching duty cycle.

Transistor Conduction Losses (IGBT) = $IC * V_{CE(sat)} * D$ (12)

Where

- I_C is the IGBT collector current.
- $V_{CE\ (sat)}$ is the IGBT saturation voltage.
- D is the switching duty cycle.

The transistor switching losses whether it's a MOSFT or IGBT is calculated as follow:

Transistor Switching Losses = $E_{on} * f + E_{off} * f$ (13)

Where

- f is the switching frequency.
- E_{on} and E_{off} is the transistor turn-on and off energy losses respectively.

The energy losses E_{on} and E_{off} are calculated using the rise time (t_r) and the fall time (t_f) of the voltage and current waveforms as shown in Fig. 3-8. Transistor switching waveformThis is done based on the information of the MOSFET gate current, input/output/reverse transfer capacitances, and gate charges and using the equations provided in [10], [70], [71]. The gate charge losses are usually quite small compared to the turn-on/turn-off switching losses, and can be neglected at full load conditions. However,

they can become substantial in the light load conditions. Gate losses is neglected under the load considered in this study.

3.2.4.3.2 Diode Losses

In calculating the diode switching losses, the diode turn-on losses is neglected and are not considered. The diode turn-off losses due to the reverse recovery is calculated according to the waveform in Fig. 3-9 as follow.

$$\text{Diode Switching Losses} = 1/4 * Qrr * V_R * f \qquad (14)$$

Where

- Q_{rr} is the reverse recovery charge.
- V_R is the actual reverse blocking voltage.

The diode conduction losses is calculated as follow:

$$\text{Diode Conduction Losses} = V_d * I_F * (1-D) \qquad (15)$$

Where

- V_d is the diode voltage drop.
- I_F is the diode forward current.

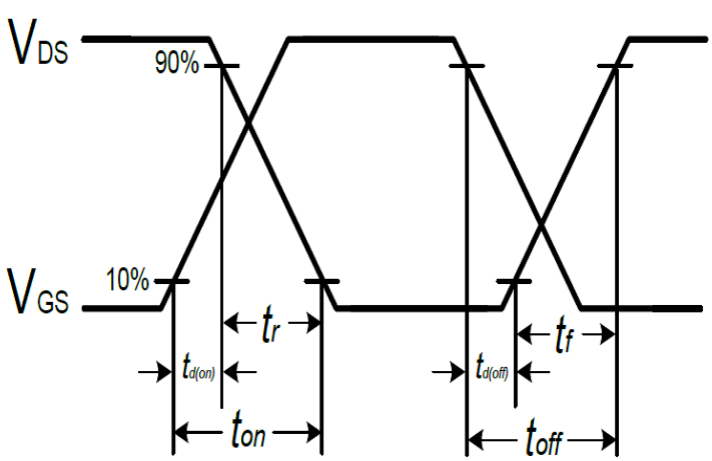

Fig. 3-8. Transistor switching waveform

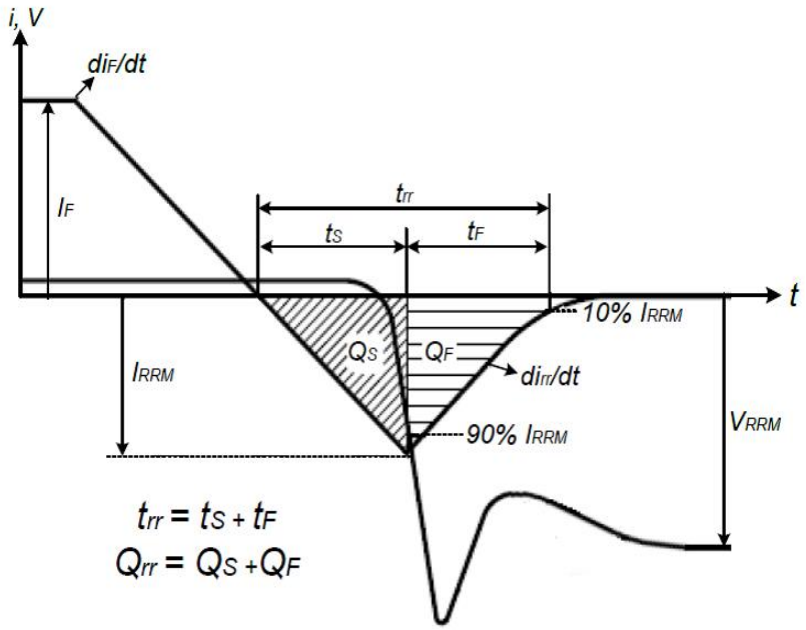

Fig. 3-9. Diode recovery waveform

3.2.4.4 Semiconductor Devices under comparison

This research, as mentioned in the abstract, has compared low losses fast switching WBG semiconductor options, SiC Trench MOSFET switches (ACCUFET) and GaN on Si E-HEMT cascode, for the high power high voltage application of DC/DC converter in the EV powertrain's DC/DC converter. Also, the pure Si MOSFET is considered in the selection for the NLEV load. Due to GaN and pure Si MOSFET voltage limits (< 650 V), only SiC ACCUFET and hybrid modules, Si IGBT with anti-parallel SiC SBD, are considered for the ART load. SiC ACCUFET devices are designed for high frequency high power ultra-low loss applications. The SiC ACCUFET belongs to the family of SiC Trench power devices that can withstand voltages from 400 V to 1700 V. Trench Structure refers to a type of structure wherein a MOSFET gate is formed on the sidewall of a groove created on the chip surface. As a result, switching performance is improved [30]. The pure Si MOSFET used in this study belongs to the 650 V CoolMOS™ CFDA series automotive qualified technology with integrated the Fastest Body Diode on the market [72].

3.2.5 Li-Ion Battery

The required specifications of the Li-ion battery pack used in PSIM are listed below:

1. Number of cells in series.
2. Number of cells in parallel.
3. Rated cell voltage in V.
4. Full cell voltage in V.
5. Discharge cut-off cell voltage in V.
6. Rated cell capacity in Ah.
7. Internal cell resistance in ohm.
8. Maximum cell capacity in Ah.
9. Exp. point cell voltage in V.
10. Exp. point cell capacity in Ah.
11. Maximum continuous current in A.

The first two parameters are calculated as follow:

Number of cells in series (Ns) = Battery terminal voltage/cell voltage *(16)*

Number of cells in parallel (Np) = Rated battery energy / terminal voltage/ cell capacity

(17)

The detailed model (power and control circuits) schematic for the whole EV powertrain is presented in Fig. 3-10.

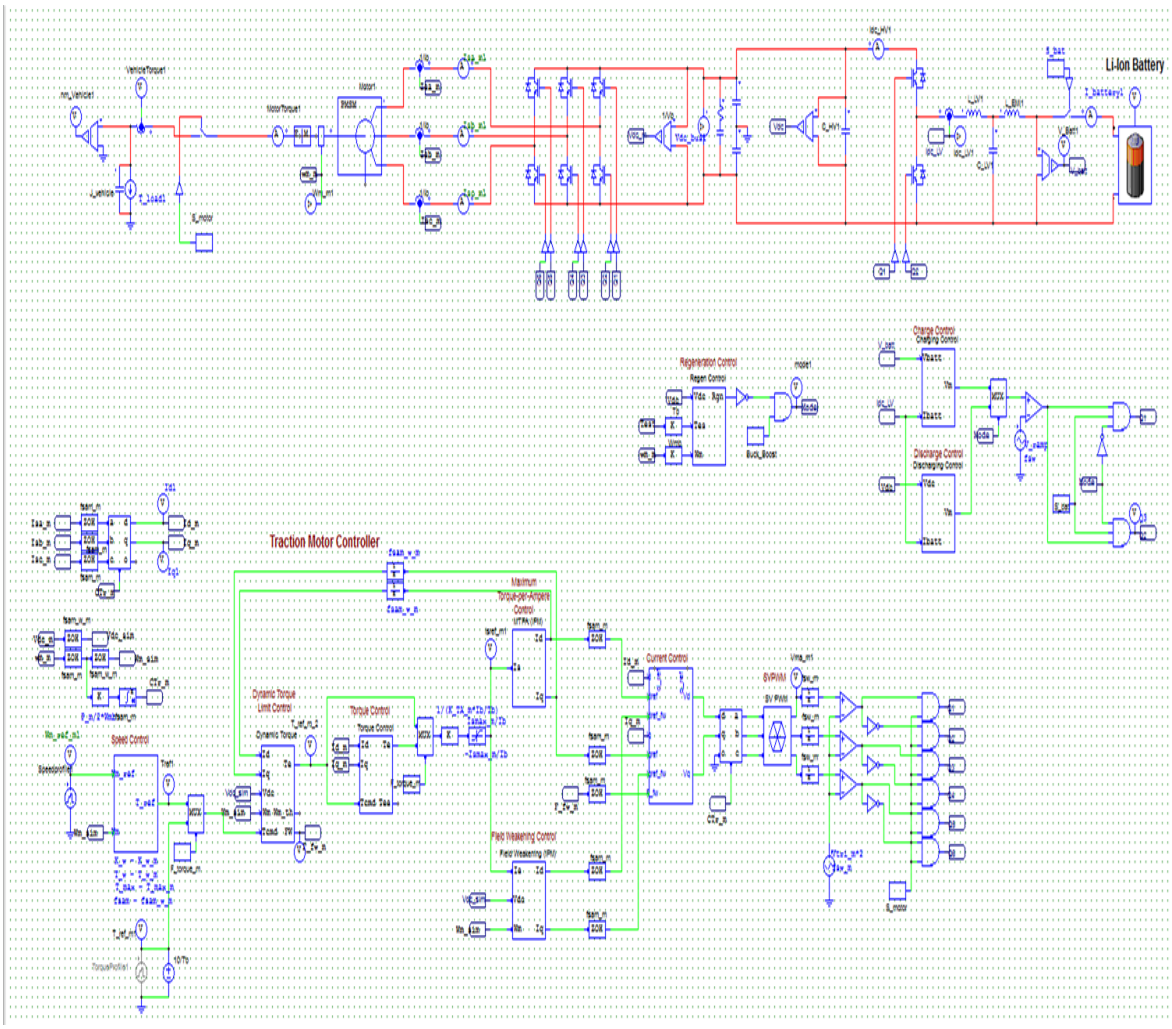

Fig. 3-10. Detailed PSIM EV model schematic (power and control circuits)

Chapter 4 : Nissan Leaf Electric Vehicle

4.1 Nissan Leaf 2016 EV Description

In this research, Nissan Leaf 2016 EV (NLEV) with a maximum torque of 254 N.m up to 160 km/h is simulated in PSIM. This is an environment friendly car with zero emissions. Nissan Leaf have a powerful EV structure with a compact high voltage unit, including an electric motor, inverter and DC/DC converter, resulting in high power density. Li-Ion battery from AESC (Automotive Energy Supply Corporation) with nominal voltage of 360 V is used to supply power to the NLEV, with two available capacities. These batteries have a single charge mileage index of up to 107 miles according to the U.S. Environmental Protection Agency (EPA) driving cycle as shown in Table 4-1. This index can go up to 155 miles for the New European Driving Cycle (NEDC) system driving cycle. Moreover, its energy consumption is 150 Wh/km. Speaking of acceleration, NLEV can go from 0 - 62 mph in 11.5 sec [73] [74].

Table 4-2. lists the NLEV maximum speeds available for different wheel sizes whereas the traction motor specifications are shown in Table 4-3.

Table 4-1. NLEV single charge mileage for each battery capacity

Battery Capacity	EPA	NEDC
24 kwh	84 miles	124 miles
30 kwh	107 miles	155 miles

Table 4-2. NLEV maximum speeds available for different wheel sizes

Tire used	Maximum speed (mph)
16”	87
17”	89

Table 4-3. NLEV traction motor specifications

Max. engine power	kW (hp) / rpm	80(109) / 3008-10000
Max. torque	Nm / rpm	254 / 0-3008
Max. rpm	rpm	10,500

A value of 200 N.m was considered as the load command on motor with no gears added; either for motoring or braking, per the assumptions section. This corresponds to a not fully loaded car, which is the normal operating case. At this loading, the motor efficiency is better than maximum torque. The curb weight of NLEV is 1500 kg whereas the Gross weight is 1945 kg.

4.2 Nissan Leaf 2016 EV Powertrain Design and Simulation

4.2.1 Traction Motor

4.2.1.1 Motor Parameters

The motor parameters for the NLEV entered to the PSIM model are listed in Table 4-4. whereas those for the 3- phase inverter controlling the motor are listed in Table 4-5.

Table 4-4. The Traction motor parameters for NLEV

Number of Poles	8
Line-to-line back EMF constant	244 V/krpm
Stator winding resistance	0.065 ohm
d-axis inductance at rated conditions	0.00085 H
q-axis inductance at rated conditions	0.01 H
moment of inertia	0.03 kg.m^2
Shaft time constant	100 sec
Maximum motor torque	254 N.m
Maximum motor power	80 kW
Maximum motor speed	10500 rpm

Table 4-5. The parameters of the motor's inverter control circuit for NLEV

Inverter switching frequency	20 kHz
PWM carrier peak amplitude	1
Inner current loop sampling frequency	20 kHz
Outer speed loop sampling frequency	5 kHz
Maximum inverter output current amplitude	200 A

4.2.1.1.1 Speed and MTPA PI Control

The PI controller constants of motor control with other dependent parameters for NLEV, obtained by trial and error, are listed in Table 4-6.

Table 4-6. Dependent parameters of motor control for NLEV

Motor	K_TA_m	3.3985
	Te_max_m	679.701
Inverter	Vsmax_m	259.808
d-axis control loop	K_d_m	3.61157
	T_d_m	0.0294769
q-axis control loop	K_q_m	18.8495
	T_q_m	0.0769231
Speed control loop	K_w_m	0.250173
	T_w_m	0.00461319

4.2.2 DC bus

The parameters characterizing the DC Bus are listed in Table 4-7.

Table 4-7. DC bus parameters

Nominal DC Bus Voltage	500 V
Minimum DC Bus Voltage	400 V
Maximum DC Bus Voltage	600 V
DC bus capacitance	0.00115 F

4.2.3 DC/DC Converter

The specifications of the DC/DC converter used for ART simulation are listed in Table 4-8.

Table 4-8. The parameters of the DC/DC Converter for NLEV

Maximum battery charging power		40 kW
Maximum battery discharging power		80 kW
Converter switching frequency	fsw	50- 300 kHz *
Low-Voltage Side Inductance	L_LV	0.0008 H
Low-Voltage Side Capacitance	C_LV	0.01 F
Carrier peak amplitude	V_ramp	1

*depends on the thermal limits of the switching semiconductor options used

4.2.3.1 Inductor Selection

The following calculations were carried according to the design equations in the previous chapter.

For NLEV:

For f > 50 kHz (minimum switching frequency in this study), Using 5% ripple limit

$$L = 0.04032 / I_{batt} = 26.81 / \text{load power}$$

For f > 50 kHz, and a value of L_LV= 0.0008 H, The current ripple will be limited to:

$\Delta I_L = (1 - V_{batt} / V_o)\, V_{batt} / L\_LV\, f = (1-360/500) * 360 / (0.0008*50000) = 2.52$ A

This ripple value is 1.88 % of rated inductor average current of 120 A for 24 kWh battery pack. This percentage will rise at low loads, but will still be lower than the 5%. However, the same inductance value will result in less ripple for higher frequencies which is a bonus for the high frequency switching WBG devices.

According to the above analysis, a value of L_LV = 0.8 mH is selected for the NLEV DC/DC converter as seen in Table 4-8.

4.2.3.2 DC/DC Converter Control

The required NLEV DC/DC converter parameters, associated symbols and values obtained using trial and error are as seen in Table 4-9.

Table 4-9. DC/DC converter parameters, associated symbols and values

loop	parameter	Symbol	Value
Current loop	PI gain	K_ca_up	0.01
	PI time constant	T_ca_up	0.002
voltage loop	PI gain	Kv_up	0.144513
	PI time constant	Tv_up	0.00397888
Regeneration control	regen power limit	P_regen	632.5

4.2.3.3 Switch selection

Based on the available supply, each switch of the two needed for the DC/DC converter require ratings as listed in Table 4-10.

Table 4-10. DC/DC converter's switch requirements for NLEV

Rating	Minimum for NLEV
DC Voltage	600 V
peak current	120 A (24 kWh)

The key characteristics comparison between the available switch options for NLEV at 25 ºC case temperature are listed in Table 4-11.

Table 4-11. Key comparison characteristics at 25 ºC case temperature for NLEV options

Device type X count	$R_{DS\ on}$(mΩ)	Qrr (nC)	V_{DS} (V)	DC I_D (A)	Ruggedness V/ns
[75] Pure Si MOSFET X 2	48 / 2	1800*2	650	120	50
[76] GaN Cascode X 2	34 / 2	304*2	600	140	150
[31] SiC ACCUFET X 1	16	1100	1200	193	50

4.2.3.4 Thermal frequency limit

The temperature rise of the junction over the module case should be limited to 125 ºC assuming the heat sink is successful to maintain 25 ºC case temperature for the 150 ºC junction temperature. Consequently, this limits the allowed power dissipation (P_{dm}) of the used transistors and diodes to the values listed below. The maximum allowed power dissipation for each switch option is calculated based on the thermal resistance from the datasheet. Those for NLEV are listed in Table 4-12. These dissipation limit determine the

maximum switching frequency for each switch option. The suggested maximum frequencies for testing in this research are in Table 4-13. For the purpose of comparison, the pure WBG transistor options were tested also at 50 kHz.

Pdm (W) = Max. allowed temperature rise (ºC) / Thermal Resistance (j-c) (ºC/W)

Table 4-12. Maximum allowed power dissipation for NLEV options

	Thermal Resistance (j-c) (ºC/W)	Pdm (W)
Pure Si MOSFET X 2	0.25 / 2	1000
GaN Cascode X 2	0.27 / 2	924
SiC ACCUFET Transistor	0.135	925.926
SiC ACCUFET Diode	0.115	1086.957

Table 4-13. Maximum test frequencies for each option

	Max. Tested frequencies (kHz)
Pure Si MOSFET X 2	50
GaN Cascode X 2	300
SiC ACCUFET	100

4.2.4 Li-Ion Battery

The specifications of Li-ion battery pack used in PSIM to simulate the 360 V 24 kWh AESC battery of the 84 miles range NLEV trim is shown in Table 4-14. This battery pack model is based on the Saft VL-34570 Rechargeable lithium-ion battery electrical characteristics as the available data. Six Saft VL-34570 are equivalent to the original NLEV battery cell from AESC. Table 4-15 show some specs of the cell from AESC. Initial battery state of charge SOC is chosen 0.5 to leave a margin for regenerative braking to charge the battery. AESC battery pack consists of 48 modules. Each module for the NLEV have 4 cells, 2 parallel x 2 series. Cell count calculations based on the Saft VL-34570 rechargeable lithium-ion battery cell is as follow:

Number of cells in series (Ns) = 360 V/3.7 V/cell = 98 cells

Number of cells in parallel (Np) = 24 kWh/ 360 V / 5.58 Ah= 12 cells

Table 4-14. Li-ion battery pack model specifications

Number of cells in series	98
Number of cells in parallel	12
Rated cell voltage	3.7 V
Full cell voltage	4.2 V
Discharge cut-off cell voltage	2.7 V
Rated cell capacity	5.4 Ah
Internal cell resistance	0.05 ohm
Maximum cell capacity	5.58 Ah
Exp. point cell voltage	3.9 V
Exp. point cell capacity	1.08 Ah
Maximum continuous current	11 A

Table 4-15. AESC battery cell specifications

Capacity	32.5 Ah
Nominal Voltage	3.75 V
Exterior Dimensions	290mm x 216mm x 787 g
Energy Density	317Wh/L 157Wh/kg

4.3 NLEV Simulation Results

4.3.1 The General Performance

Testing the system against the simple driving cycle described in Fig. 3-1, the following graphs were observed to show the main variables' trends of the powertrain system. No significant differences between different options were observed in terms of DC bus voltage, battery voltage, torque, and speed profiles. Just a slight change in battery current occurred that reflects the difference in the switch properties which is listed in the following section describing the motoring Steady state Performance. Fig. 4-1 shows the battery current during the driving cycle. As seen, the current tends to reach the first steady state around 46.65 A after half a second. After that, the braking command to 1% of the speed starts; so, the battery current oscillates between negative and positive till the new steady state point. The more time the current is positive, the more regeneration braking energy captured back into the battery. The value of this regeneration energy differs with the switch parameters within the conversion system. The regeneration energy for each switch option is listed in the regeneration section. All the waveforms have under damped transient performance. In Fig. 4-2, the battery terminal voltage decreases with loading to 382 V. As the battery current decreases with braking, the battery terminal voltage rises again to around 395 V.

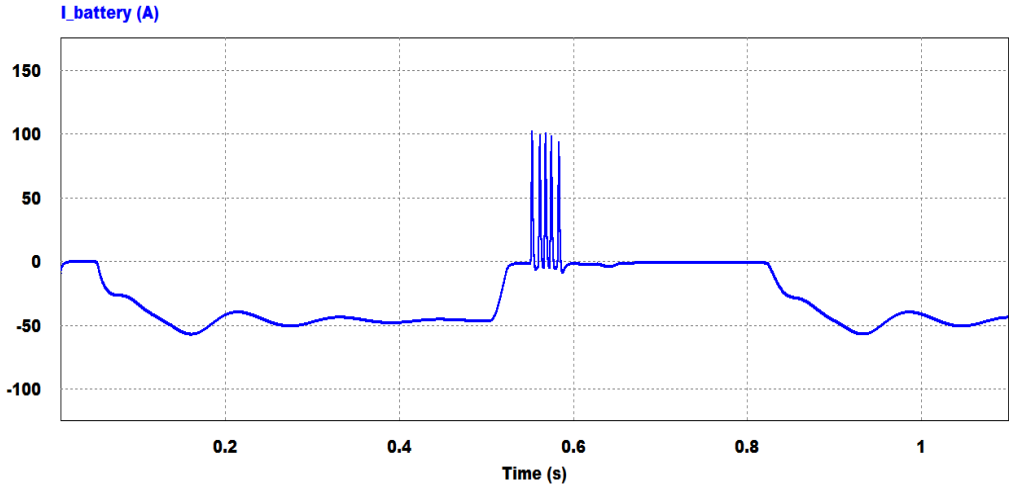

Fig. 4-1. Battery current for the whole driving cycle

During the regenerative current pulses, the battery voltage pulsates up near the maximum voltage of 412 V until after 5 pulsations it settles around 392 V. During this regeneration period, the DC link voltage pulsates between the maximum and minimum limits in opposite to the battery voltage pulsations as observed in the waveforms till it settle at 580 V. During motoring, the steady state value of the DC link voltage average value is around 500 V. Fig. 4-3 shows the battery state of charge with rise during braking.

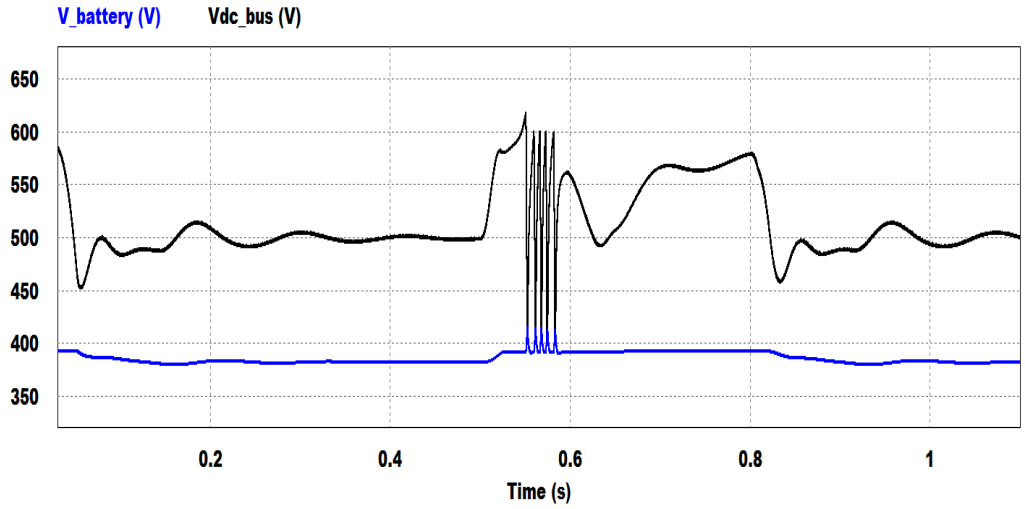

Fig. 4-2. Battery voltage and DC bus voltage during the whole driving cycle

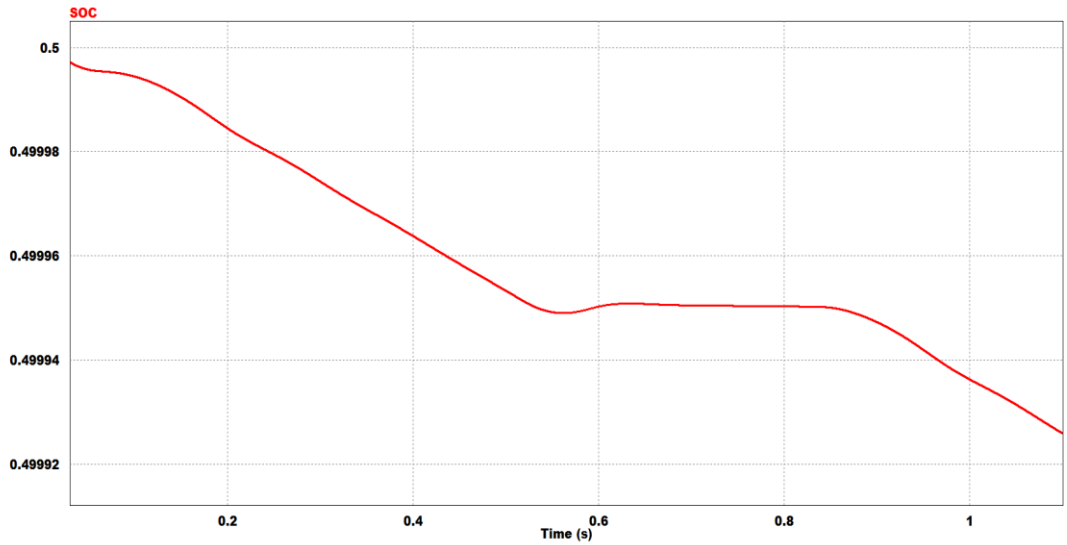

Fig. 4-3. Battery state of charge during the whole driving cycle

Regarding the motor output, the vehicle torque is as shown in Fig. 4-4. As seen, the torque have under damped behavior during both motoring and braking. The torque ripple

at the first steady state point is 4 N.m (2%) for all cases. Also the steady state for first motoring step begins around 0.5 second which is fast enough for the desired 200 N.m. value. After the braking command starts, the vehicle torque decreases, according to newton's law of motion ($J\frac{d\,\omega}{dt} = T_{developed} - T_{load}$), to 123 N.m to decrease the speed and then rise again in an under damped behaviour to reach the second motor torque steady state as the load is a constant torque, which is the same as the first, after 0.3 seconds from the braking command start. Following this braking, the motor torque increases to lift the speed again to the third steady state value while the torque settle again at 200 N.m.

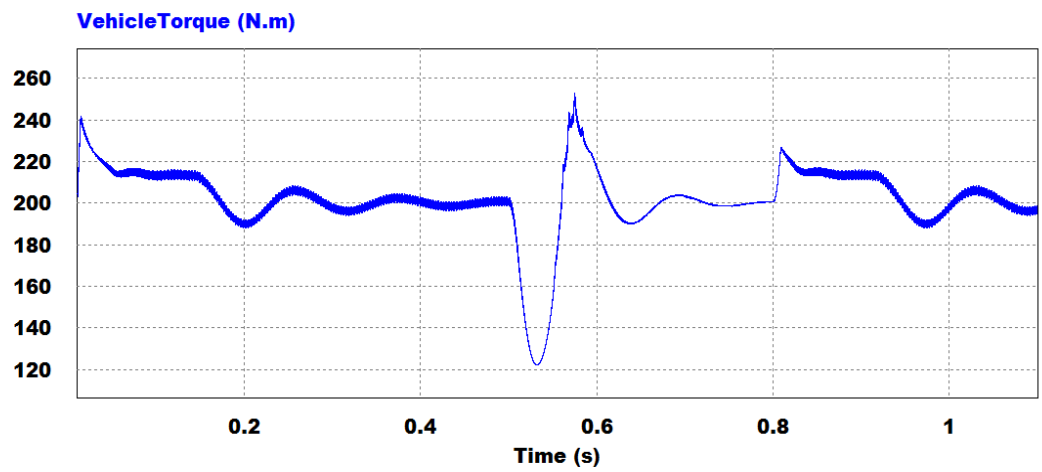

Fig. 4-4. Vehicle Torque during the whole driving cycle

Fig. 4-5 presents the motor speed trend during motoring and braking. The speed waveform successfully traced its reference during motoring, then braking, and finally motoring. As observed, the reference speed is lower than the motor threshold (base) speed through the whole driving cycle. This base speed depends on the motor parameters and fluctuate proportionally to the DC bus voltage. This means that the motor works in the MTPA region. This further indicates that the motor control is working in MTPA control mode; not the field weakening mode. This ensures maximum efficiency of the motor and its conversion system. The response of the speed control of the PMSM is very fast as observed and could reach steady state in 0.5 seconds for motoring to regular speed of 100 km/hr and 0.3 seconds for braking from this speed to 1% of it.

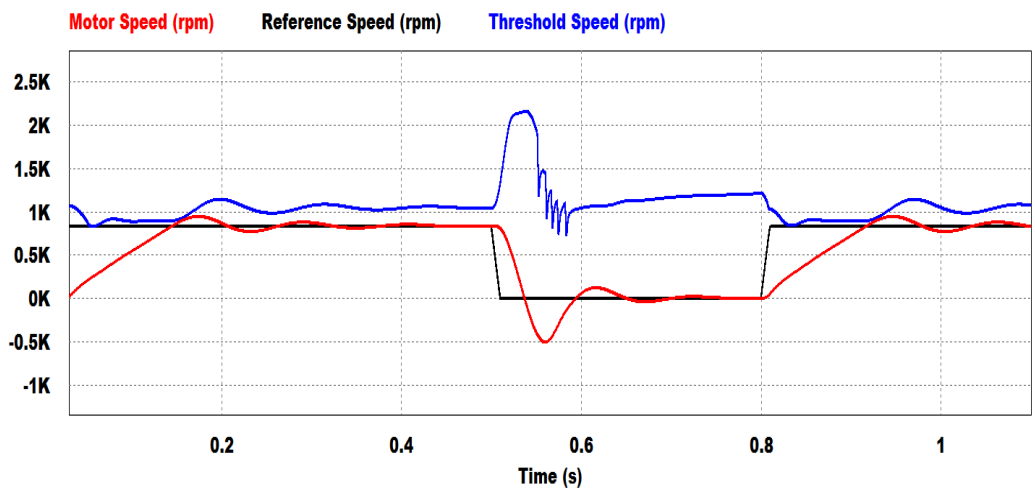

Fig. 4-5. Motor speed tracking the reference speed that is lower than the motor threshold speed through the whole driving cycle

Fig. 4-6 shows the DC/DC converter's inductor current. As seen, the current ripple is about 2 A (4.3% of 46.5 A average corresponding to 17.81 kW battery output (the tested operating point)). At higher loads, the ripple current percentage will go lower. Fig. 4-7 presents the lower motoring switch current whereas Fig. 4-8 shows the lower motoring switch voltage. The switching duty cycle measured on these graphs is 0.28 as calculated in the modelling chapter.

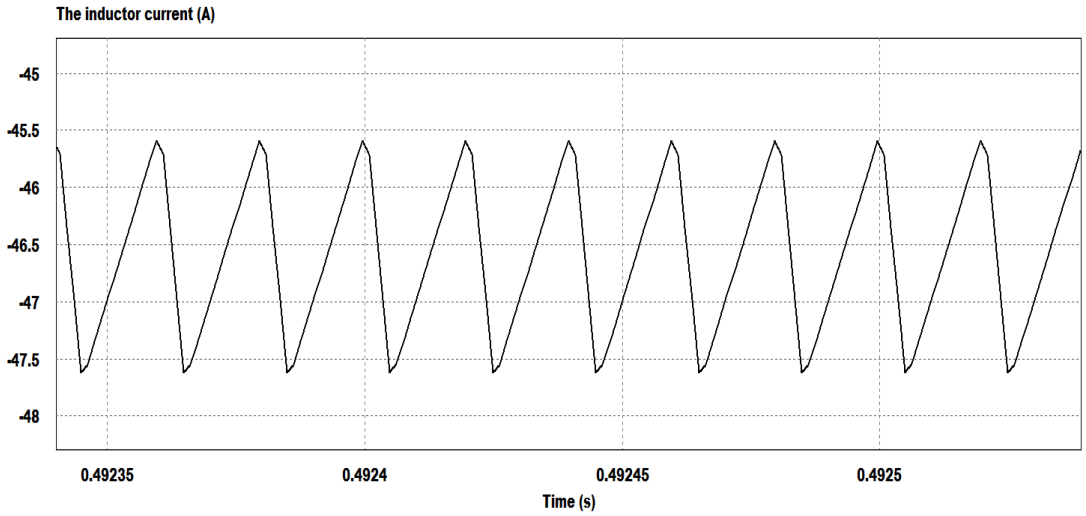

Fig. 4-6. The DC/DC converter inductor current during steady state motoring

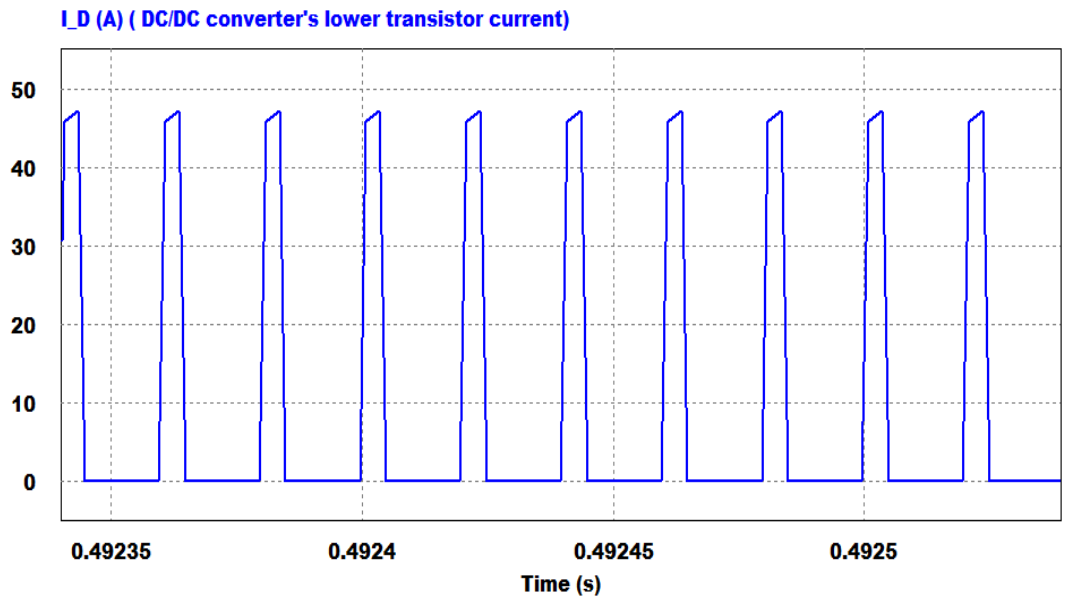

Fig. 4-7. The DC/DC converter Lower motoring switch current during steady state motoring

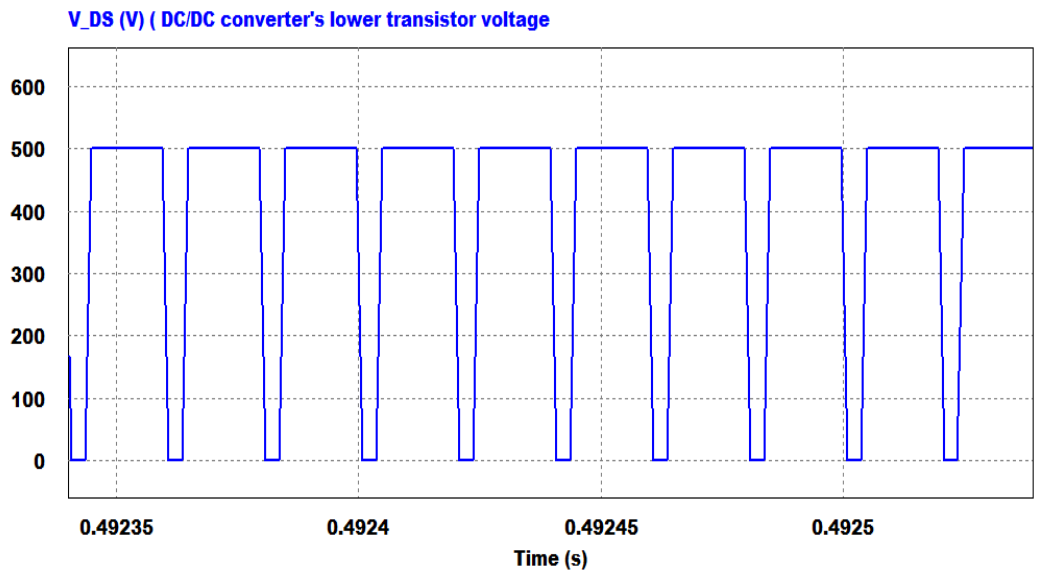

Fig. 4-8. The DC/DC converter Lower motoring switch voltage during steady state motoring

Fig. 4-9 presents the motor input 3 phase currents out of the inverter. The currents are sinusoidal with peak of 62 A at steady state motoring.

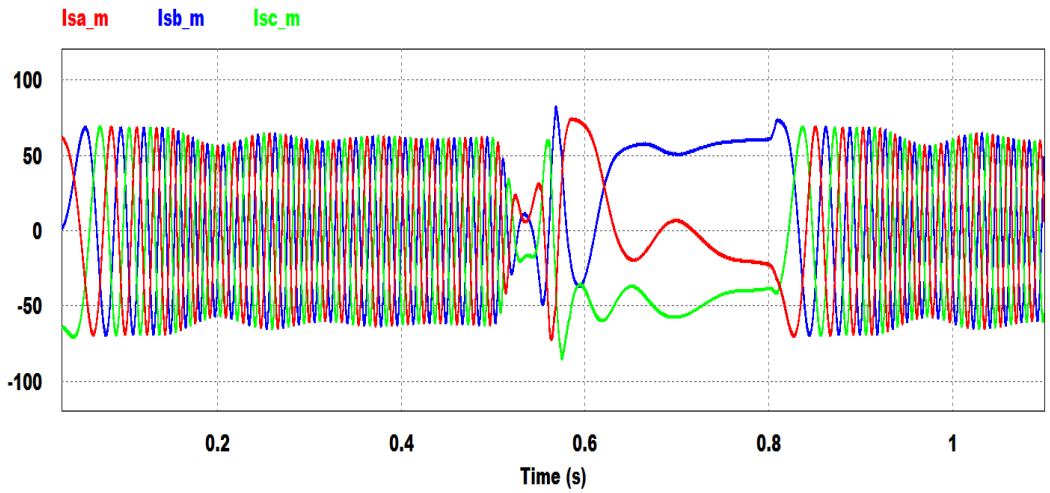

Fig. 4-9. The motor input 3- phase currents out of the inverter during the whole driving cycle

The 3- phase voltages output of the inverter are shown in Fig. 4-10 . These voltages are pulse width modulated with of RMS of 248.5 V and frequency spectrum and harmonic content as shown in Fig. 4-11. The modulation and carrier signals producing the PWM signals inputs to the inverter are captured in Fig. 4-12. The modulation signal amplitude is determined by the current control according to the reference speed and the operating conditions as illustrated in the modelling chapter. It can be observed from Fig. 4-13 that the phase sequence of the motor input 3- line-Line voltages (and the same for phase voltages) out of the inverter is reversed after the braking command as the motor transfer from motor operation mode to generator. As this happens, the phase sequence of the motor phase currents follow the phase voltages as observed in Fig. 4-9. After the braking command is applied, the phase sequence is opposed from a-b-c to a-c-b reflecting the PMSM machine transferring from operating as motor to generator mode; i.e. from first quadrant to the second as seen in Fig. 8-3 in Appendix I.

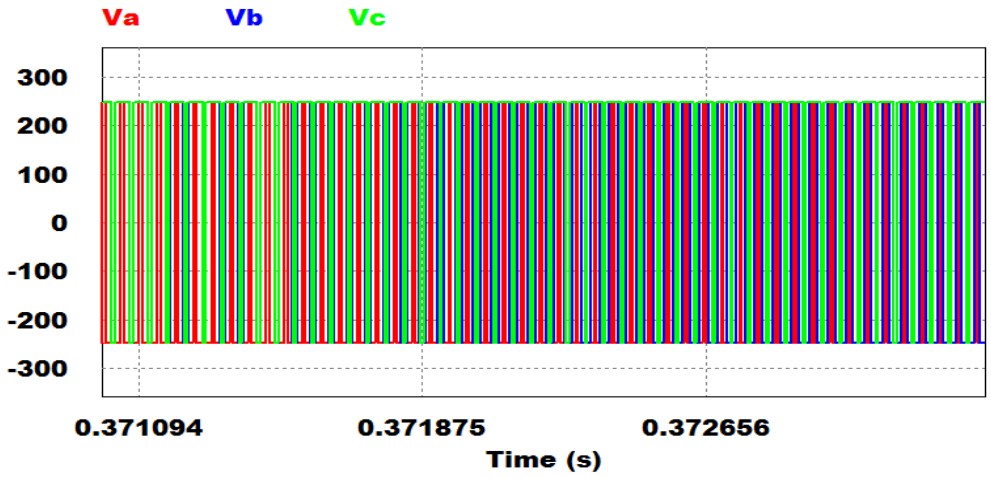

Fig. 4-10. The motor input PWM 3- phase voltages during steady state motoring

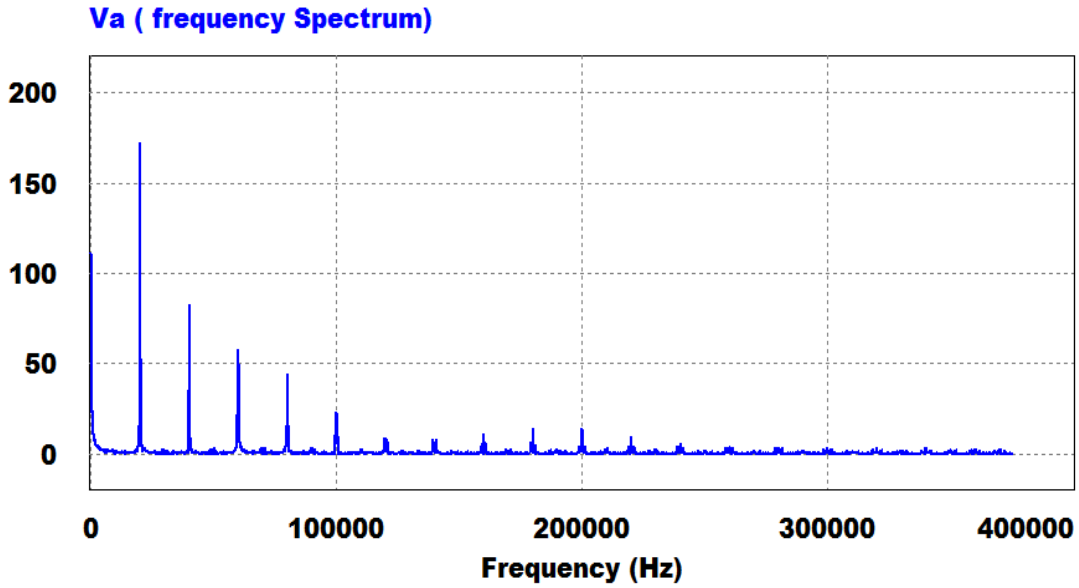

Fig. 4-11. Frequency spectrum of phase A voltage during steady state motoring

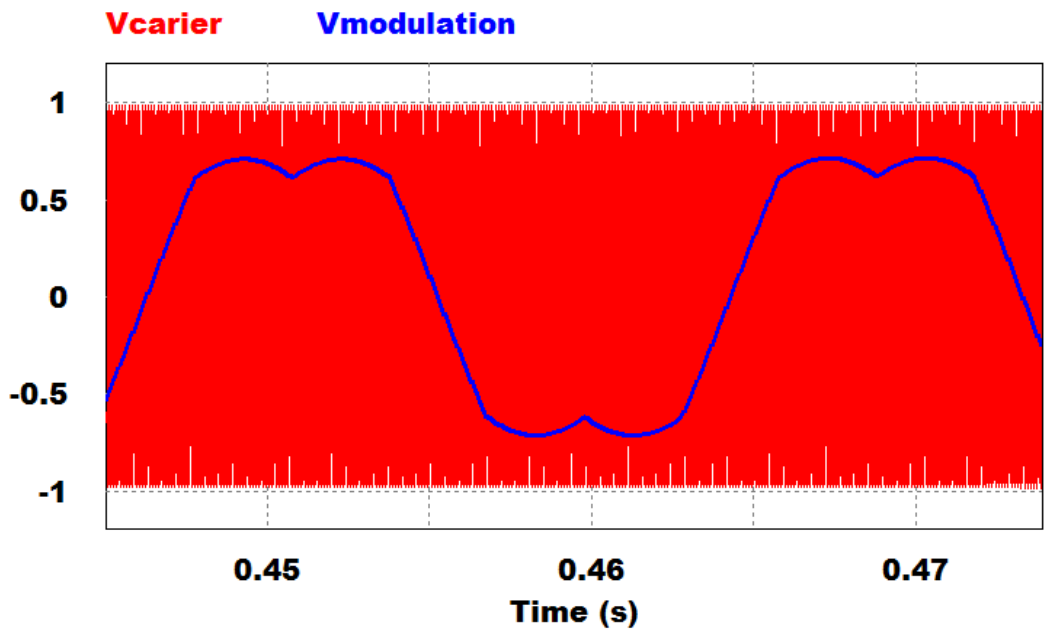

Fig. 4-12. The modulation and carrier signals producing the PWM signals inputs to the inverter during steady state motoring

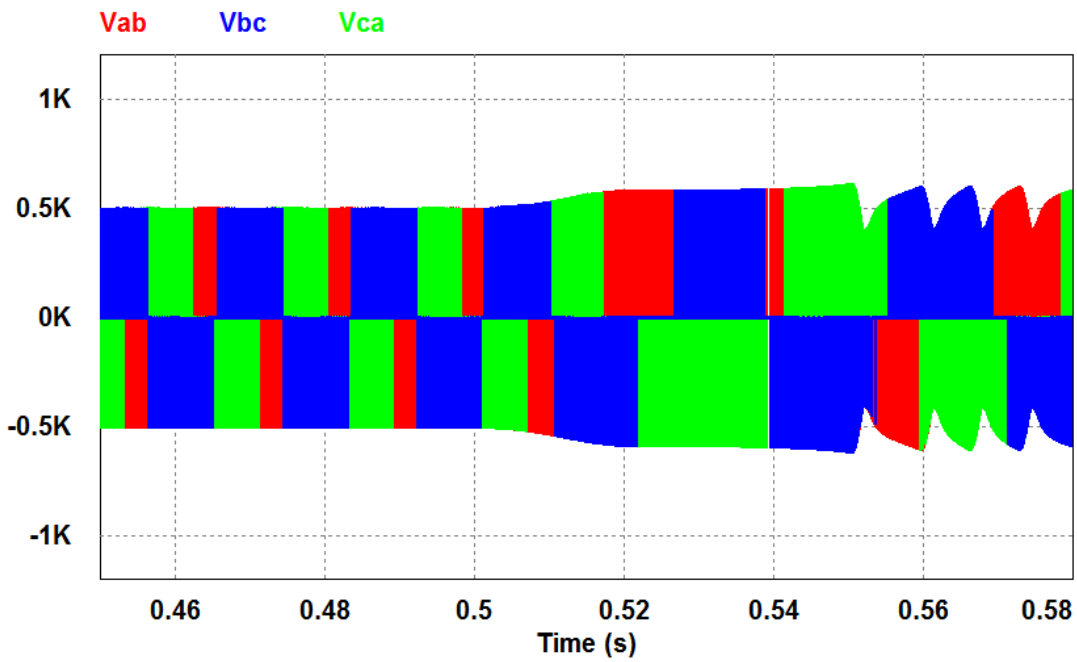

Fig. 4-13. The motor input 3- line-Line voltages out of the inverter transition from motoring through braking command showing the phase sequence reversal as the motor work as generator

4.3.2 Motoring Performance

4.3.2.1 Transient response

As seen in Fig. 4-14, the PMSM has an underdamped behavior during acceleration from standstill to the 840 rpm (88 rad/sec) motoring with appropriate overshoot and settling time for both torque and speed variables. During the positive net motor's shaft torque periods, the speed will increase (acceleration) according to newton's law of motion ($J\frac{d\,\omega}{dt} = T_{developed} - T_{load}$). As the net motor's shaft torque go ngative, deceleration happens causing decrease in speed. These fluctuations are repeated with attenuated peaks due to the friction until the system reaches its steady state point. At steady state, the net motor's shaft torque is zero and the speed is the set point (reference) of this adjustable speed drive. This reference for the first step motoring is 840 rpm (88 rad/sec) as shown in Fig. 4-14. These fluctuations are so fast with a settling time of 0.5 second. The overshoot under these conditions is 13% (12/88) and 20% (40/200) for the speed and torque respectively as calculated from the PSIM waveforms shown in Fig. 4-14.

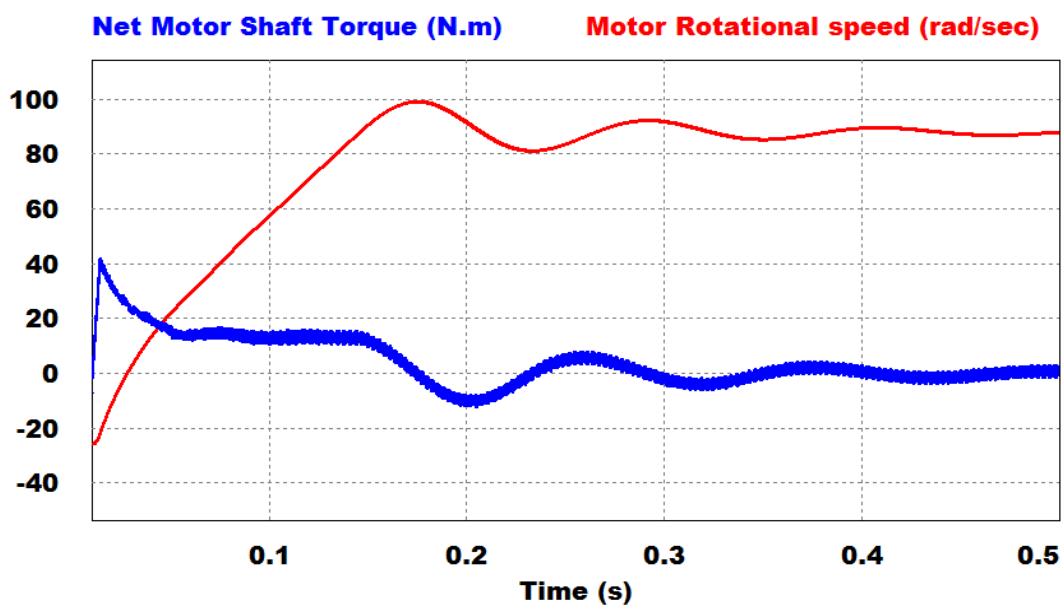

Fig. 4-14. Motor's net shaft torque and angular speed during motoring transient

4.3.2.2 Steady state Performance

As mentioned in the general performance section, no significant differences between proposed options were observed in terms of DC bus and battery voltages, torque and speed profiles. Just a slight change in battery current that reflects the difference in the switch properties. Table 4-16 lists the motoring steady state battery current at 25 ºC for 50 kHz. Table 4-17 lists those for 150 ºC and 50 kHz whereas Table 4-18 lists those for maximum frequencies tested and 25 ºC. The higher the switching frequency or the junction temperature, the higher the current drawn from the battery.

Table 4-16. Switch peak current comparison at 25 ºC for 50 kHz

GaN Cascode	46.72 A
SiC ACCUFET	46.75 A
Pure Si MOSFET	46.68 A

Table 4-17. Switch peak current comparison at 150 ºC for 50 kHz

GaN Cascode	46.762 A
SiC ACCUFET	46.778 A
Pure Si MOSFET	46.757 A

Table 4-18. Switch peak current comparison at 25 ºC for maximum suggested frequencies

GaN Cascode at 300 kHz	46.76 A
SiC ACCUFET at 100 kHz	46.78 A
Pure Si MOSFET at 50 kHz	46.68 A

4.3.3 Loss and Efficiency Comparison during Motoring

4.3.3.1 Comparison at 25 ºC and 50 kHz

4.3.3.1.1 Lower Motoring Transistor

In Fig. 4-15, a chart compares the losses, switching, conduction and total, for the proposed options in the lower motoring position where the transistor only operates during motoring. As seen, the GaN cascode transistor has a superior performance compared to the other options. Table 4-19 lists the values of these losses used in the comparison.

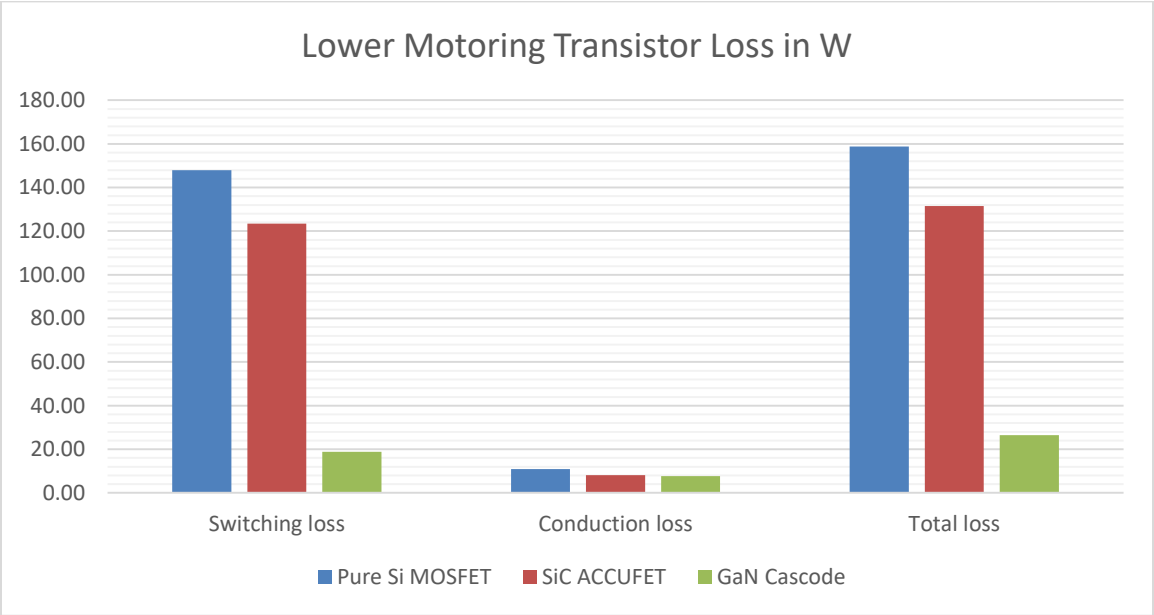

Fig. 4-15. Lower motoring transistor power loss at 25 ºC and 50 kHz

Table 4-19. Lower motoring transistor power loss at 25 ºC and 50 kHz

	Pure Si MOSFET	SiC ACCUFET	GaN Cascode
Switching loss	147.93	123.40	18.77
Conduction loss	10.93	8.16	7.64
Total loss	158.86	131.55	26.41

4.3.3.1.2 DC bus side Diode

In Fig. 4-16, a chart compares the losses, switching, conduction and total, for the proposed options for the DC bus side position where the diode only operates during motoring. As seen, the pure Si MOSFET body diode has the lower total losses, despite higher conduction loss. Hence, it has a superior performance compared to the other options. Table 4-20 lists the values of these losses used in the comparison.

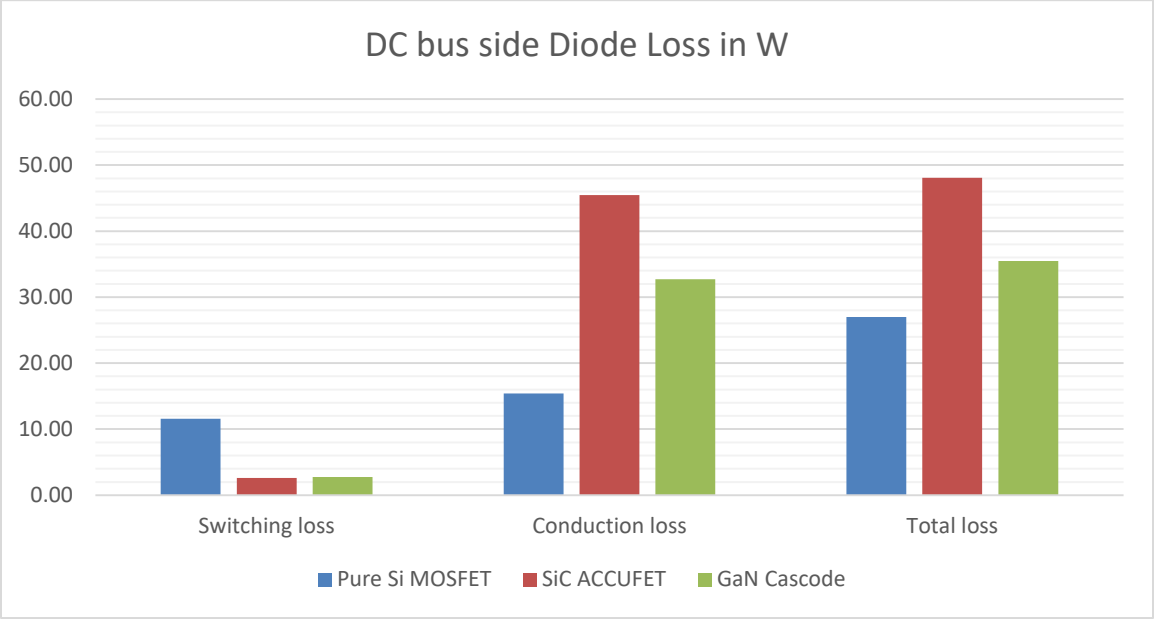

Fig. 4-16. DC bus side diode power loss at 25 ºC and 50 kHz

Table 4-20. DC bus side diode power loss at 25 ºC and 50 kHz

	Pure Si MOSFET	SiC ACCUFET	GaN Cascode
Switching loss	11.57	2.61	2.77
Conduction loss	15.40	45.44	32.72
Total loss	26.97	48.06	35.49

4.3.3.1.3 Total Converter efficiency

Despite the lower diode losses for the pure Si MOSFET as noted in Table 4-20, the total converter losses are less for the GaN cascode as seen in Table 4-21. It should be noted that the two DC/DC converter's switches should be similar for easy gate control between motoring and braking. The SiC ACCUFET scores a slightly lower losses than the pure Si MOSFET which is 3 times higher than that of the GaN options.

Table 4-21. DC/DC converter switches comparison at 25 ºC and 50 kHz

	Pure Si MOSFET	SiC ACCUFET	GaN Cascode
Losses (W)	185.86	179.65	61.91
Efficiency (%)	98.96	98.99	99.65
Heat sink size reduction (%)	--	3.2	67

4.3.3.2 Comparison at 25 ºC and different frequencies

4.3.3.2.1 Lower Motoring Transistor

In Fig. 4-17, a chart compares the losses, switching, conduction and total, for the proposed options in the lower motoring position at 25 ºC and different frequencies. As seen, the GaN cascode transistor has the lower switching losses then the pure Si MOSFET then the SiC ACCUFET. However, these options take the opposite order in terms of conduction losses. As the conduction losses are much lower than switching losses at tested frequencies, the total transistor losses are lower for GaN. Table 4-22 lists the values of all these losses used in the comparison.

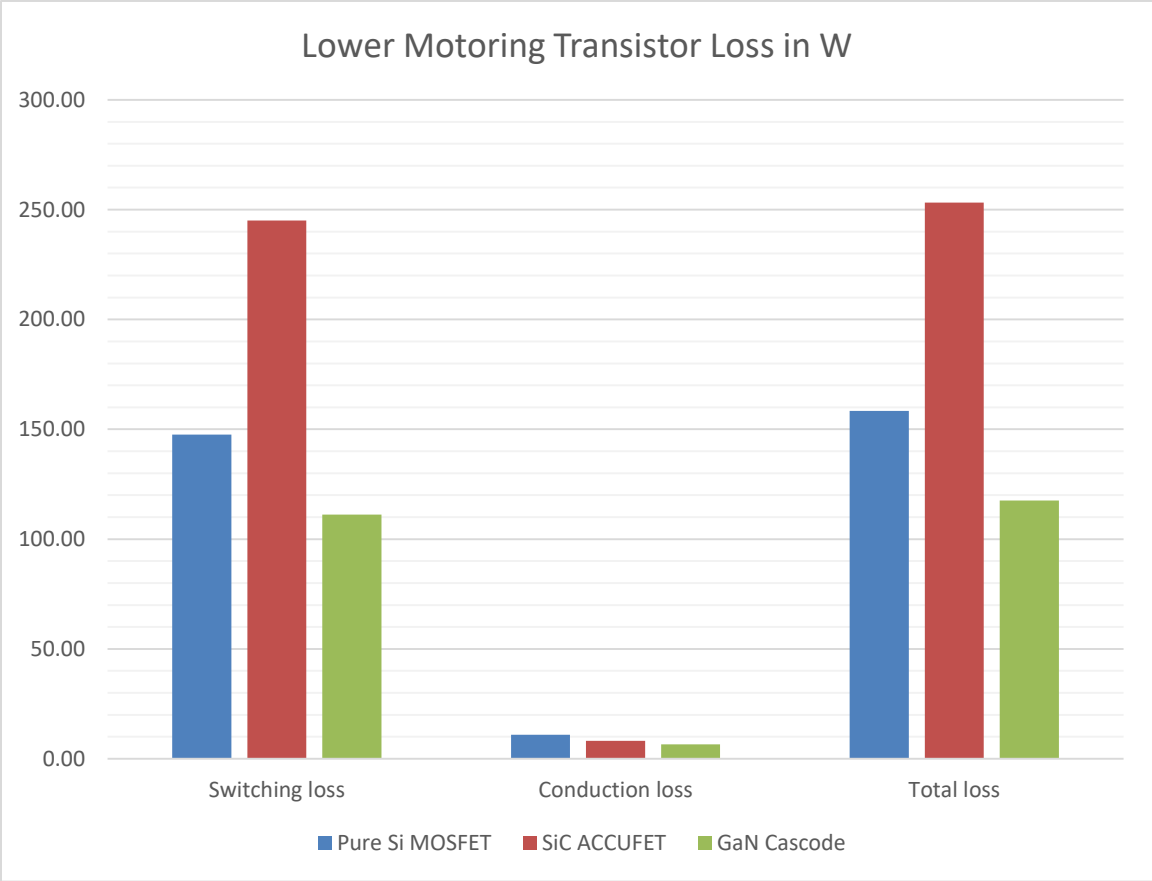

Fig. 4-17. Lower motoring transistor power loss at 25 ºC and different frequencies

Table 4-22. Lower motoring transistor power loss at 25 ºC and different frequencies

	Pure Si MOSFET	SiC ACCUFET	GaN Cascode
Switching loss	147.93	245.07	111.1
Conduction loss	10.93	8.12	6.5
Total loss	158.86	253.20	117.6

4.3.3.2.2 DC bus side Diode

In Fig. 4-18, a chart compares the losses, switching, conduction and total, for the proposed options for the DC bus side position where the diode only operates during motoring. As seen, the SiC ACCUFET body diode still has the lower switching losses even after doubling its switching frequency to 100 kHz. It should be noted that there is no difference in the pure Si MOSFET case as the switching frequency is fixed at 50 kHz. The pure Si MOSFET has the lowest conduction losses and hence lower diode total losses. Hence, it has a superior performance compared to the other options in this position. Table 4-23 lists the values of these losses used in the comparison.

Table 4-23. DC bus side diode power loss at 25 ºC and different frequencies in W

	Pure Si MOSFET	SiC ACCUFET	GaN Cascode
Switching loss	11.57	5.28	16.94
Conduction loss	15.40	45.29	34
Total loss	26.97	50.56	50.94

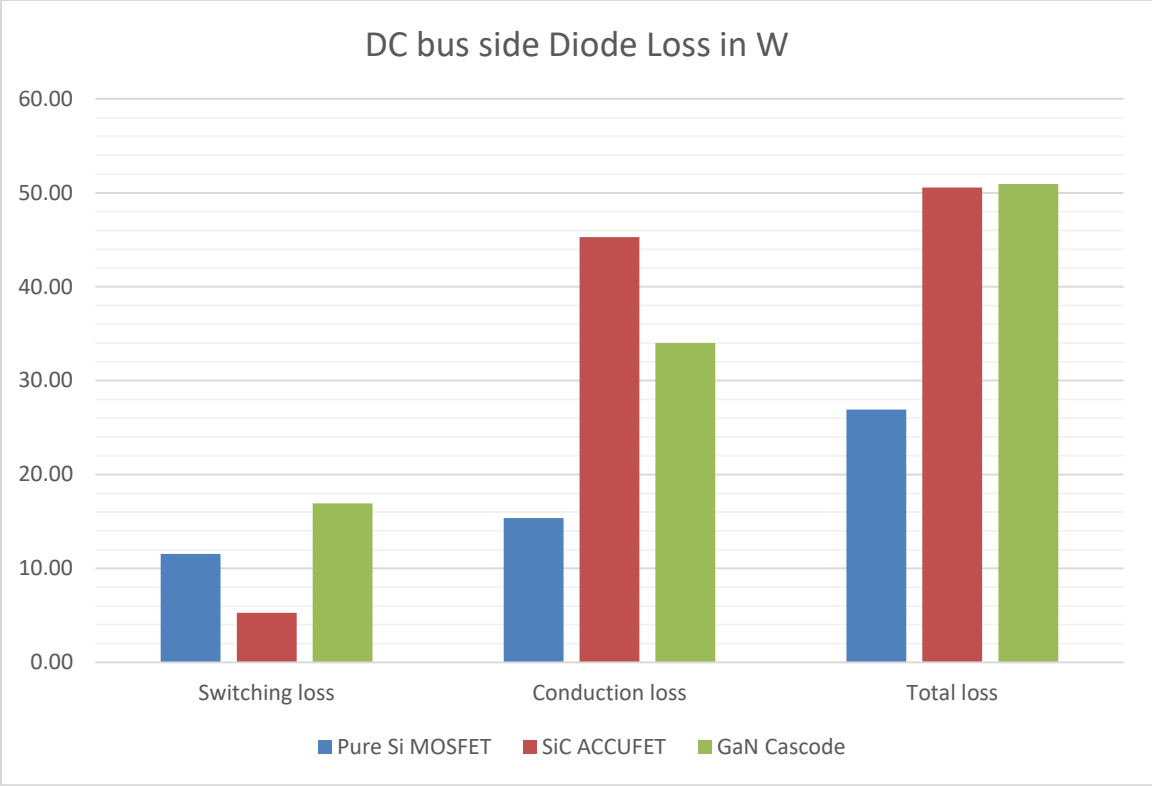

Fig. 4-18. DC bus side diode power loss at 25 ºC and different frequencies

4.3.3.2.3 Total Converter efficiency

Despite the lower transistor losses for the GaN cascode at 300 kHz as noted in Table 4-22, the pure Si MOSFET has slightly lower total losses than GaN switched at 300 kHz as seen in Table 4-24. Switching the SiC ACCUFET at 100 kHz increased the switching losses to the double approximately compared to 50 kHz. As the transistor switching losses is the dominant, SiC ACCUFET at 100 kHz is the worst choice.

Table 4-24. DC/DC converter switches comparison at 25 ºC and different frequencies

	Pure Si MOSFET	SiC ACCUFET	GaN Cascode
Losses (W)	185.32	303.76	168.54
Efficiency (%)	98.96	98.3	99.06
Heat sink size reduction (%)	--	- 64	9
Filter size reduction (%)	--	50	83

4.3.3.3 Comparison at 150 ºC and 50 kHz

4.3.3.3.1 Lower Motoring Transistor

In Fig. 4-19, a chart compares the losses, switching, conduction and total, for the proposed options in the lower motoring position at 150 ºC and 50 kHz. As seen, the GaN cascode transistor is the most promising option with the increase in junction temperature compared to the other options. Following GaN comes SiC ACCUFET then pure Si MOSFET. The pure Si MOSFET isn't a good candidate for high junction temperatures. Table 4-25 lists the values of these losses used in the comparison.

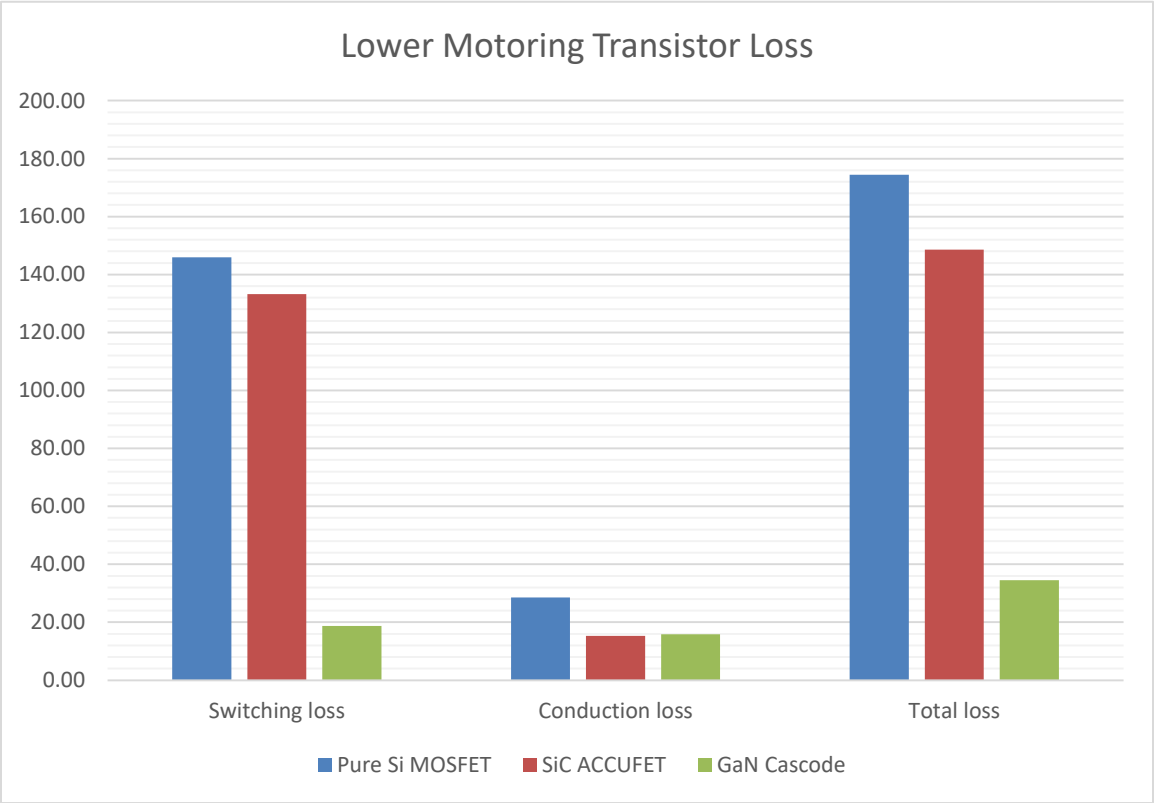

Fig. 4-19. Lower motoring transistor power loss at 150 ºC and 50 kHz

Table 4-25. Lower motoring transistor power loss at 150 ºC and 50 kHz

	Pure Si MOSFET	SiC ACCUFET	GaN Cascode
Switching loss	145.89	133.26	18.75
Conduction loss	28.56	15.30	15.82
Total loss	174.45	148.56	34.57

4.3.3.3.2 DC bus side Diode

In Fig. 4-20, a chart compares the losses, switching, conduction and total, for the proposed options for the DC bus side position at 150 ºC and 50 kHz. As seen, the pure Si MOSFET body diode still has the lower conduction loss and total losses even with higher junction temperature, despite higher switching loss. Hence, it has a superior performance compared to the other options in this position. Table 4-26 lists the values of the losses used in this comparison.

Table 4-26. DC bus side diode power loss at 150 ºC and 50 kHz

	Pure Si MOSFET	SiC ACCUFET	GaN Cascode
Switching loss	11.56	2.61	2.89
Conduction loss	27.60	43.28	48.38
Total loss	39.16	45.89	51.26

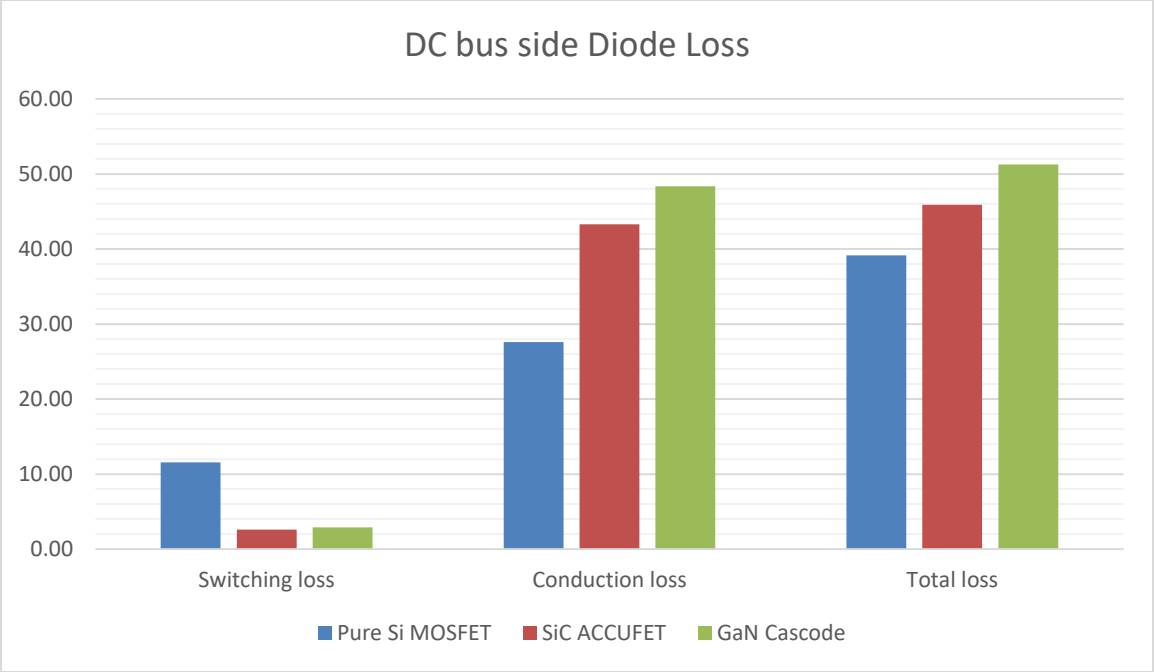

Fig. 4-20. DC bus side diode power loss at 150 ºC and 50 kHz

4.3.3.3.3 Total Converter efficiency

Similarly as 25 ºC, despite the diode losses is lowest for the pure Si MOSFET at 150 ºC and 50 kHz as noted in Table 4-26, the total converter losses are less for the GaN cascode switching at 50 kHz as seen in Table 4-27. The SiC ACCUFET scores the second then the pure Si MOSFET at the end with 0.1% efficiency difference only. Due to high switching losses, the pure Si MOSFET isn't a good candidate for high junction temperatures which is more practical case than 25 ºC.

Table 4-27. DC/DC converter switches comparison at 150 ºC and 50 kHz

	Pure Si MOSFET	SiC ACCUFET	GaN Cascode
Losses (W)	213.61	194.45	85.83
Efficiency (%)	98.8	98.91	99.52
Heat sink size reduction (%)	--	9	60

4.3.3.4 Comparison at 150 ºC and different frequencies

4.3.3.4.1 Lower Motoring Transistor

In Fig. 4-21, a chart compares the losses, switching, conduction and total, for the proposed options in the lower motoring position at 150 ºC and different frequencies. As the switching frequencies increase for the WBG options, the switching losses increase proportionally approximately. For SiC ACCUFET, the switching losses reach a value more than pure Si MOSFET unlike GaN. As seen, the GaN cascode transistor has a superior performance compared to the other options in terms of the dominant switching losses, hence the total transistor losses. Table 4-28 lists the values of these losses used in this comparison.

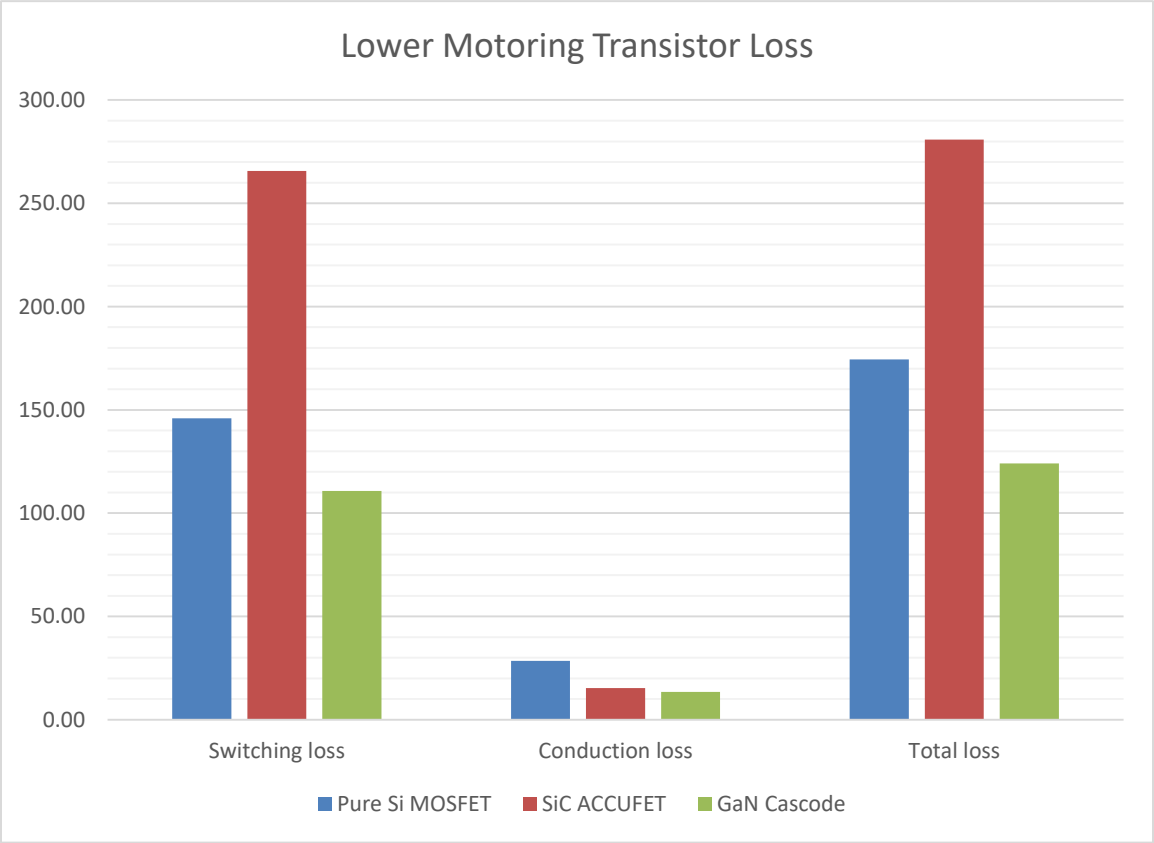

Fig. 4-21. Lower motoring transistor power loss at 150 ºC and different frequencies

Table 4-28. Lower motoring transistor power loss at 150 ºC and different frequencies

	Pure Si MOSFET	SiC ACCUFET	GaN Cascode
Switching loss	145.89	265.63	110.69
Conduction loss	28.56	15.3	13.46
Total loss	174.45	280.93	124.15

4.3.3.4.2 DC bus side Diode

In Fig. 4-22, a chart compares the losses, switching, conduction and total, for the proposed options for the DC bus side position at 150 ºC and different frequencies. As seen, the pure Si MOSFET body diode has the lower dominant conduction losses, hence total losses. Table 4-29 lists the values of the losses used in this comparison.

Table 4-29. DC bus side diode power loss at 150 ºC and different frequencies

	Pure Si MOSFET	SiC ACCUFET	GaN Cascode
Switching loss	11.56	5.27	17.61
Conduction loss	27.6	43.28	50.13
Total loss	39.16	48.55	67.74

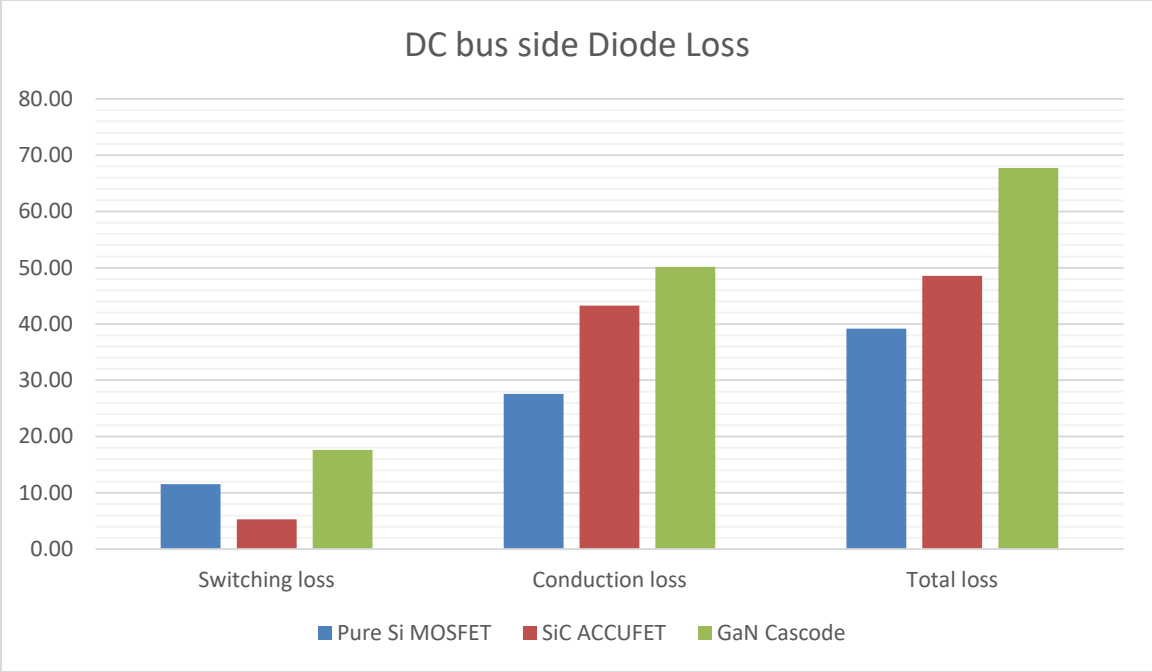

Fig. 4-22. DC bus side diode power loss at 150 ºC and different frequencies

4.3.3.4.3 Total Converter efficiency

Despite the lower diode losses for the pure Si MOSFET as noted in Table 4-29, the total converter losses are less for the GaN cascode as seen in Table 4-30. The SiC ACCUFET scores the highest losses as its switching losses is the highest. SiC losses is 80% higher than pure Si MOSFET and 140% higher than the GaN options.

Table 4-30. DC/DC converter switches comparison at 150 ºC and different frequencies

	Pure Si MOSFET	SiC ACCUFET	GaN Cascode
Losses (W)	213.61	329.48	191.1
Efficiency (%)	98.80	98.16	98.92
Heat sink size reduction (%)	--	- 54	10.33
Filter size reduction (%)	--	50	83

4.3.3.5 Summary

The following tables summarize the comparison between available options based on junction temperature and switching frequency. Fig. 4-23. summarizes the efficiencies of all NLEV cases studied.

Table 4-31. NLEV powertrain's DC/DC converter efficiencies for 50 kHz

	Pure Si MOSFET	SiC ACCUFET	GaN Cascode
25 ºC	98.96	98.99	99.65
150 ºC	98.8	98.91	99.52

Table 4-32. NLEV powertrain's DC/DC converter efficiencies for the suggested different frequencies

	Pure Si MOSFET	SiC ACCUFET	GaN Cascode
25 ºC	98.96	98.3	99.06
150 ºC	98.8	98.16	98.92

Table 4-33. NLEV powertrain's DC/DC converter efficiencies for 25 ºC

Switching frequency	Pure Si MOSFET	SiC ACCUFET	GaN Cascode
50 kHz	98.96	98.99	99.65
maximum	98.96	98.3	99.06

Table 4-34. NLEV powertrain's DC/DC converter efficiencies for 150 ºC

Switching frequency	Pure Si MOSFET	SiC ACCUFET	GaN Cascode
50 kHz	98.8	98.91	99.52
maximum	98.8	98.16	98.92

Fig. 4-24. Summary of Efficiencies

Table 4-35 and Table 4-36 lists the conversion efficiency differences for SiC and GaN options from pure Si MOSFET peer for 50 kHz and suggested maximum frequencies respectively. Table 4-37 summaries the differences in conversion efficiency for SiC from that of GaN option.

Table 4-35. Efficiencies difference from pure Si MOSFET for 50 kHz

	SiC ACCUFET	GaN Cascode
25 ºC	0.03	0.69
150 ºC	0.11	0.72

Table 4-36. Efficiencies difference from pure Si MOSFET for different frequencies

	SiC ACCUFET	GaN Cascode
25 ºC	- 0.34	0.14
150 ºC	- 0.64	0.12

Table 4-37. Efficiencies difference for SiC from GaN

Switching frequency	25 ºC	150 ºC
50 kHz	-0.66	-0.61
Maximum	-0.76	-0.76

Regenerative braking to 1% of regular speed

As seen in the general performance section, the regeneration occurs within the 0.1 second following the braking command at 0.5 second for 0.1 second and end around 0.7 second from the drive cycle start. This time waiting is for the regenerative power to reach the threshold of regeneration control as described in the Regeneration Control section. Table 4-38 summarizes the average power regenerated back to the battery over the regeneration time period at 25 ºC for the suggested maximum frequencies in KW and percentage of motoring input power. The GaN cascode option recovered more power back into the battery, then the pure Si MOSFET, and finally the SiC ACCUFET with the same order of efficiency seen in Table 4-33.

Table 4-38. Average power regenerated back to the battery for 25 ºC at suggested maximum frequencies

GaN Cascode at 300 kHz	7.88 kW	45.03 %
SiC ACCUFET at 100 kHz	6.9 kW	39.43 %
Pure Si MOSFET at 50 kHz	7.1 kW	40.57 %

Fig. 4-25 describes the PMSM angular speed trend with the applied net braking torque. It can be observed that the PMSM has an underdamped behavior during decceleration from the normal speed of 840 rpm (88 rad/sec) down to 1% this speed of 8.4 rpm (0.88 rad/sec). As seen, the PMSM still posses appropriate overshoot and settling time for both torque and speed variables. The net motor's shaft torque fluctuates around zero during transient periods. During the negative net torque periods, the speed will decrease (decceleration) according to newton's law of motion ($J\frac{d\,\omega}{dt} = T_{developed} - T_{load}$). As the net motor's shaft torque go negative, the motor decelerates causing decrease in speed. The torque and speed continue fluctuating with attenuated peaks (under damped response) due to the friction and the selected PI values until the system reaches its steady state point. At steady state, the net motor's shaft torque is zero and the speed reaches the setpoint

(reference) of the adjustable speed drive, which for the second step is 8.4 rpm (0.88 rad/sec), after 0.3 seconds as shown in Fig. 4-25. The torque overshoot under these regenerative braking conditions is 25% (50/200) as calculated from the PSIM waveform shown.

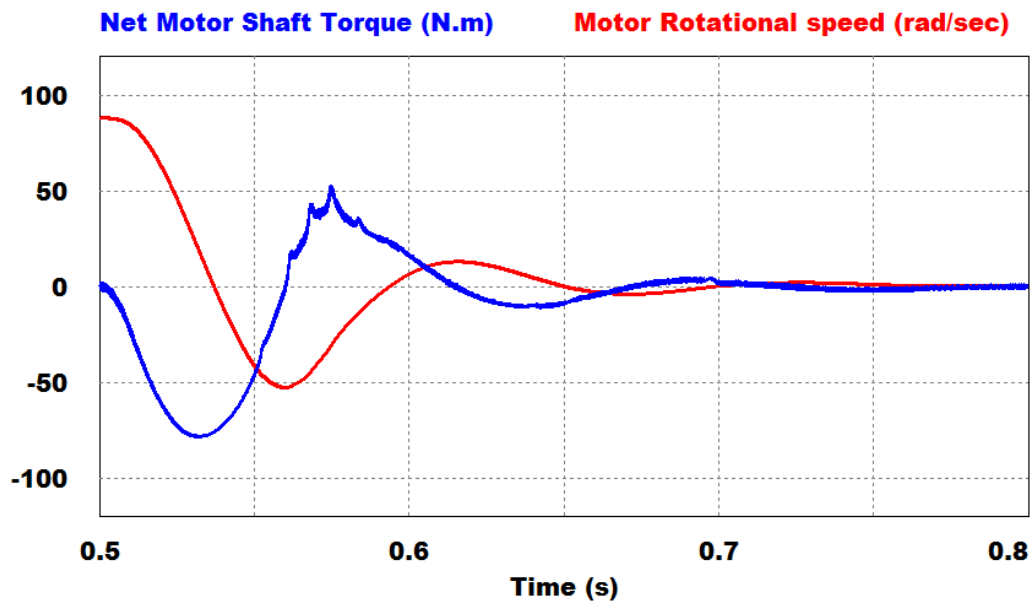

Fig. 4-25. Motor's net shaft torque and angular speed during braking transient

The torque and speed curves are further investigated in the next sections. These sections present the regenerative related waveforms for every NLEV semiconductor option for the cases in Table 4-33.

4.3.3.6 Pure Si MOSFET

Fig. 4-26 shows the battery current and voltage pulsations during regenerative braking for Pure Si MOSFET option whereas Fig. 4-27 shows the battery SOC ramping up within the period after the regeneration pulses are initiated. Fig. 4-28 shows the relation between the voltages of the LV and HV sides of the DC/DC converter during the regeneration braking for this case. Fig. 4-29 and Fig. 4-30 show the vehicle torque and motor speed respectively during braking. After the braking command started, the battery current ramp up from negative toward zero and the DC bus voltage rose till the regeneration threshold is reached and a regenerative pulse starts, i.e. the battery current is positive (back into the

battery). As the battery positive current ramp up, the battery voltage pulsate up opposite to the DC bus voltage which had high pulsations during regenerative braking as seen in Fig. 4-26 and Fig. 4-28. When a regenerative pulse goes down, the opposite occurs; this is that the battery voltage goes down while the DC bus voltage rises rapidly while the DC bus capacitor charges from the generator output through the inverter. When the regeneration threshold is reached again, the DC bus capacitor discharges again through the DC/DC converter charging the battery. This causes the battery to have a new pulsation phase in current and voltage. This pattern continues till the PMSM reaches the new mechanical equilibrium point at 8.4 rpm and the torque settles again at the load torque of 200 N.m as seen in Fig. 4-25, Fig. 4-29 and Fig. 4-30. This means that the motor's shaft net torque reached zero as any kinetic energy difference between 1st and 2nd steady state points is either dissipated as losses in the powertrain circuit or recovered back in to the battery.

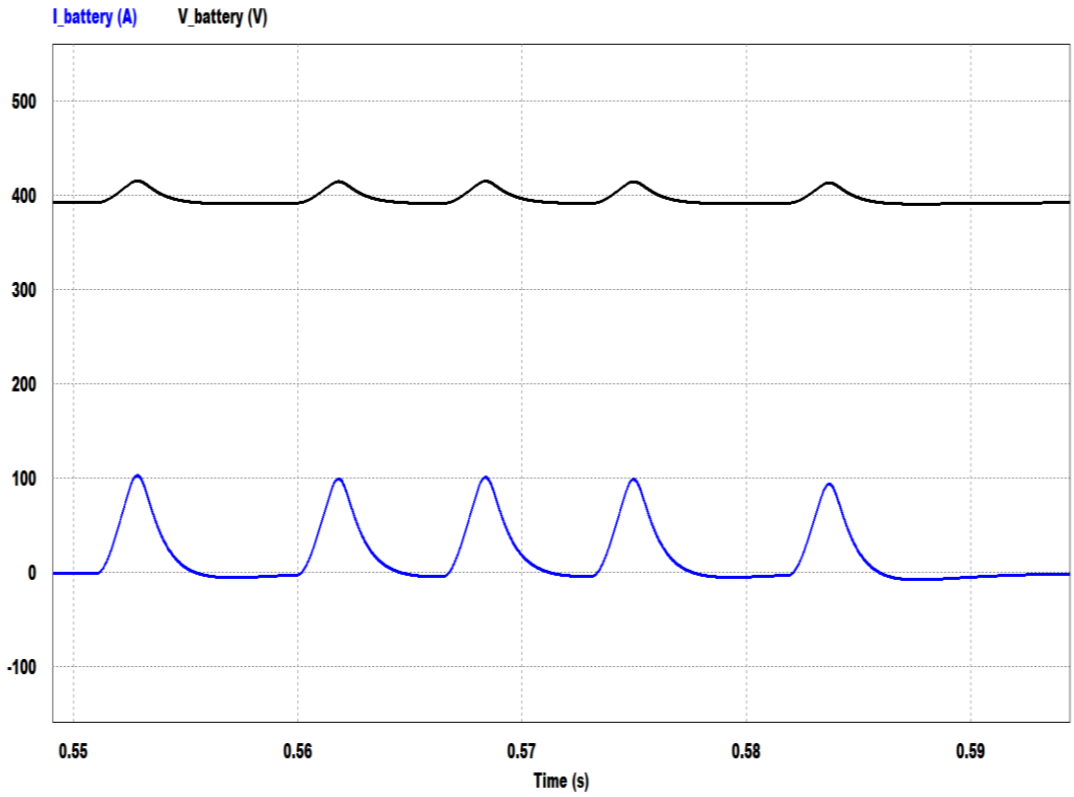

Fig. 4-26. Battery current and voltage during regenerative braking for Pure Si MOSFET option

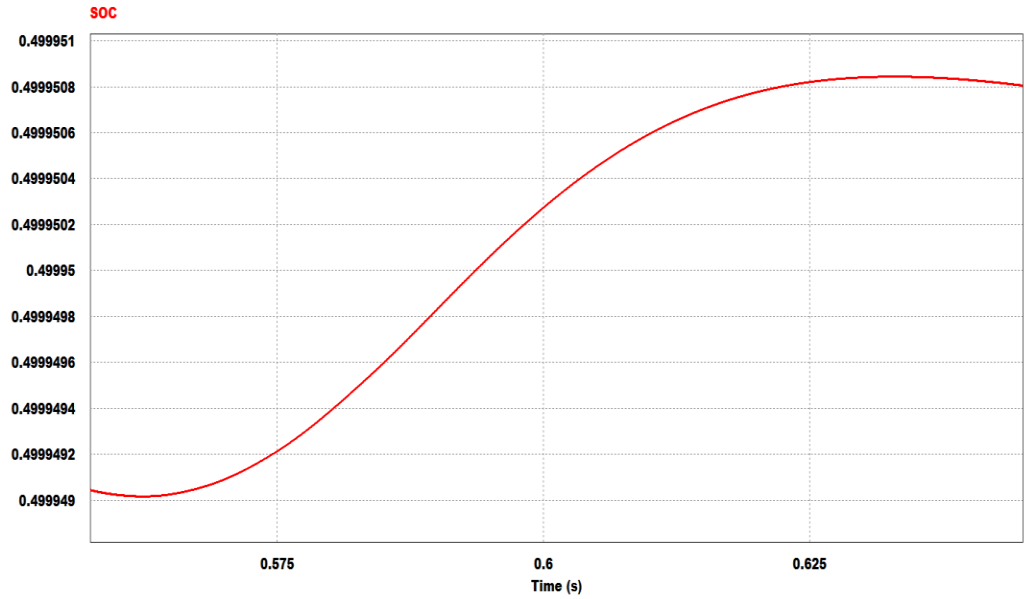

Fig. 4-27. Battery state of charge during regenerative braking for Pure Si MOSFET option

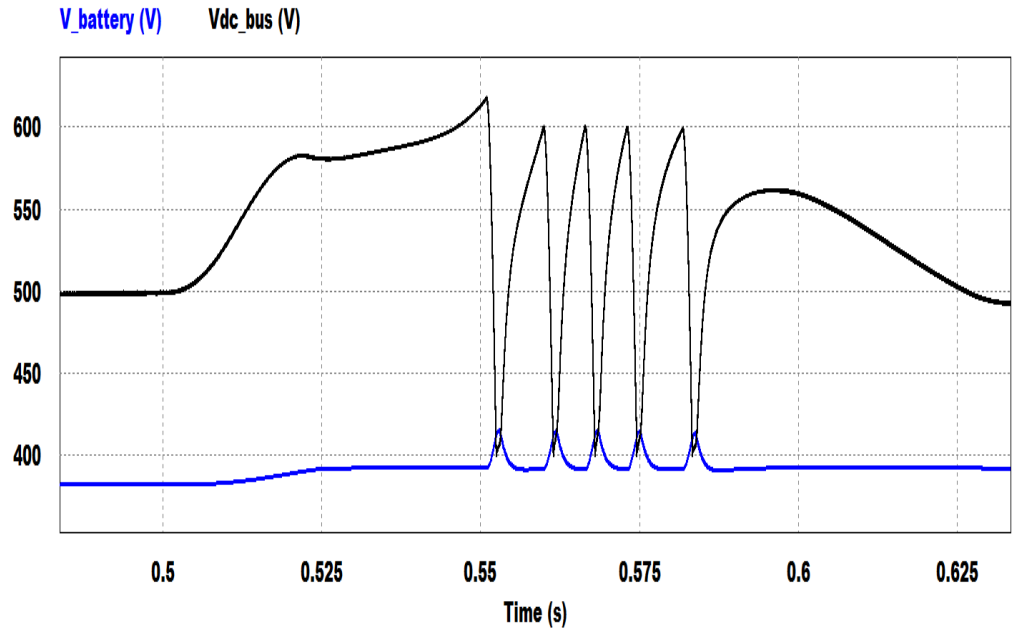

Fig. 4-28. Battery and DC bus voltages during regenerative braking for Pure Si MOSFET option

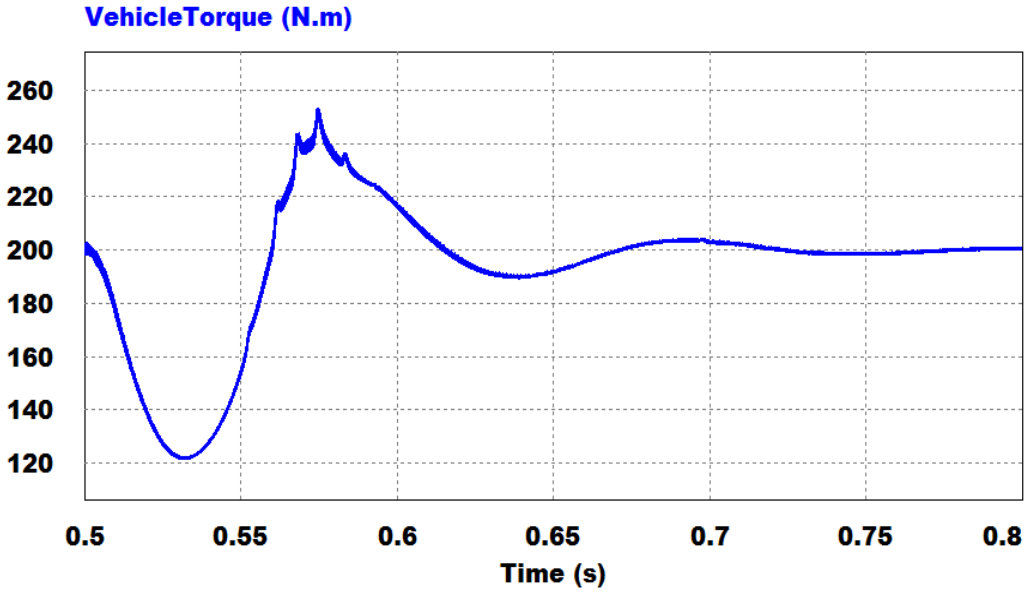

Fig. 4-29. Vehicle torque during braking for pure Si MOSFET

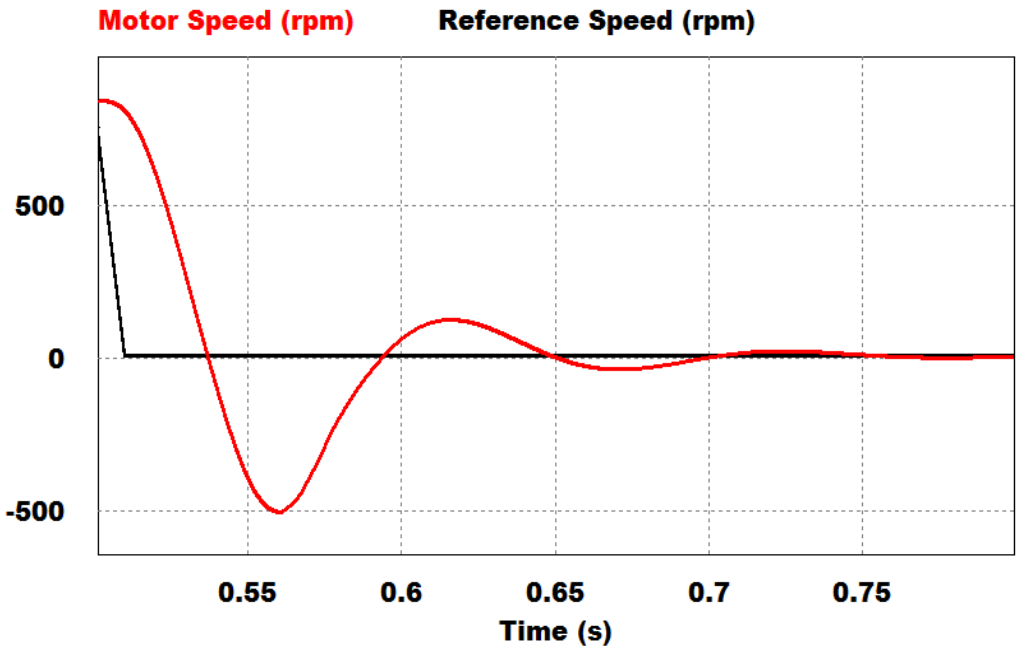

Fig. 4-30. Motor speed during braking for pure Si MOSFET

Because of the charging and discharging actions during regenerative braking, the output voltage of the PMSM generator oscillates in a same manner as the DC bus voltage as shown in Fig. 4-31.

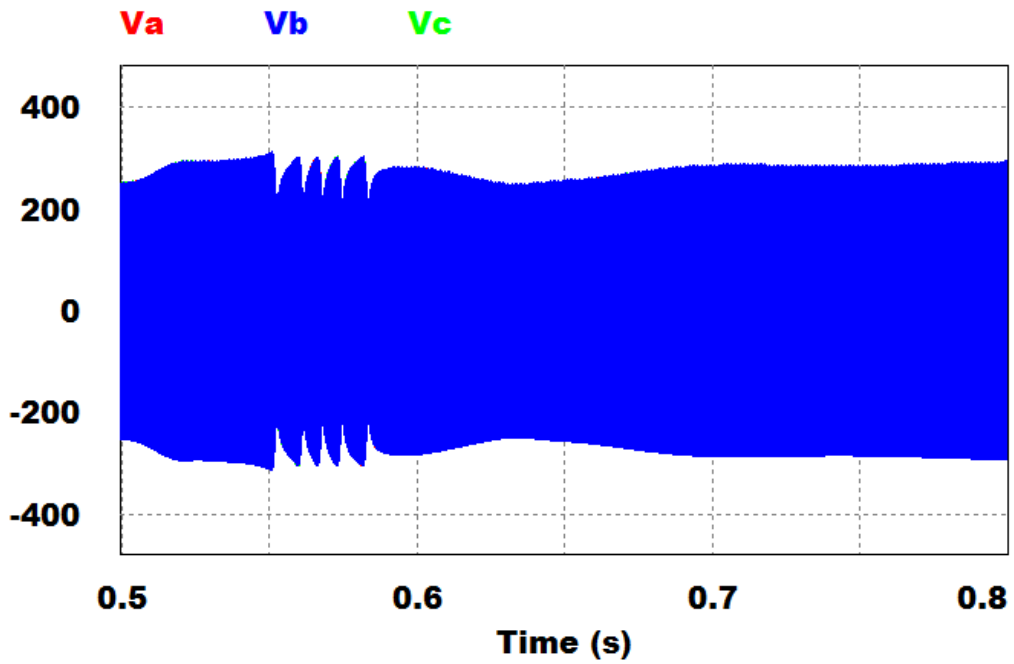

Fig. 4-31. Phase voltages output of the motor drive's inverter for pure Si MOSFET

Fig. 4-32 observes the DC/DC converter's lower motoring switch waveforms, voltage and current, during the first regeneration pulse for Pure Si MOSFET option. As shown, while the current pulse is ramping up, the DC bus transistor turn on and the DC/DC converter operate in the buck mode charging the battery. As the pulse reaches its peak, the motoring transistor turn on again suppling power from the battery to the DC bus. The net average power during the regenerative pulses period is positive (back into battery) as seen in Table 4-38.

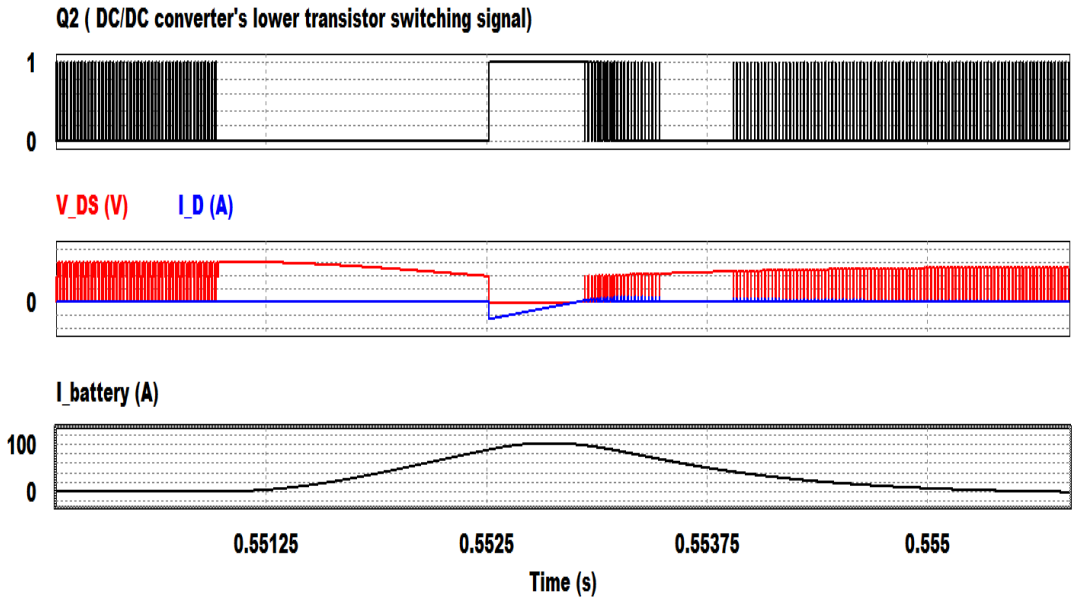

Fig. 4-32. DC/DC converter motoring switch signal, voltage and current during first regeneration pulse for Pure Si MOSFET option

In Fig. 4-33, the motoring switch losses and the DC bus side switch losses pulses are presented for the pure Si MOSFET option. The DC bus switch loss pulses reach a value from 1240 to 1415 W. The loss pulses for the motoring switch are around 240 W but are wider than the DC bus side. The division of these loss values are shown in Fig. 4-34 and Fig. 4-35 for the DC bus switch and motoring switch respectively. The losses for each switch at the second steady state point is 1.5 W and 6 W for DC bus side and motoring switches respectively.

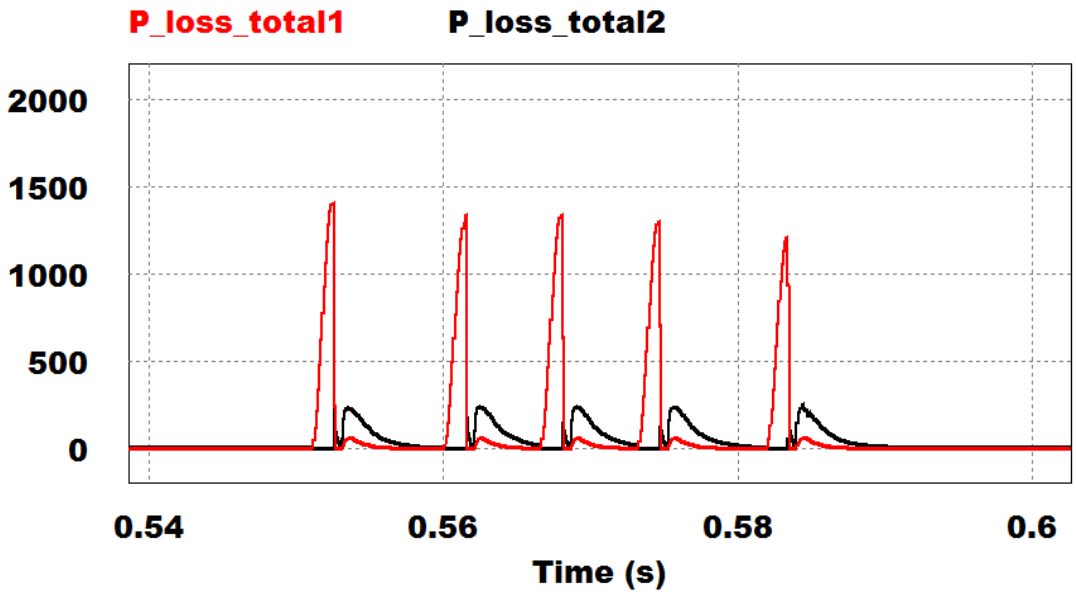

Fig. 4-33. Power losses during regenerative braking for the DC/DC converter switches for Pure Si MOSFET option; 1: DC bus side switch, 2: Lower motoring switch

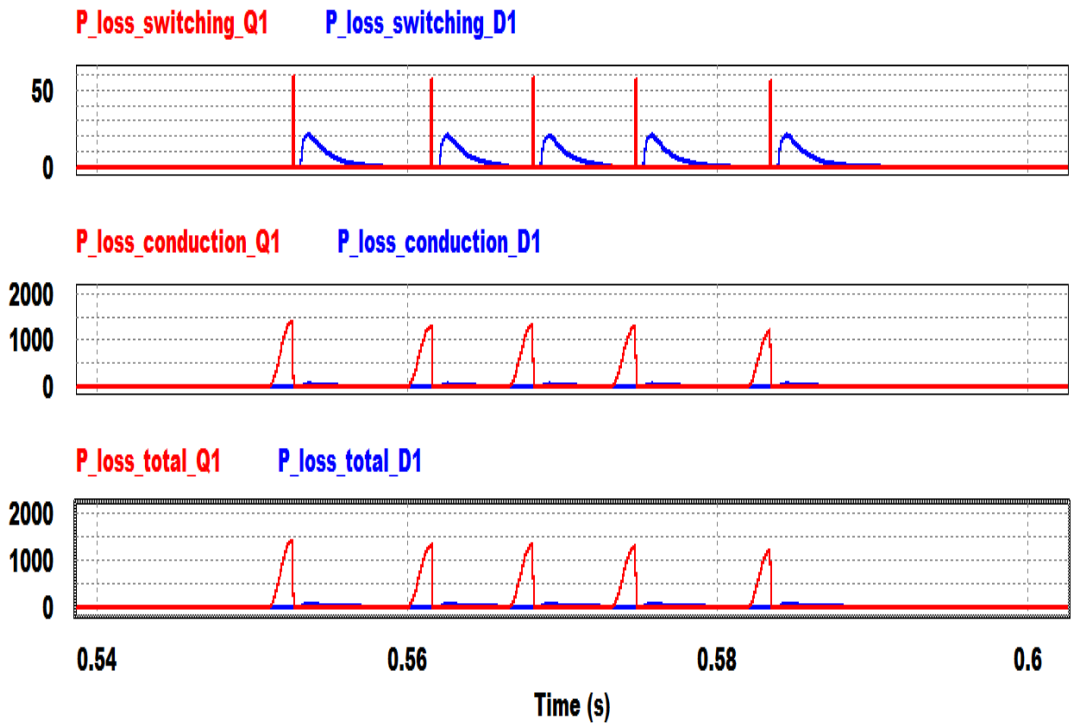

Fig. 4-34. DC bus side switch power loss division, switching, conduction and total, between the transistor Q1 and the body diode D1, for Pure Si MOSFET option

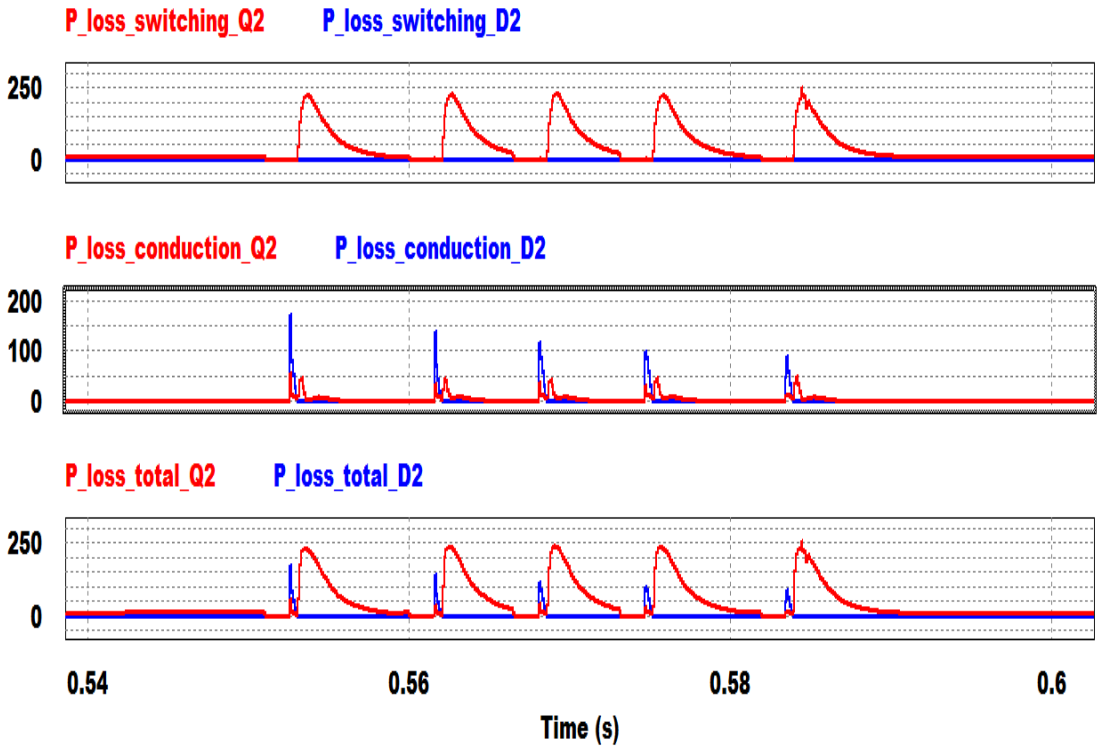

Fig. 4-35. Lower motoring switch power loss division, switching, conduction and total, between the transistor Q2 and the body diode D2, for Pure Si MOSFET option

4.3.3.7 GaN Cascode

Fig. 4-36 shows the battery current and voltage during regenerative braking for the GaN cascode option whereas Fig. 4-37 shows the battery SOC ramping up within the period after the regeneration pulses are initiated. Fig. 4-38 shows the relation between the voltages of the LV and HV sides of the DC/DC converter during the regeneration braking for this case. Fig. 4-39 and Fig. 4-40 show the vehicle torque and motor speed respectively during braking whereas Fig. 4-41 presents the phase voltages output of the motor drive's inverter for this option; GaN cascode. This figure show phase reversal and voltage pulsations during charging and discharging.

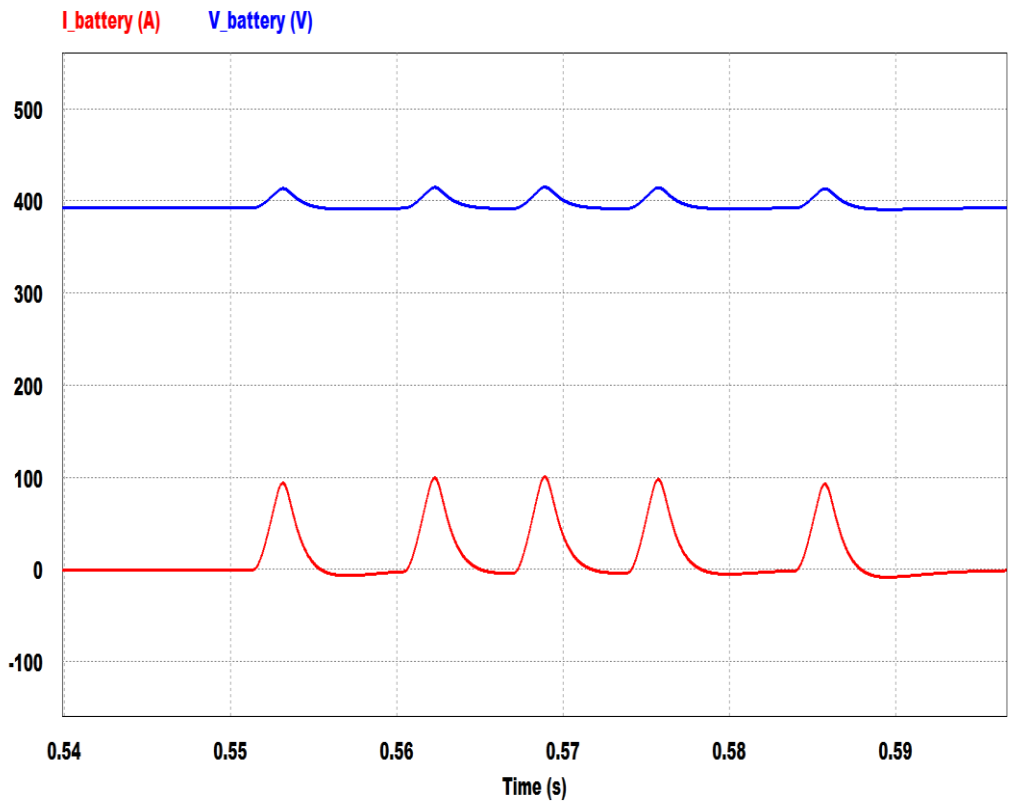

Fig. 4-36. Battery current and voltage during regenerative braking for GaN Cascode option

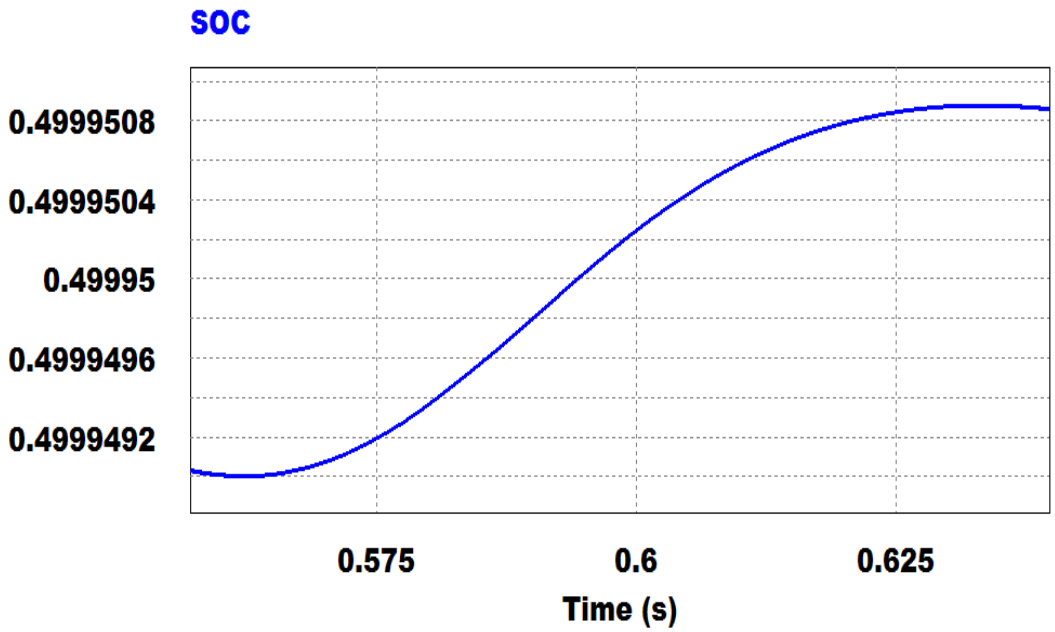

Fig. 4-37. Battery state of charge during regenerative braking for GaN cascode option

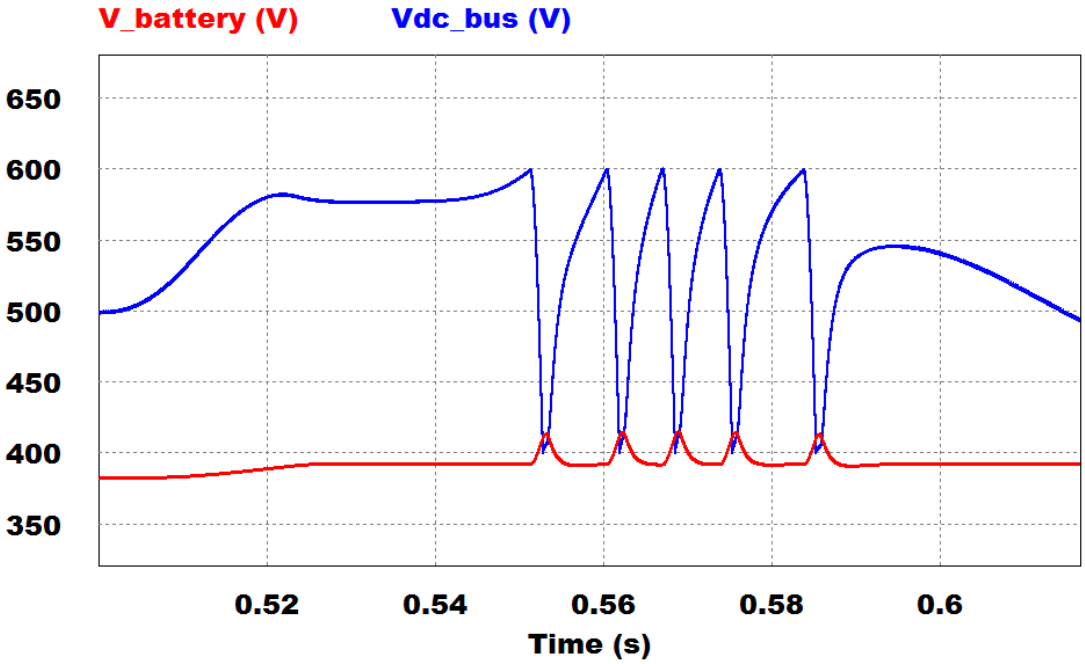

Fig. 4-38. Battery and DC bus voltages during regenerative braking for GaN cascode option

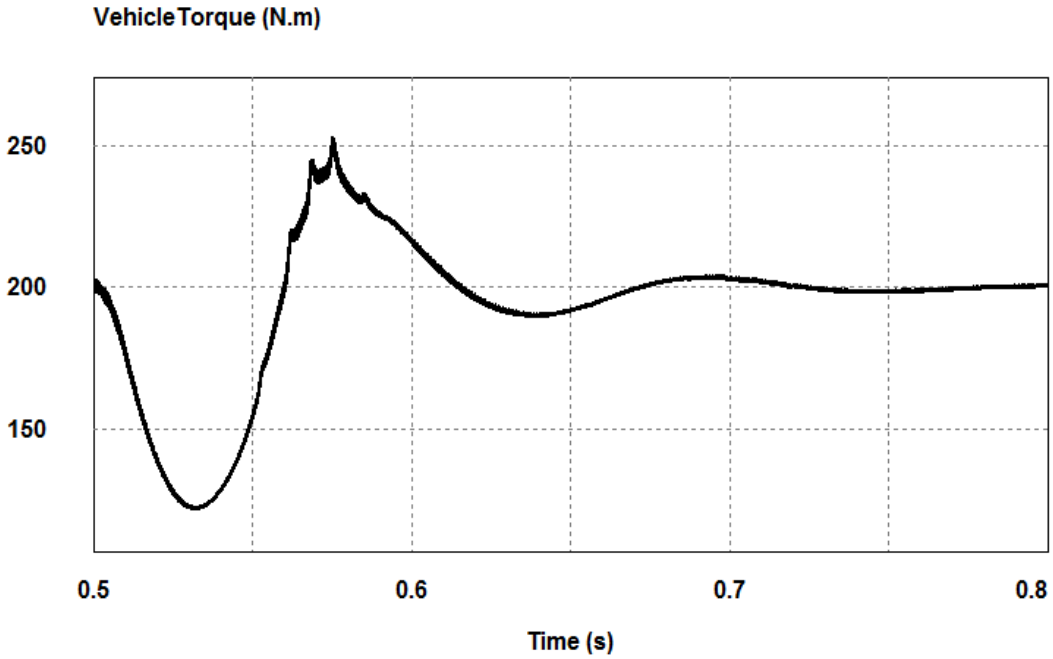

Fig. 4-39. Vehicle torque during braking for GaN cascode

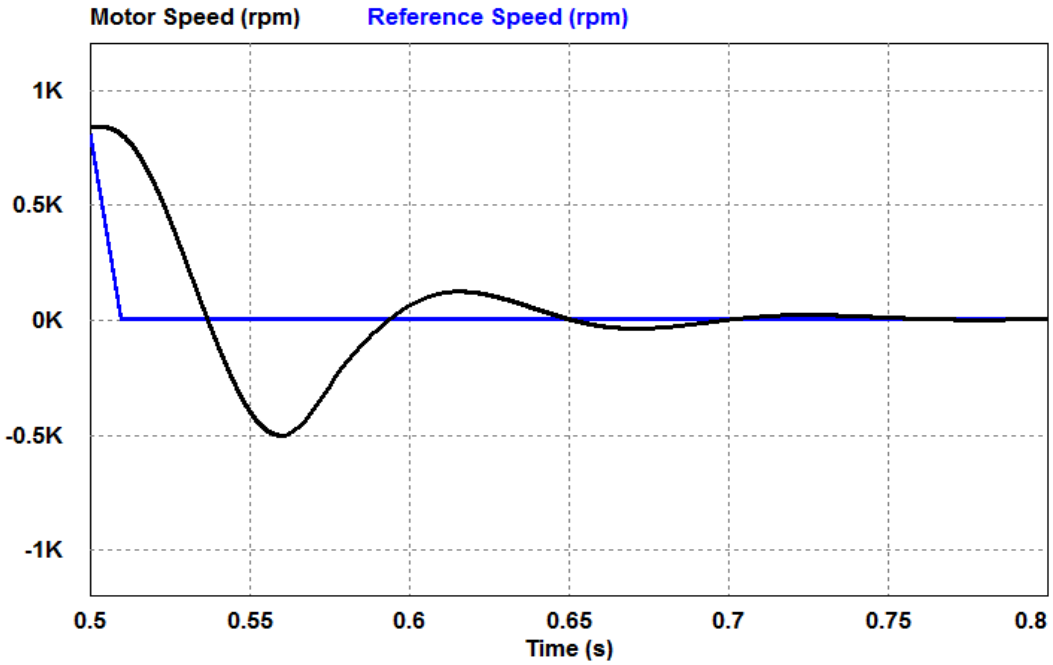

Fig. 4-40. Motor speed during braking for GaN cascode

Because of the charging and discharging actions during regenerative braking, the output voltage of the PMSM generator oscillates in a same manner as the DC bus voltage as shown in Fig. 4-41.

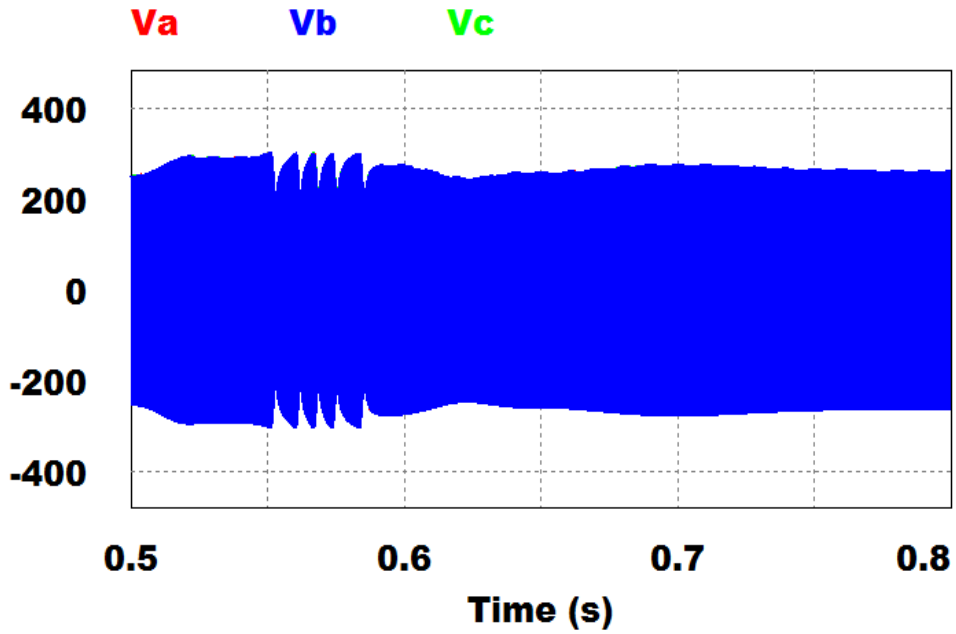

Fig. 4-41. Phase voltages output of the motor drive's inverter during braking for GaN cascode.

In Fig. 4-42, the motoring switch losses and the DC bus side switch losses pulses are presented for the GaN cascode option. The DC bus switch loss pulses reach a value from 1700 to 1950 W. The motoring switch losses consists of 2 pulses, an impulse from 450 W to 700 W followed by a wide pulse around 190 W. Fig. 4-43 and Fig. 4-44 present the GaN cascode switches loss division for the motoring switch and DC bus switch respectively. The DC bus switch loss pulses reach a value from 1650 to 1950 W for the transistor and 265 W for the diode, both primarily conduction. The loss pulses for the motoring transistor or diode are around 300 W but are wider for the transistor. The losses for each switch at the second steady state point is 4 W and 6 W for DC bus side and motoring switches respectively.

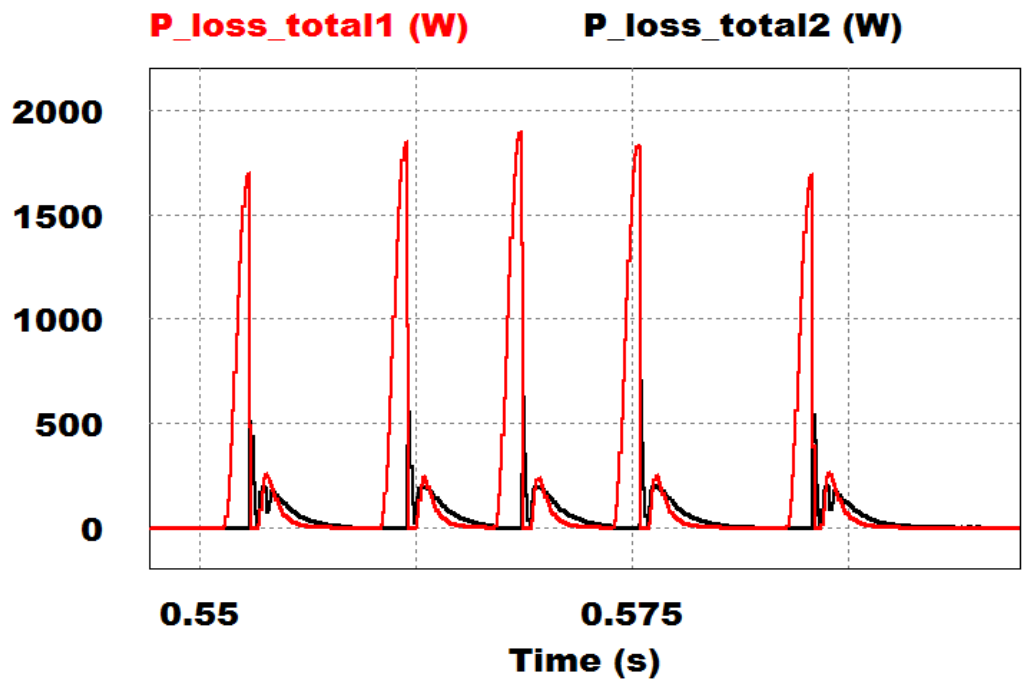

Fig. 4-42. Power losses during regenerative braking for the DC/DC converter switches for GaN cascode option; 1: DC bus side switch, 2: Lower motoring switch

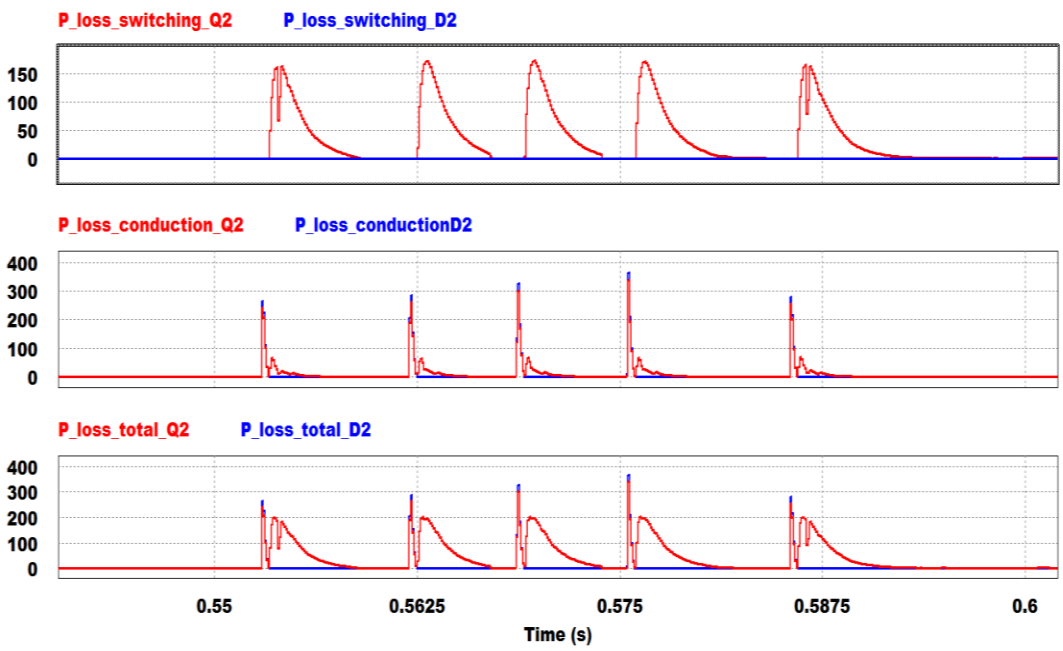

Fig. 4-43. Lower motoring switch power loss division, both switching and conduction, between the transistor Q2 and the body diode D2 for GaN Cascode option

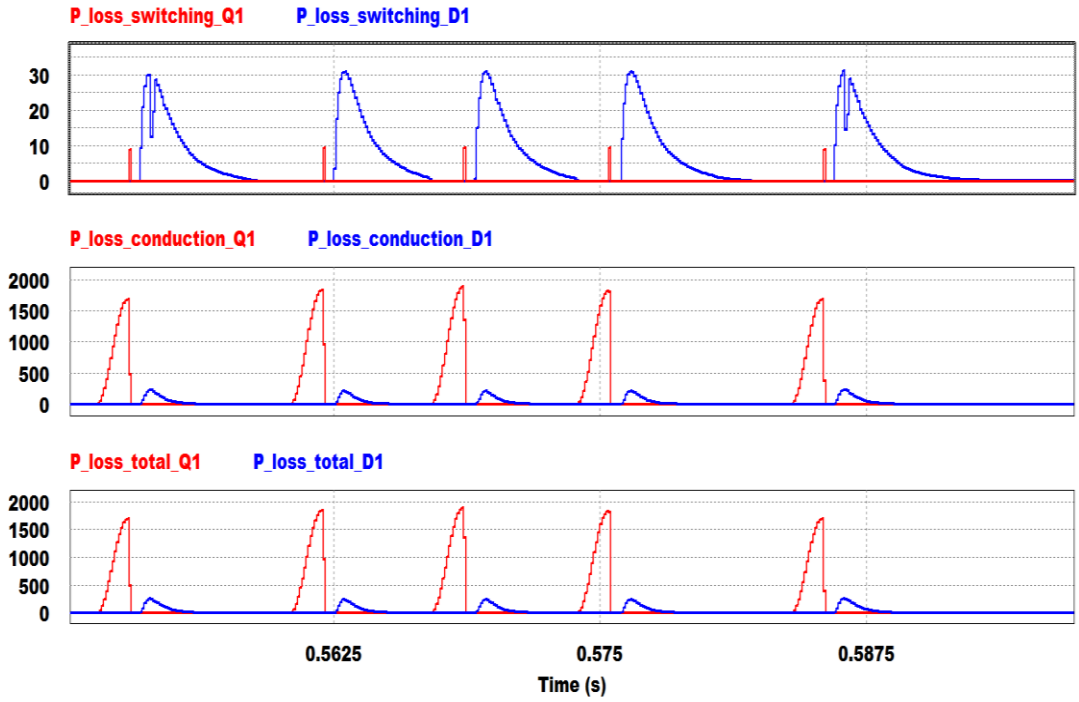

Fig. 4-44. DC bus side switch power loss division, both switching and conduction, between the transistor Q1 and the body diode D1 for GaN Cascode option

4.3.3.8 SiC ACCUFET

Fig. 4-45 shows the battery current and voltage during regenerative braking for the SiC ACCUFET option whereas Fig. 4-46 shows the battery SOC ramping up within the period after the regeneration pulses are initiated.

Fig. 4-47 shows the relation between the voltages of the LV and HV sides of the DC/DC converter. Fig. 4-48 and Fig. 4-49 show the vehicle torque and PMSM speed respectively during braking for this option; SiC ACCUFET.

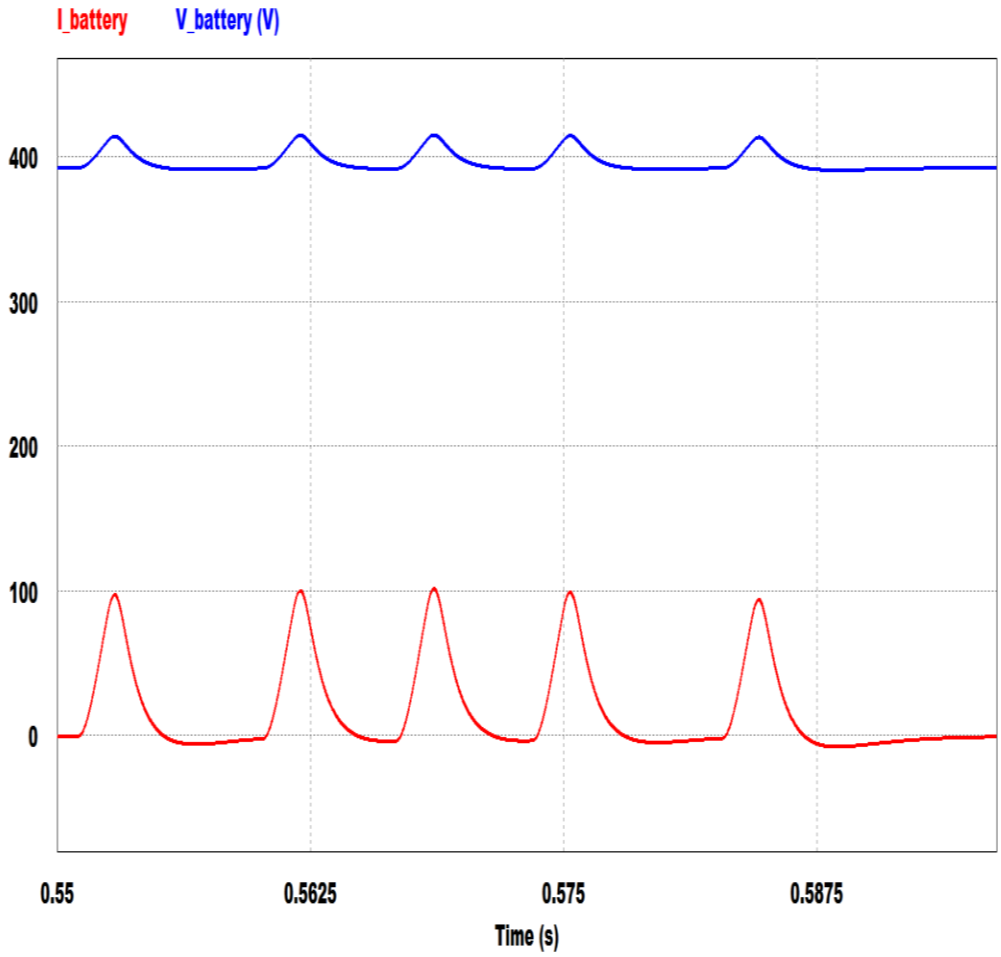

Fig. 4-45. Battery current and voltage during regenerative braking for SiC ACCUFET option

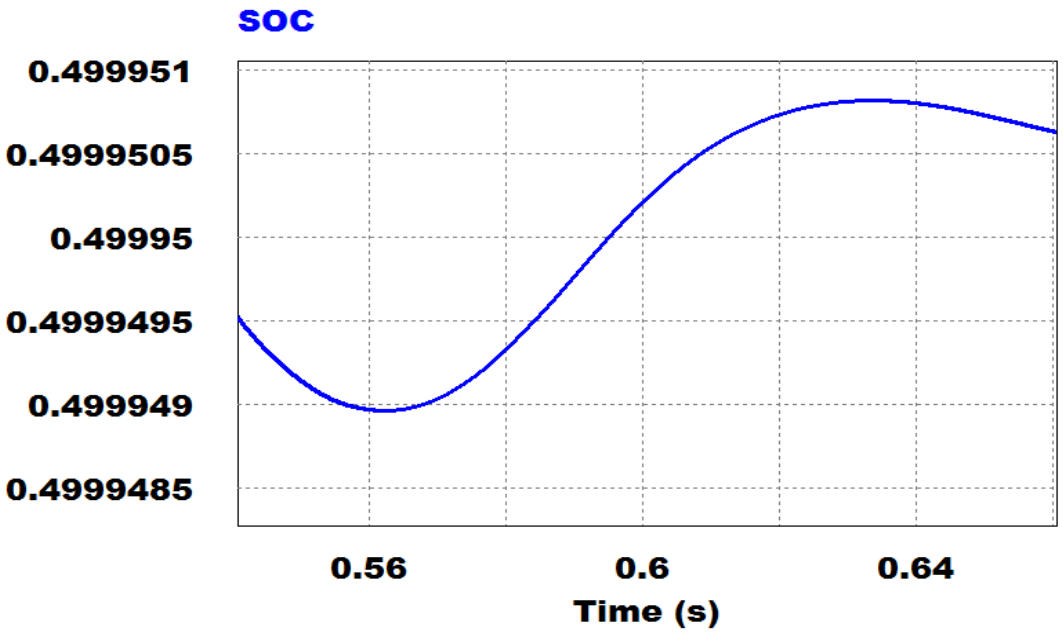

Fig. 4-46. Battery state of charge during regenerative braking for SiC ACCUFET option

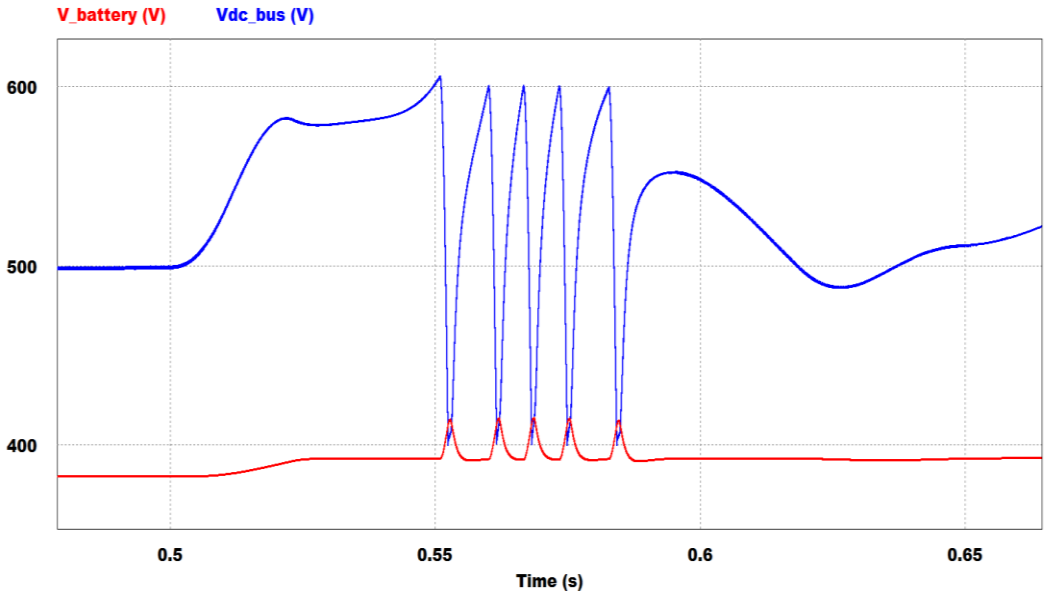

Fig. 4-47. Battery and DC bus voltages during regenerative braking for SiC ACCUFET option

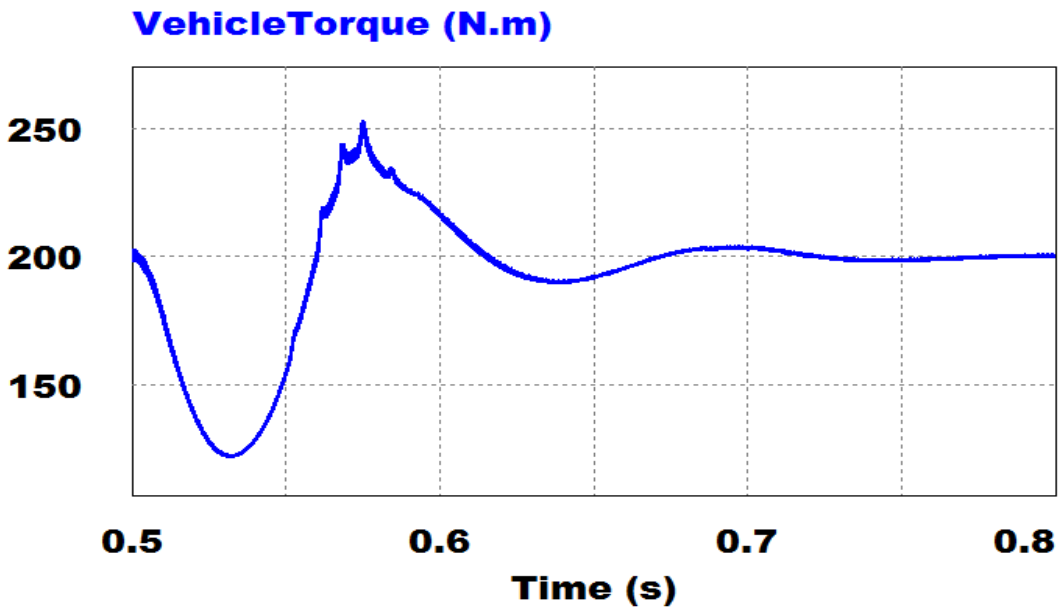

Fig. 4-48. Vehicle torque during braking for SiC ACCUFET option

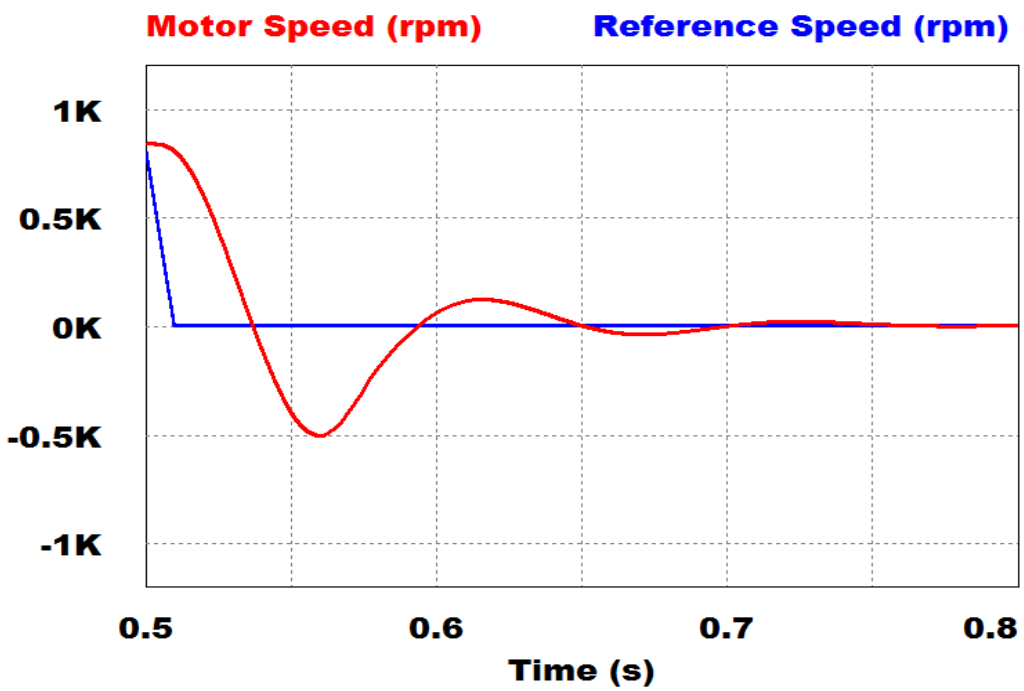

Fig. 4-49. Motor speed during braking for SiC ACCUFET option

Because of the charging and discharging actions during regenerative braking, the output voltage of the PMSM generator oscillates in a same manner as the DC bus voltage as shown in Fig. 4-50.

.

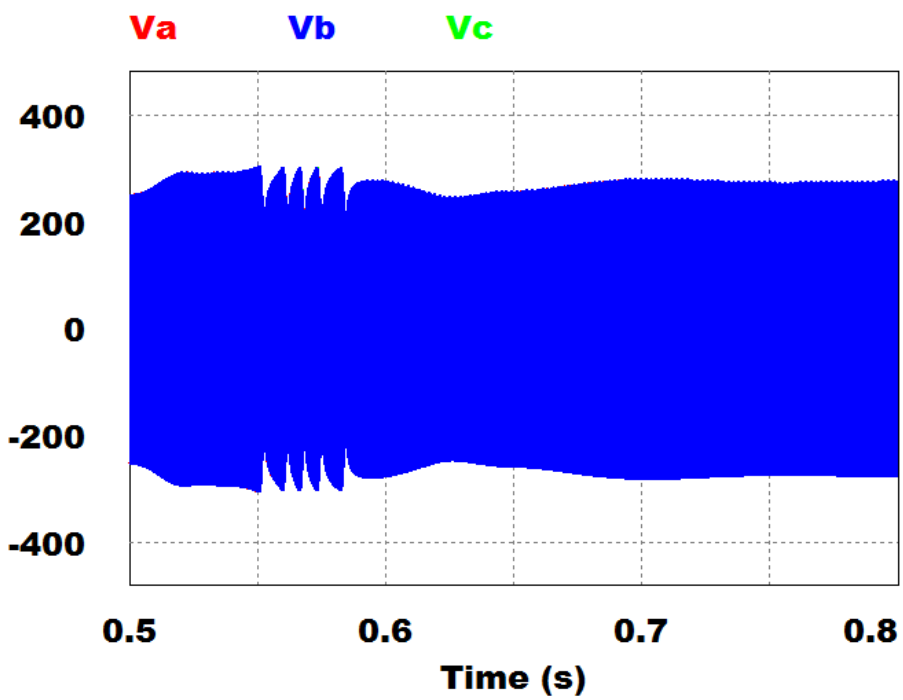

Fig. 4-50. Phase voltages output of the motor drive's inverter during braking for SiC ACCUFET option

In Fig. 4-51, the motoring switch losses and the DC bus side switch losses pulses are presented for the GaN cascode option. The DC bus switch loss pulses reach a value from 900 to 1000 W. The motoring switch losses consists of 2 pulses, an impulse followed by a wide pulse, both around 350 W.

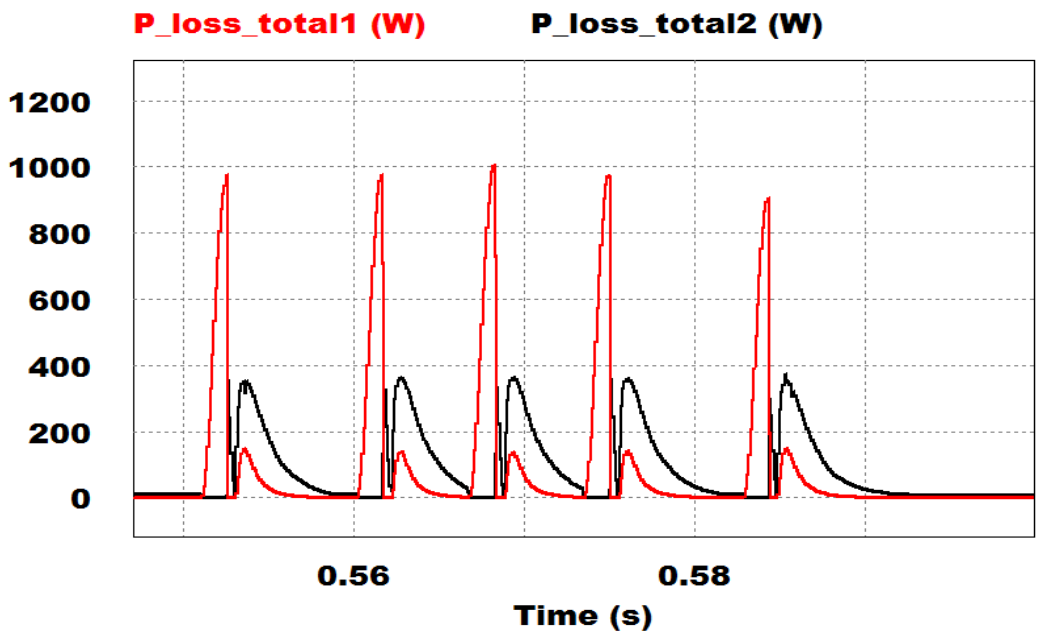

Fig. 4-51. Power losses during regenerative braking for the DC/DC converter switches for SiC ACCUFET option; 1: DC bus side switch, 2: Lower motoring switch

Fig. 4-52 and Fig. 4-53 present the division of the SiC ACCUFET switches loss values for the motoring switch and DC bus switch respectively. The DC bus switch loss pulses reach a value around 1000 W for the transistor and 180 W for the diode, both primarily conduction. The loss pulses for the motoring transistor are around 400 W and for the diode 200 W but are wider for the transistor.

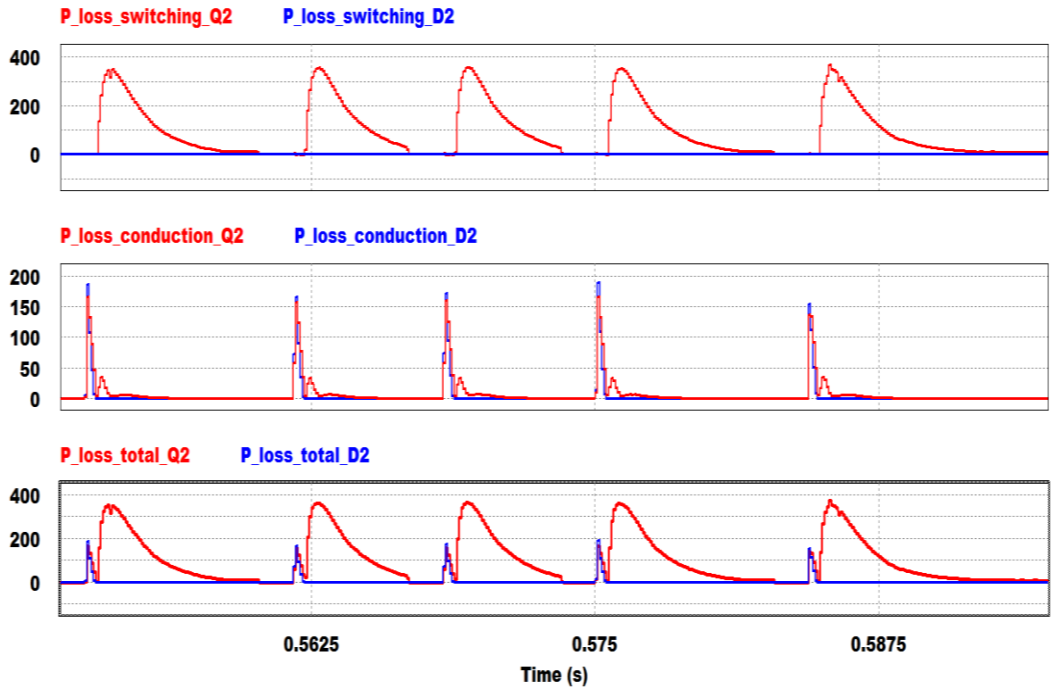

Fig. 4-52. Lower motoring switch power loss division, both switching and conduction, between the transistor Q2 and the body diode D2 for SiC ACCUFET option

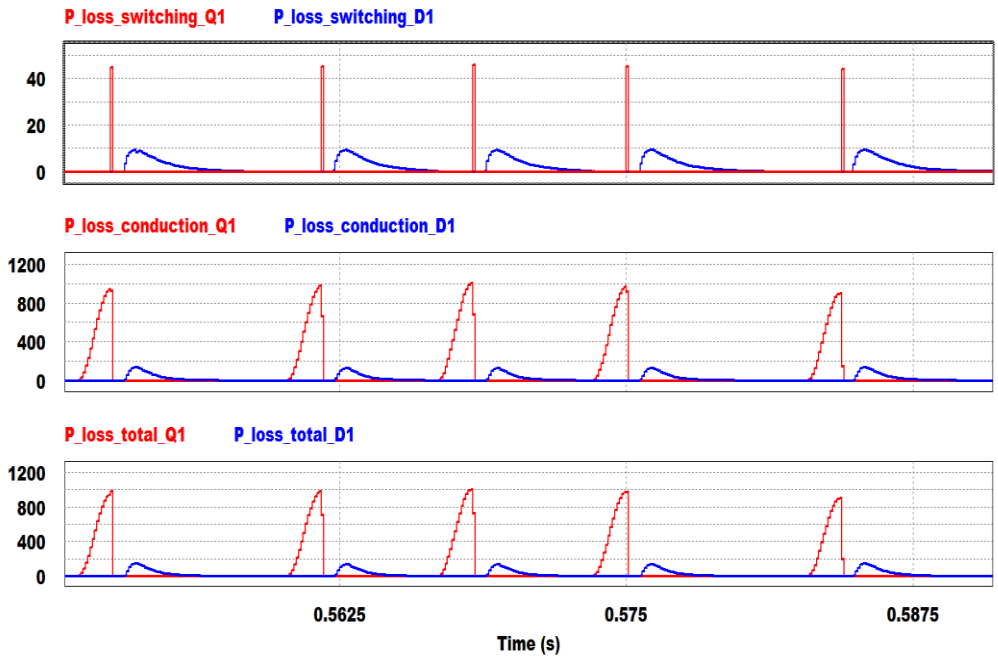

Fig. 4-53. DC bus side switch power loss division, both switching and conduction, between the transistor Q1 and the body diode D1 for SiC ACCUFET option

4.3.4 Conclusion

According to the NLEV simulation results, the following inferences can be concluded:

1. Switching the DC/DC converter at 50 kHz during motoring, the GaN cascode has a superior performance with high efficiency margin around the range of 0.6%-0.7% from the other options at all the tested temperatures. This means 60-67% smaller heat sink footprint and higher power density.
2. This superiority margin shrank to around 0.13% as the GaN cascode switching frequency increased to 300 kHz compared to the pure Si MOSFET option at only 50 kHz, yet with filtering components 83% size reduction and 9-10% heat sink size reduction. This means still higher power density than other options even switching other options at 1/6 frequency (50 kHz).
3. The efficiency margin between SiC and GaN switches is approximately constant around the range of 0.6%-0.7% at all cases for the tested normal load.
4. The SiC ACCUFET is comparable, in terms of efficiency, to the pure Si MOSFET only while switched at the same frequency of 50 kHz. At higher frequencies, it isn't.
5. The SiC ACCUFET is not a powerful candidate for high voltage medium power applications; e.g. NLEV. However, the SiC ACCUFET can work for higher voltage and higher power applications unlike pure Si MOSFET and GaN cascode. This gives the SiC ACCUFET an advantage in Railway systems. This is will be presented in the Railway application of the next chapter.
6. The higher junction temperatures affects primarily conduction losses while switching losses is affected directly by both switching frequencies and junction temperatures.

Chapter 5 : Advanced Rapid Transit Railway

5.1 Vancouver's Advanced Rapid Transit (ART) Description

The same problem and methodology for switching semiconductor options selection in the traction DC/DC converter has been applied to a railway system. For this purpose a 2-car Basic Train Unit (BTU) of ART 300 train, running in Vancouver BC Canada (Sky Train system), by Bombardier has been used. This is a regular Metro car in revenue service by Vancouver Sky Train and manufactured by Bombardier. Both cars are LIM powered vehicles running on 750 VDC from the 4th rail. A Traction converter (TC) - inverter system to convert 750 V DC into 3-phase regulated AC for LIM is already on board.

The PSIM model developed for NLEV is used to simulate the ART, with different components' ratings and parameters. Each BTU contains 2 cars. Each car have 2 motors, each of 130 kW. The empty weight of the car is 20.5 tons, full load is 25.5 tons corresponding to 5 kg.m.m rotational mass. Speaking of each LIM Thrust-Speed profile, it is a constant continuous thrust of 13,200 N until the knee speed of 54 km/h and after that it is a constant power until 90 km/h.

Compared to the passenger road vehicle load, this railway load is heavier in weight requiring more thrust to drive the system while the speed range is lower than the passenger road vehicle load. This requires different component ratings and accordingly, different control parameters. Moreover, the railway using LIM doesn't feature gear systems. As a result, each LIM equivalent PMSM can have a small field weakening range as seen in the motor specifications.

The ART system is tested, in this study, at a regular speed of 27 km/hr and the maximum continuous thrust assuming a wheel diameter of 575 mm for a rail under service.

(27 km/hr * 11.28 revolutions. hr / km. min = 300 rpm= 31.4 rad/sec)

5.2 Advanced Rapid Transit (ART) Design and Simulation

5.2.1 Traction Motor

5.2.1.1 Motor Parameters Estimation by Trial and Error

The ART parameters entered to the PSIM model for the traction motor are listed in Table 5-1.

Table 5-1. The Traction motor parameters for ART

Number of Poles	8
Line-to-line back EMF constant	122 V/krpm
Stator winding resistance	0.000065 ohm
d-axis inductance at rated conditions	0.000479 H
q-axis inductance at rated conditions	0.02 H
moment of inertia	0.25 kg.m2
Shaft time constant	100 sec
Maximum motor torque	5 K N.m
Maximum motor power	400 kW
Maximum motor speed	5000 rpm

5.2.1.2 3-phase inverter control

The parameters of the motor's inverter control circuit for ART is the same as those for NLEV except the maximum inverter output current amplitude, it's higher as seen in Table 5-2.

Table 5-2. The parameters of the motor's inverter control circuit for ART

Inverter switching frequency	20 kHz
PWM carrier peak amplitude	1
Inner current loop sampling frequency	20 kHz
Outer speed loop sampling frequency	5 kHz
Maximum inverter output current amplitude	2000 A

5.2.1.2.1 Speed and MTPA

The PI controller constants of motor control with other dependent parameters for the ART load, obtained using trial and error, are listed in Table 5-3.

Table 5-3. Dependent parameters of motor control for ART

Motor	K_TA_m	1.80579
	Te_max_m	127188
Inverter	Vsmax_m	390
d-axis control loop	K_d_m	1.80579
	T_d_m	0.117908
q-axis control loop	K_q_m	5
	T_q_m	0.0769231
Speed control loop	K_w_m	0.326313
	T_w_m	0.00276239

5.2.2 DC bus

The parameters characterizing the DC bus are listed in Table 4-7. The DC link voltage is according to the IEEE standards in

Table 5-4. DC bus parameters for the ART

Nominal DC Bus Voltage	900 V
Minimum DC Bus Voltage	600 V
Maximum DC Bus Voltage	1200 V
DC bus capacitance	0.0375 F

5.2.3 DC/DC Converter

The specifications of the DC/DC converter used for ART simulation are listed in Table 5-5.

Table 5-5. The parameters of the DC/DC Converter for ART

Maximum battery charging power		200 kW
Maximum battery discharging power		400 kW
Converter switching frequency	fsw	50- 100 kHz *
Low-Voltage Side Inductance	L_LV	0.0001 H
Low-Voltage Side Capacitance	C_LV	0.0375 F
Carrier peak amplitude	V_ramp	1

*depends on the thermal limits of the switching semiconductor options used

5.2.3.1 Inductor Selection

For ART: For f > 50 kHz (minimum switching frequency in this study)

and 5% current ripple limit:

L_LV> 0.030146/ I batt = 20.047/ load power = 0.000083 H

For f > 50 kHz, and a value of L_LV= 0.0001 H, The current ripple will be limited to

$$\Delta I_L = = (1\text{-}665/900)* 665/ (0.0001*50000) = 15.072 \text{ A}$$

This ripple value is 4.175 % of rated inductor average current of 361 for 120 kWh battery pack. This percentage will rise at low loads but will still be lower than the 5%. However, the same inductance value will result in less ripple for higher frequencies which is in favor to the high frequency switching WBG devices; SiC ACCUFET for the case of ART.

According to the above analysis, a value of L_LV = 0.1 mH is selected for the ART DC/DC converter as seen in Table 5-5, which is 8 times less than that of NLEV case.

5.2.3.2 DC/DC Converter Control

The required DC/DC converter parameters, associated symbols and values obtained for ART using trial and error are as seen in Table 5-6. The parameters of the motor's inverter control circuit for ART is the same as those for NLEV.

Table 5-6. DC/DC converter parameters, associated symbols and values

Loop	Parameters	Symbol	value
Current loop	PI gain	K_ca_up	0.01
	PI time constant	T_ca_up	0.002
voltage loop	PI gain	Kv_up	0.144513
	PI time constant	Tv_up	0.00397888
Regen mode control	regen power limit	P_regen	632.5

5.2.3.3 Switch selection

Based on the required load, each switch of the two needed for the DC/DC converter requires ratings as listed in Table 5-7. The key characteristics comparison between the available switch options for ART at 25 ºC case temperature are listed in Table 5-8.

Table 5-7. DC/DC converter's switch requirements for ART

Rating	Minimum for ART
DC Voltage	900 V
DC current	361 A (120 kWh)

Table 5-8. Key comparison characteristics@ 25 ºC case temperature for ART options

Device type	$R_{DS\ on}$(mΩ)	V_{DS}, V_{CE} (V)	DC I_{rated} (A)	dV/dt V/ns
[31] SiC ACCUFET	5.7	1200	444	50
[77] Hybrid Switch	$V_{CE(sat)}$ @ 450A=2.4V	1200	450	50

5.2.3.4 Thermal frequency limit

The temperature rise of the junction over the module case should be limited to 125 ºC assuming the heat sink is successful to maintain 25 ºC case temperature. Consequently, this limits the allowed power dissipation (Pdm) of the used transistors and diodes to the values listed below. The maximum allowed power dissipation for each switch option is calculated based on the thermal resistance from the datasheet. Those for ART are listed in Table 5-9. This dissipation limit decides the maximum switching frequency for each switch option. Accordingly, the SiC ACCUFET switching frequency is selected to be 100 kHz. For the Hybrid module, it's 50 kHz. For the purpose of comparison, the ACCUFET transistor option were tested also at 50 kHz.

Pdm (W) = Max. allowed temperature rise (ºC) / Thermal Resistance (j-c) (ºC/W)

Table 5-9. Maximum allowed power dissipation for ART options

	Thermal Resistance (j-c) (ºC/W)	Pdm (W)
SiC ACCUFET Transistor	0.07	1785
SiC ACCUFET Diode	0.07	1785
Hybrid module Transistor	0.092	1358
Hybrid module Diode	0.15	833

5.2.4 Li-Ion Battery

Table 5-10 show some specifications of the intelligent battery module cell from Kokam. Kokam battery pack consists of 4 modules. The specifications of Li-ion battery pack used in PSIM to simulate the 750 V 240 kWh Kokam battery used for the ART car is shown in Table 5-11. Cell count calculations based on the Saft VL-34570 rechargeable lithium-ion battery cell is as follow:

Number of cells in series (Ns) = 750 V/3.7 V/cell = 208 cells
Number of cells in parallel (Np) = 280 Ah/ 5.58 Ah= 50 cells

Table 5-10. Kokam's battery module specifications for ART [78]

Energy	kWh	30
Weight of battery	Kg	360
Energy density	Wh/kg •Wh/l	82 • 133
Discharge power cont. /max.	kW	92 / 370
Charge power cont. /max.	kW	92 / 153
Dimensions	mm^3	750x216x1545

Table 5-11. Li-ion battery pack PSIM specifications for ART

Number of cells in series	208
Number of cells in parallel	50
Rated cell voltage	3.7 V
Full cell voltage	4.2 V
Discharge cut-off cell voltage	2.7 V
Rated cell capacity	5.4 Ah
Internal cell resistance	0.05 ohm
Maximum cell capacity	5.58 Ah
Exp. point cell voltage	3.9 V
Exp. point cell capacity	1.08 Ah
Maximum continuous current	11 A

5.3 ART Simulation Results

5.3.1 The General Performance

Testing the system against the driving cycle, the main waveforms through the powertrain system were as seen in the following graphs. No significant differences between different options were observed in terms of DC bus voltage, battery voltage, torque, and speed profiles. Just a slight change in battery current occurred that reflected the difference in the switch properties. Fig. 5-1 shows the battery current during the driving cycle. As seen, the current tends to reach steady state value around 233 A after 0.7 second. After that, the braking command to 1% of the speed starts; so, the battery current ramped up to zero then oscillates between negative and positive till the new steady state point which is around zero. The value of this regeneration energy differs with the switches' parameters within the conversion system. The regeneration energy for each switch option is listed in the regeneration section. All the waveforms have under damped transient performance as shown in the following figures, which is a desired behaviour.

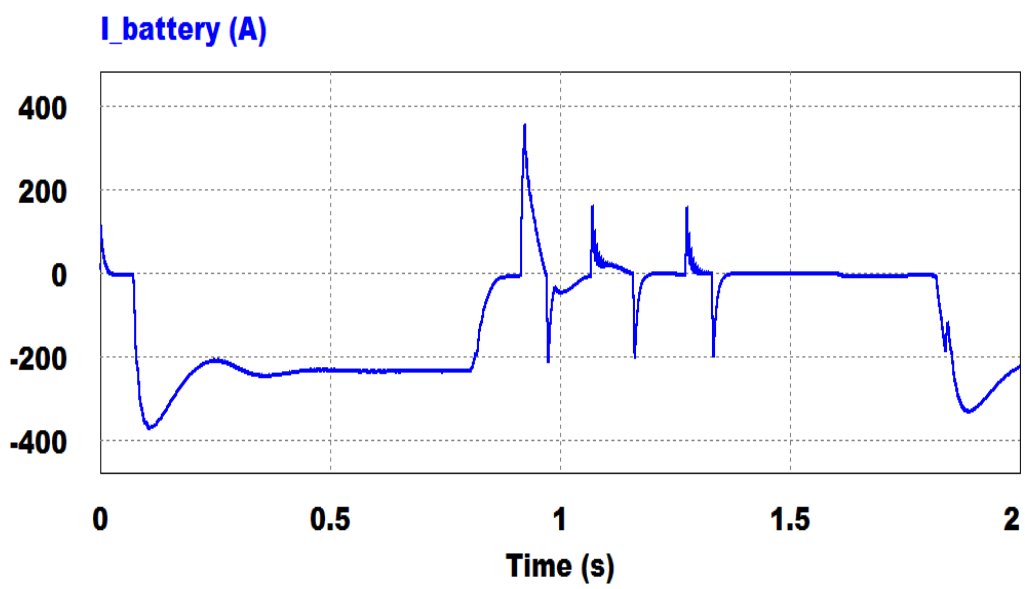

Fig. 5-1. Battery current for the ART

In Fig. 5-2, the battery terminal voltage decreases to 670 V with loading. As the battery current decreases with braking, the battery terminal voltage rises again to around 720 V. During the regenerative current pulses, the battery voltage pulsates up near to 781 V until

after 3 pulsations it settles around 720 V. During this regeneration period, the DC link voltage pulsates between 700 V and 1000 V in opposite to the battery voltage pulsations as observed in the waveforms till it settle at 900 V. During motoring, the steady state average value of the DC link voltage is around 900 V. Fig. 5-3 shows the battery state of charge with rise during braking.

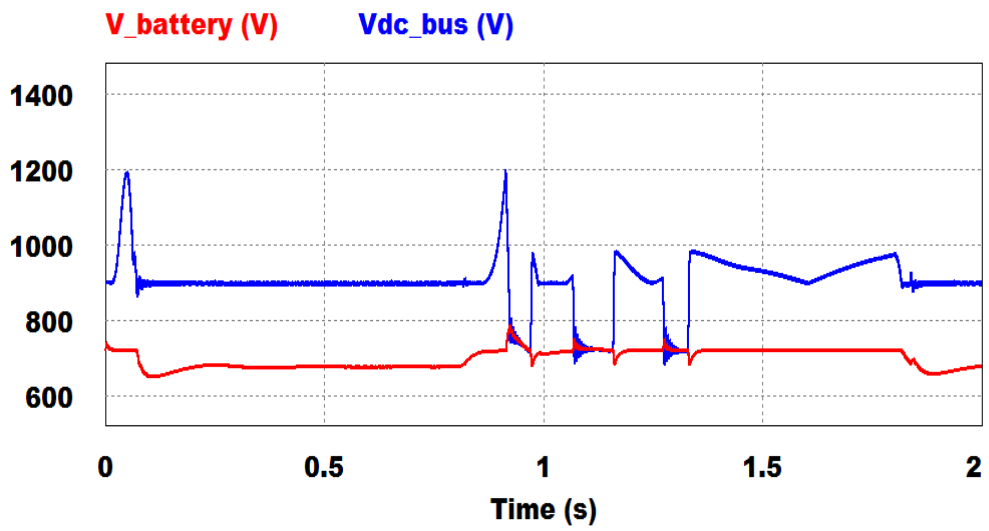

Fig. 5-2. Battery voltage and DC bus voltage for the ART

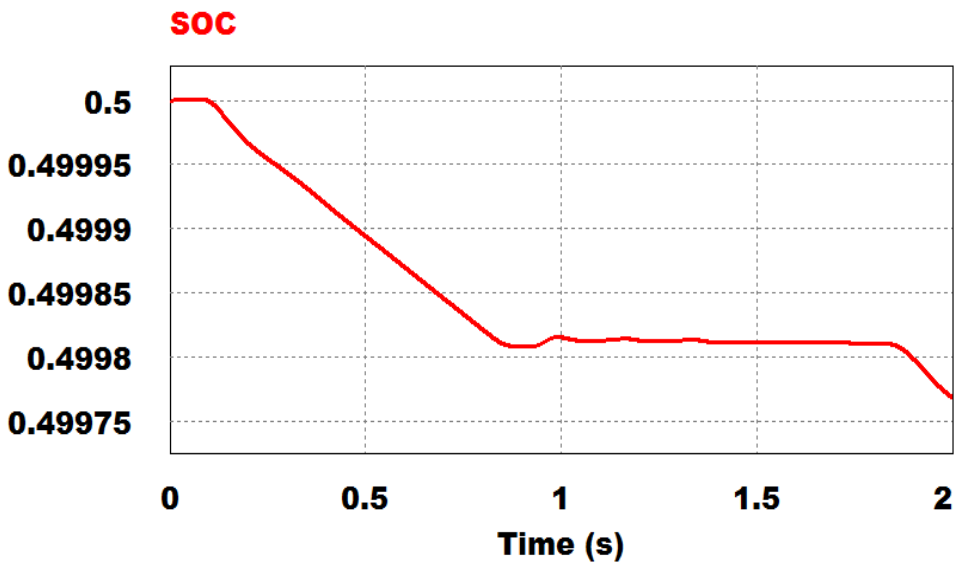

Fig. 5-3. Battery state of charge during the whole driving cycle for the ART

Regarding the motor output, the vehicle torque is as shown in Fig. 5-5. Motor speed tracking the reference speed that is higher than the motor threshold speed. As seen, the torque have under damped behavior during both motoring and braking. The torque ripple at the first steady state point is 100 N.m (2%). Also the steady state for first motoring step was reached around 0.5 second which is fast enough for the metro system. After the braking command started, the vehicle torque decrease to 1.5 k N.m to decrease the speed and then rose again in an under damped behaviour to reach the second motor torque steady state, which is the same as the first as this is a constant load torque, after 1 second from the braking command start. Following this braking, the motor torque increased to increase the speed again to the third steady state value while the torque settle again at 5 k N.m.

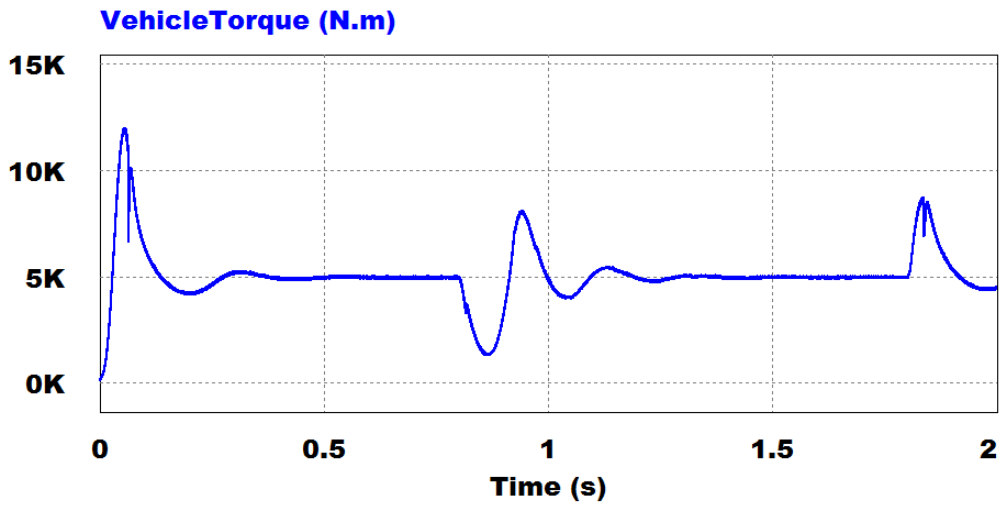

Fig. 5-4. Vehicle Torque during the whole driving cycle

Fig. 5-5 presents the motor speed trend during motoring and braking. The speed waveform successfully traced its reference during motoring, then braking, and finally motoring again. As observed, the reference speed is higher than the motor threshold speed. This means that the motor work in the field weakening region. The response of the speed control of the PMSM is very fast as observed and could reach steady state in 0.8 seconds for motoring to regular speed of 27 km/hr and 0.6 seconds for braking from 100% of regular speed to 1%. The negative speed during braking represents the motor working as a generator to charge the battery; i.e. regenerative braking. Fig. 5-6 presents the lower motoring switch current whereas Fig. 5-7 shows the voltage across this switch terminals.

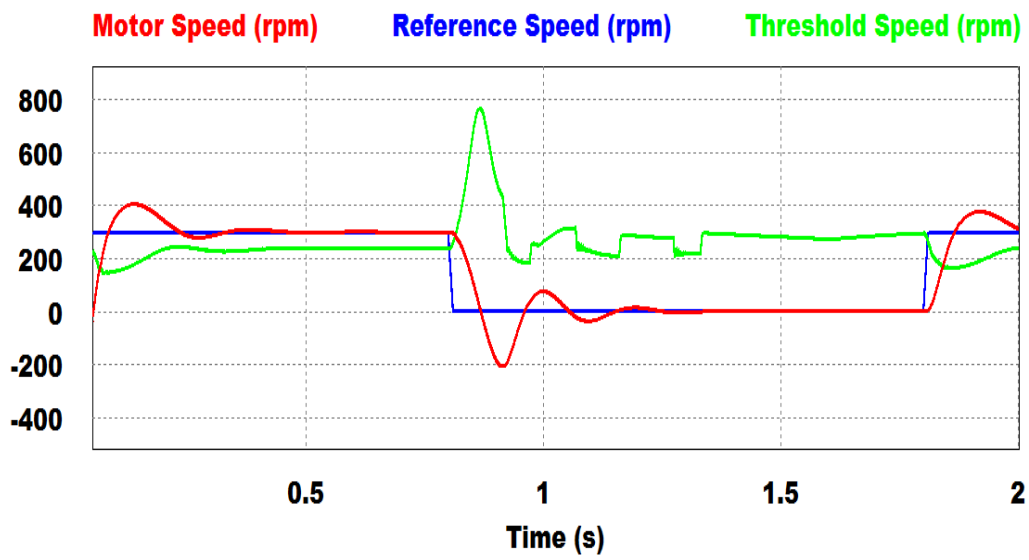

Fig. 5-5. Motor speed tracking the reference speed that is higher than the motor threshold speed

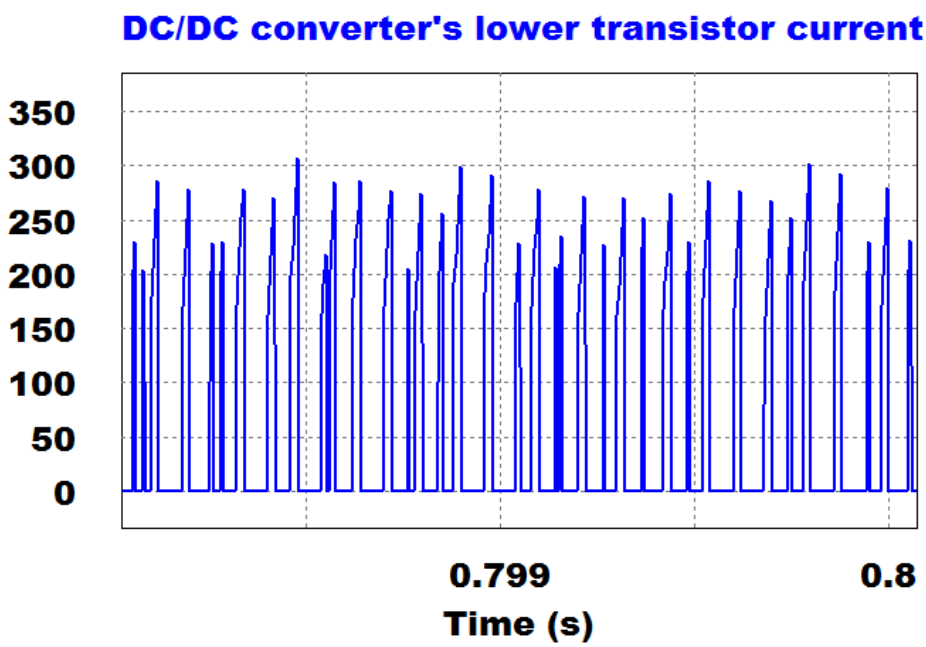

Fig. 5-6. The DC/DC converter Lower motoring switch current during steady state motoring

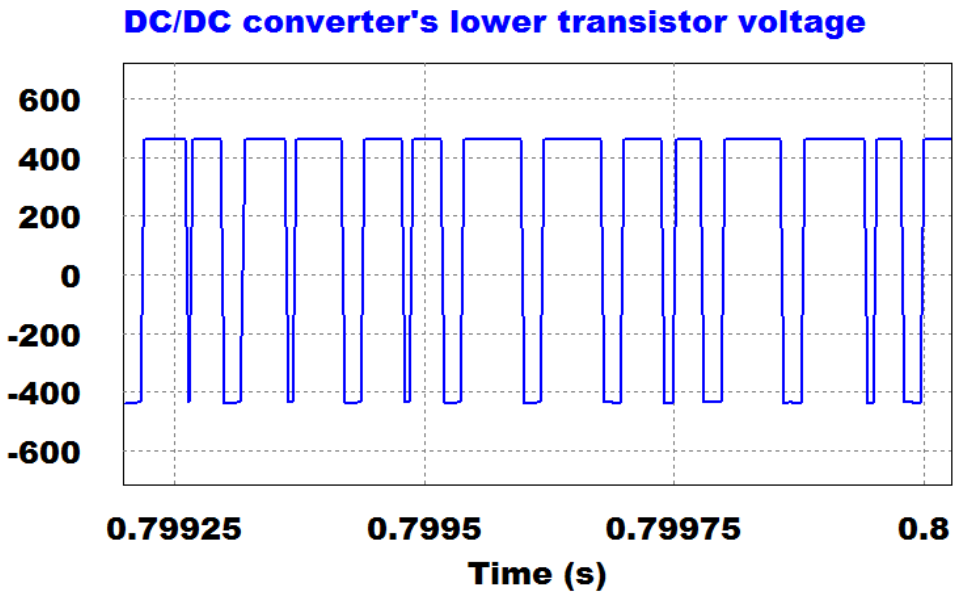

Fig. 5-7. The DC/DC converter Lower motoring switch voltage during steady state motoring

Fig. 5-8 presents the motor input 3 phase currents out of the inverter. The currents are sinusoidal with peak of 320 A at steady state motoring. The 3- phase voltages output of the inverter are shown in Fig. 5-9. These voltages are pulse width modulated. The modulation and carrier signals producing the PWM signals inputs to the inverter are captured in Fig. 5-9. The modulation signal amplitude is determined by the current control according to the reference speed and the operating conditions as illustrated in the chapter 3.

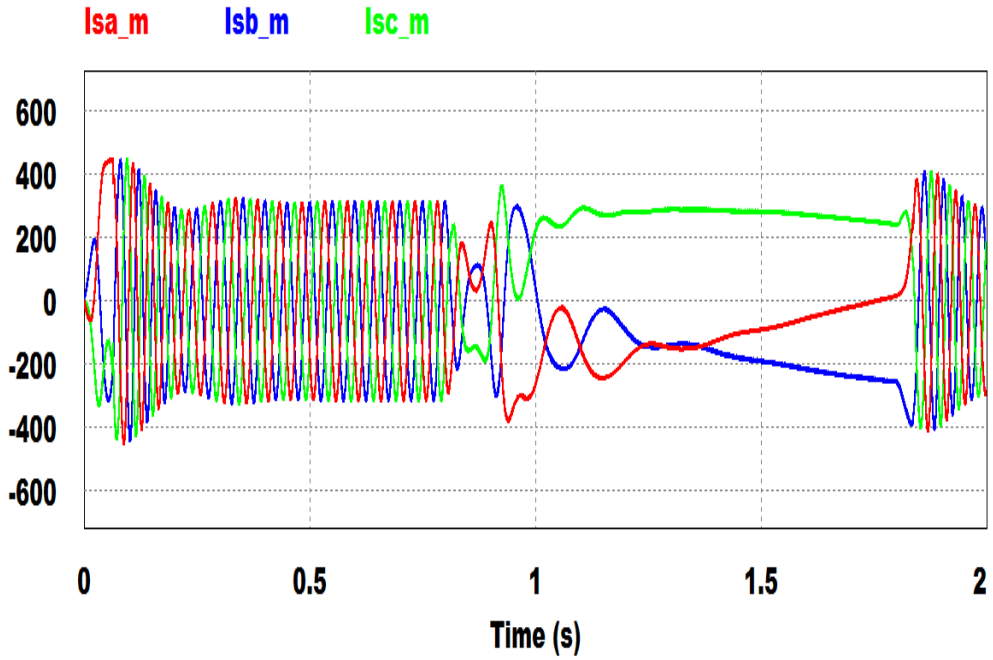

Fig. 5-8. The motor input 3- phase currents out of the inverter during the whole driving cycle

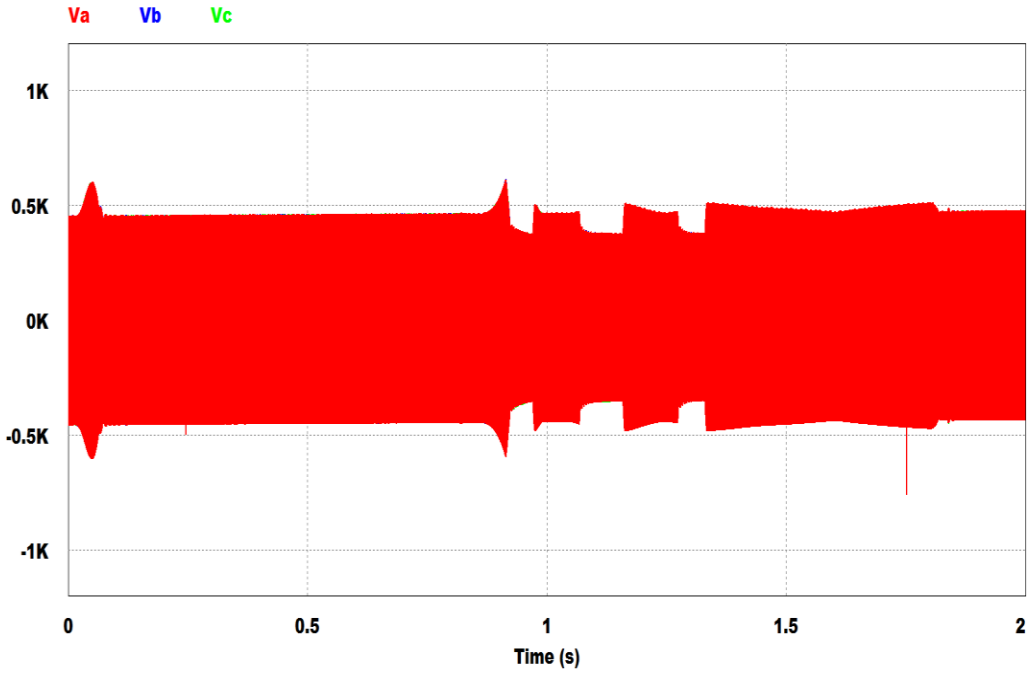

Fig. 5-9. The motor input 3- phase voltages out of the inverter

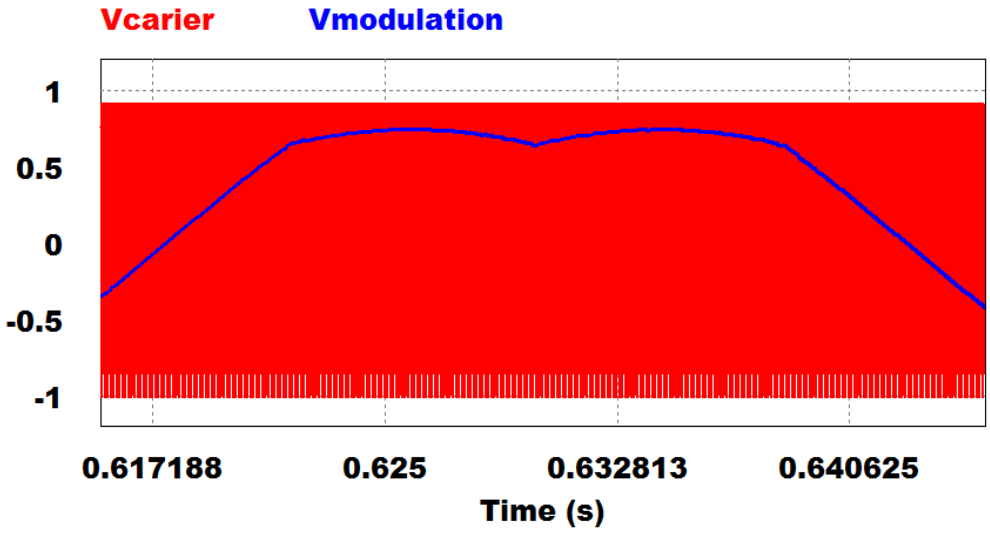

Fig. 5-10. The modulation and carrier signals producing the PWM signals inputs to the inverter during steady state motoring

5.3.2 Motoring Steady state Performance

As mentioned in the general performance section, no significant differences between proposed options were observed in terms of DC bus and battery voltages, torque and speed profiles. Just a slight change in battery current that reflects the difference in the switch properties. Table 5-12 lists the motoring steady state battery current at 25 ºC for available choices.

Table 5-12. Switch peak current comparison at 25 ºC for ART

SiC ACCUFET at 100 kHz	232.94 A
SiC ACCUFET at 50 kHz	232.997 A
Hybrid Switch at 50 kHz	233.07 A

5.3.3 Loss and Efficiency Comparison during Motoring

5.3.3.1 Lower Motoring Switch

In Fig. 5-11, a chart compares the losses, switching, conduction and total, for the proposed options in the lower motoring position where the transistor only operates during motoring. As seen, the SiC ACCUFET has a superior performance compared to the Hybrid switch. Table 5-13 lists the values of these losses. As seen, the SiC transistor switched at 50 kHz, like the Hybrid Module, posses 31% only of the loss for Hybrid. Switching the SiC at 100 kHz, it's loss increase by more 80% to reach 57 % only of the loss for Hybrid.

Table 5-13. Lower motoring switch power loss at 25 ºC junction

SiC ACCUFET at 100 kHz	433.22 W
SiC ACCUFET at 50 kHz	239.50 W
Hybrid Switch at 50 kHz	772.28 W

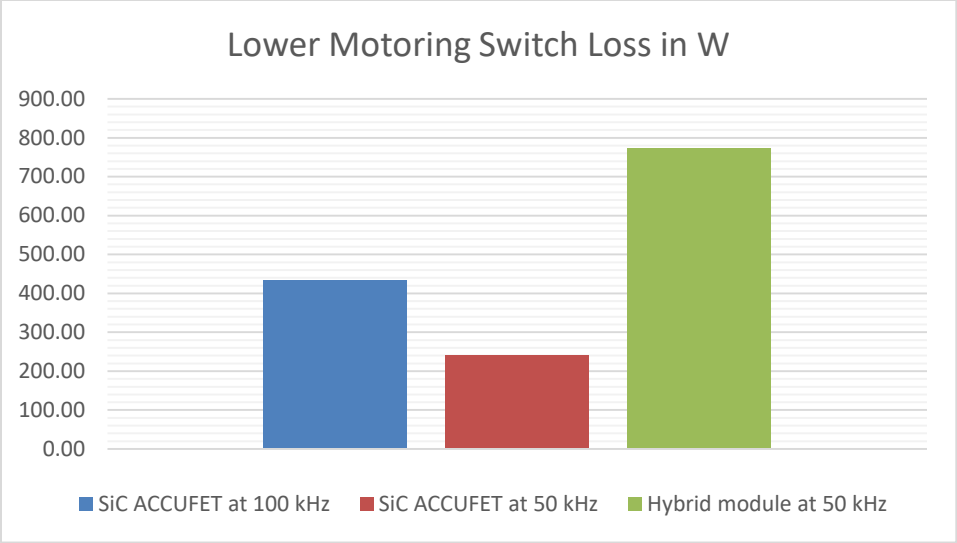

Fig. 5-11. Lower motoring switch power loss at 25 ºC junction

5.3.3.2 DC bus side Switch

In Fig. 5-12, a chart compares the losses, switching, conduction and total, for the proposed options for the DC bus side position where the diode only operates during motoring. As seen, the SiC diode switched at 50 kHz, like the Hybrid Module, posses 87% of the loss for Hybrid. Switching the SiC at 100 kHz, its loss increase by more 11.5% to reach 84 % of the loss for Hybrid. Nevertheless, the two diodes are SiC SBD so the losses difference is very small due to the difference in ratings available from different manufacturers. Table 5-14 lists the values of these losses used in the comparison. It should be noted that the 2 DC/DC converter switches should be similar for easy gate control and synchronization during both motoring and braking. The ART results conforms to this rule.

Table 5-14. DC bus side switch power loss at 25 ºC junction

SiC ACCUFET at 100 kHz	226.96 W
SiC ACCUFET at 50 kHz	234.80 W
Hybrid Switch at 50 kHz	270.00 W

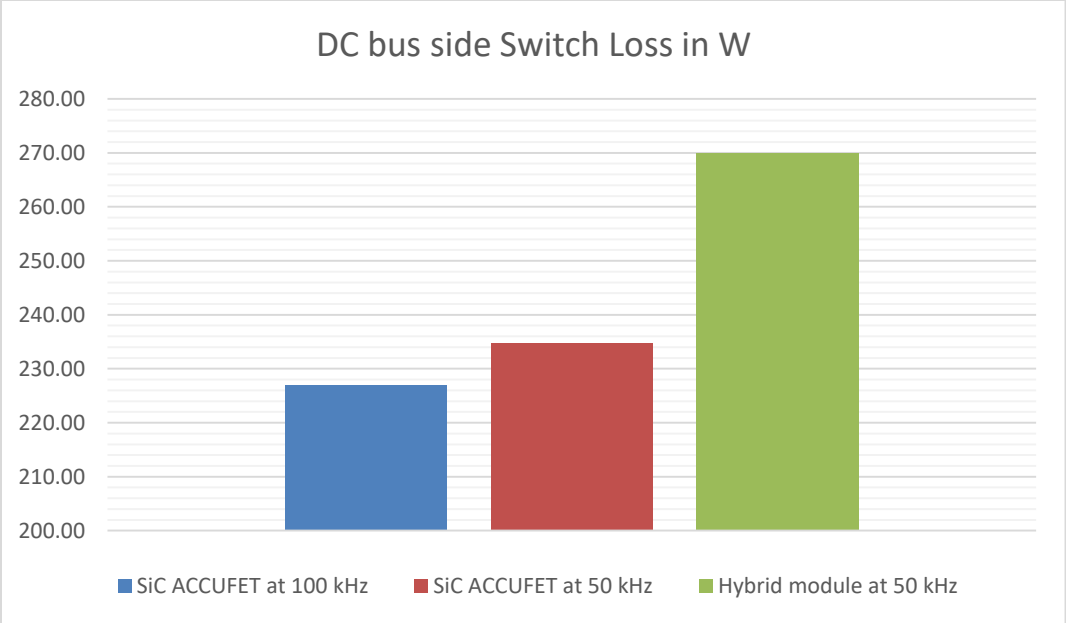

Fig. 5-12. DC bus side switch power loss at 25 ºC junction

5.3.3.3 Total Converter efficiency

As a result of the results listed above, the total converter losses are less for the SiC ACCUFET as seen in Table 5-15.

Table 5-15. DC/DC converter switches total losses and efficiency for the ART

	SiC ACCUFET at 100 kHz	SiC ACCUFET at 50 kHz	Hybrid module at 50 kHz
Losses (W)	660.18	474.30	1042.28
Efficiency (%)	99.58	99.70	99.34
Heat sink size reduction (%)	36.6	54.5	--
Filtering components size reduction (%)	50	--	--

5.3.4 Regenerative braking

As seen in the general performance section, the regeneration occur within the 0.6 second following the braking command at 0.8 second. There is a 0.1 second waiting time for the regenerative power to reach the threshold of regeneration control. Table 5-16 summarizes the power regenerated back to the battery during this regeneration time period for 25 ºC in KW and percentage of motoring load power of 157 kW.The SiC ACCUFET option gave more power back than the hybrid module with the same order of efficiency as seen in Table 5-15. DC/DC converter switches total losses and efficiency . The following figures present the braking and regenerative related waveforms for the ART railway system.

Table 5-16. Power regenerated back to the battery at 25 ºC junction for the ART

SiC ACCUFET at 100 kHz	6.35 kW	4.0445%
SiC ACCUFET at 50 kHz	6.61 kW	4.21%
Hybrid Switch at 50 kHz	6.51 kW	4.146%

Fig. 5-13 shows the battery current and voltage during regenerative braking for pure Si MOSFET option whereas Fig. 5-14 show the battery SOC ramping up within the period after the regeneration starts. Fig. 5-15 shows the relation between the voltages of the LV and HV sides of the DC/DC converter. Fig. 5-16 and Fig. 5-17 show the vehicle torque and equivalent PMSM speed respectively during braking.

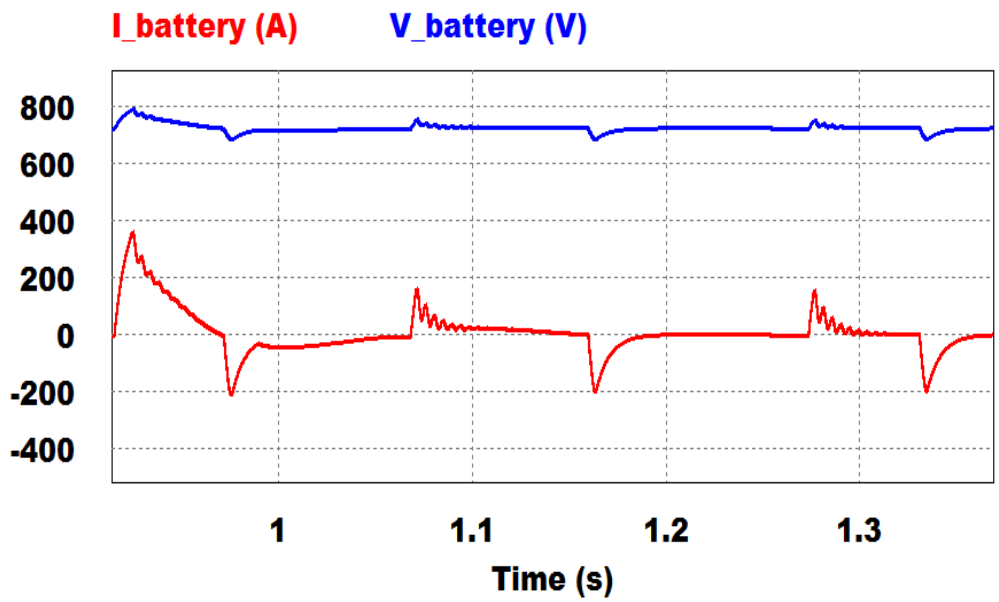

Fig. 5-13. Battery current and voltage during regenerative braking for the ART

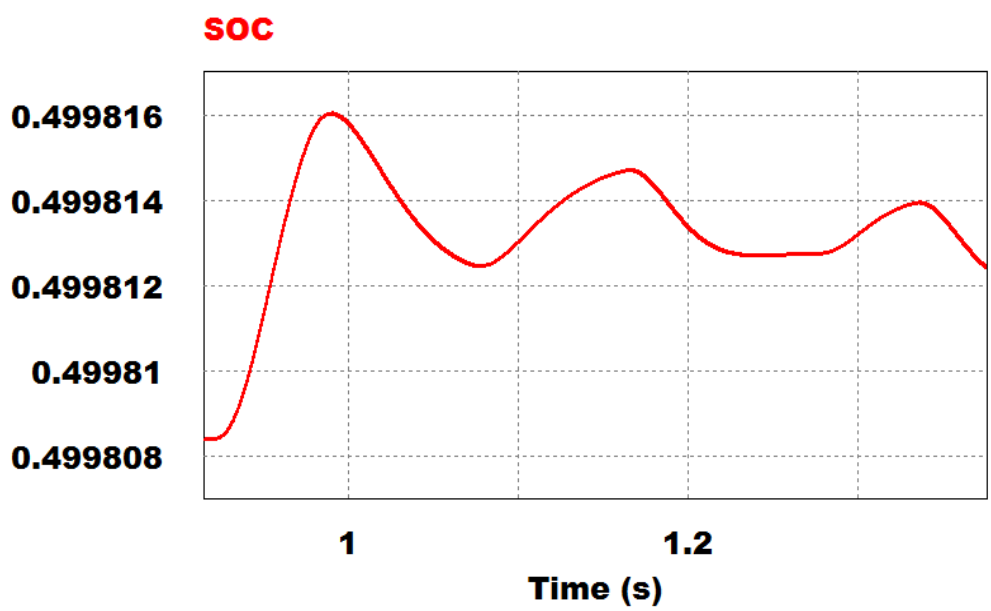

Fig. 5-14. Battery state of charge during regenerative braking for the ART

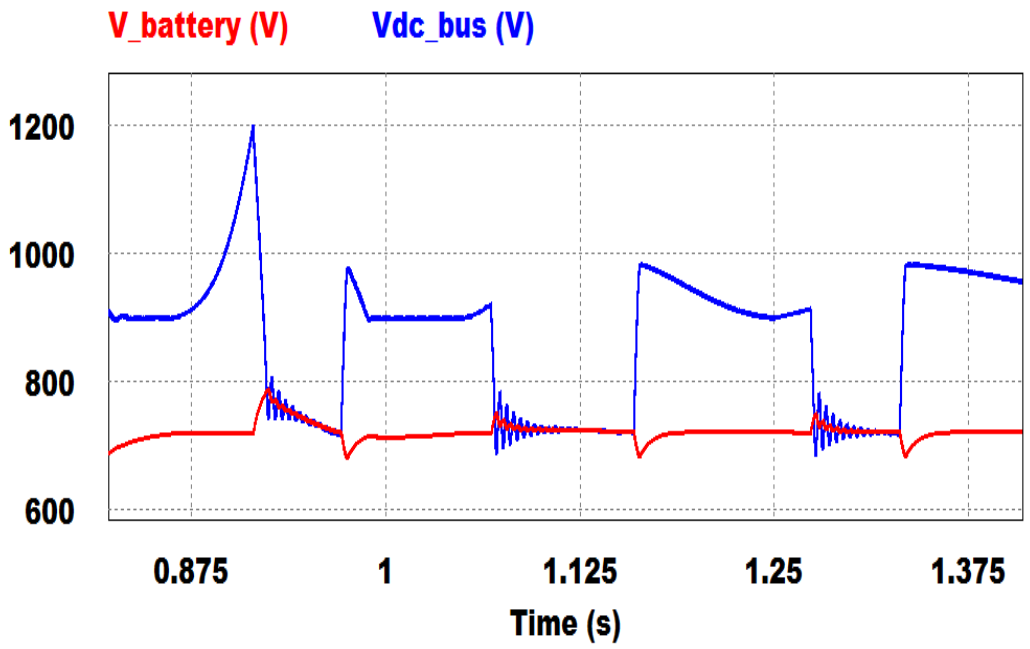

Fig. 5-15. Battery and DC bus voltages during regenerative braking for the ART

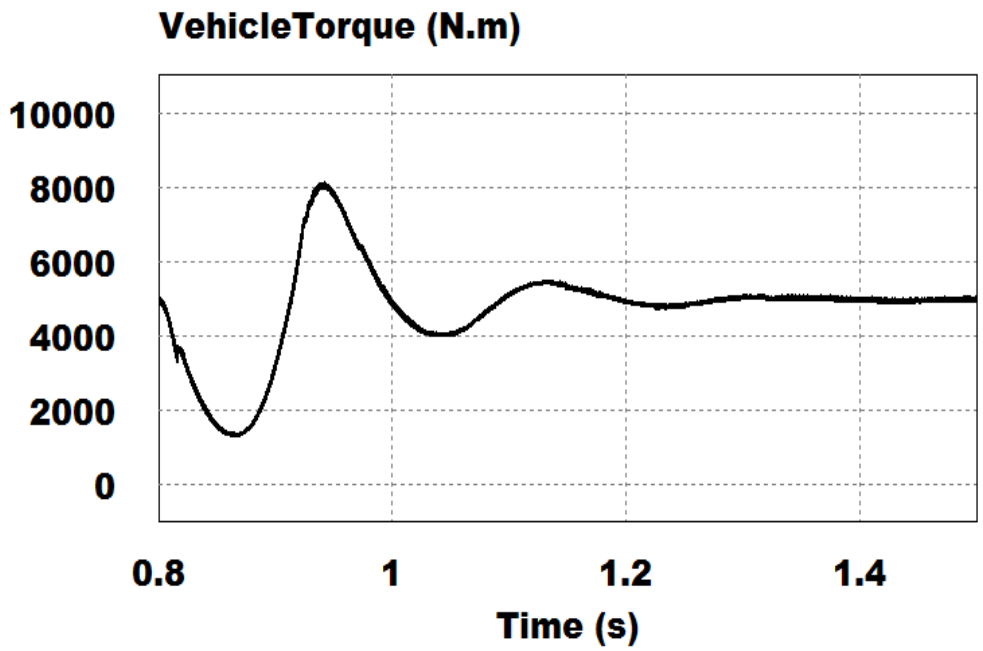

Fig. 5-16. Rail Vehicle torque during braking for ART

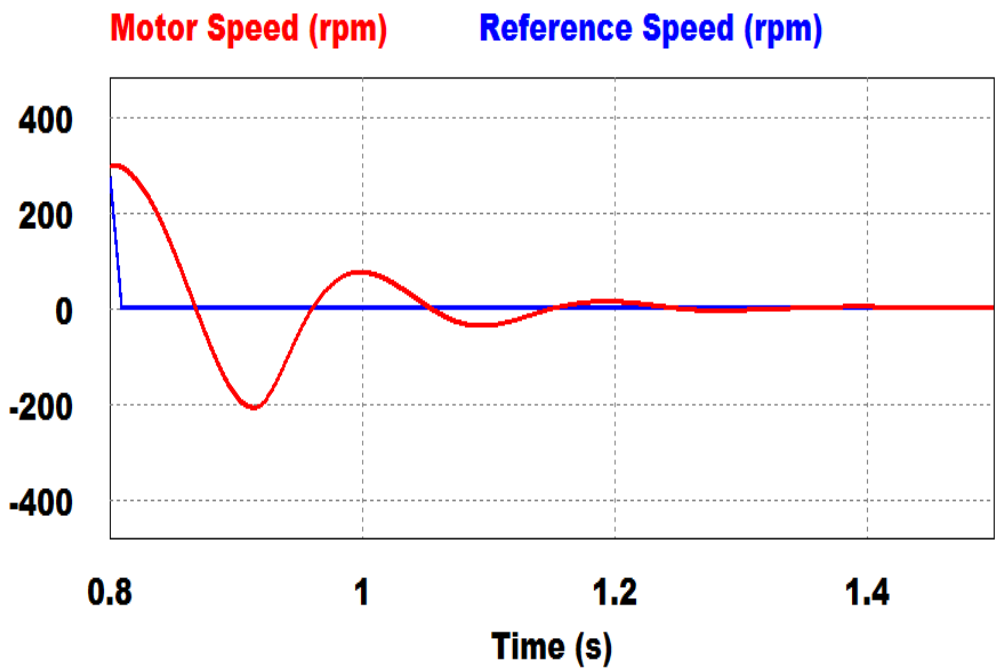

Fig. 5-17. Rail equivalent PMSM speed during braking for ART

5.3.5 Conclusion

Investigating the options available for the ART system, the SiC ACCUFET option even switched at 100 kHz, had lower losses and higher efficiency than the Hybrid Module switched at 50 kHz. This means that the SiC ACCUFET DC/DC converter has 36% lower heatsink size and 50% less filter size; hence, power density and higher mileage than its peer Hybrid Module. Moreover, SiC ACCUFET could give more regeneration power back into the battery at 50 kHz.

Despite the SiC ACCUFET better efficiency, the hybrid module could give slightly higher power back to battery than SiC ACCUFET at 100 kHz even with lower motoring efficiency.

The SiC ACCUFET is a powerful candidate for ART, and any similar high voltage high power applications, that can both boost the conversion efficiency and reduce the size of the filtering components by increasing the switching frequency; hence, increasing the powertrain DC/DC converter's power density and the railway car mileage.

Chapter 6 : The Experimental Test

6.1 The Experimental setup

The experimental setup shown in Fig. 6-1 and Fig. 6-3 was used in the lab to verify the high efficiency of WBG recent technologies; GaN E-HEMT cascode and SiC ACCUFET low loss WBG power semiconductors. The verification is based on watching the switch voltage– current crossover area. This setup consists of the following:

1. Oscilloscope.
2. Signal generator.
3. Multi-meter.
4. 12 V DC Power supply for the gate drive.
5. DC power supply series with a resistor load.
6. Evaluation board including the tested switch and its gate drive.

The specification of each component in the experimental setup are presented in Table 6-1.

Table 6-1. The specification of each component in the experimental setup

	Model	specification
Oscilloscope	Teledyne WaveAce 2004	70 MHz
Signal generator	Aim TTI TG2511A	25 MHz/20 V/11A
Multi-meter	Aim TTI 1705	
Power supply	Aim TTI EX1810R	18 V 10 A
Power resistor	Little Fuse	175 A
Evaluation board including the tested switch and its gate drive.	GS66508T	650 V 30 A
	C2M0080120D	1200 V 30 A

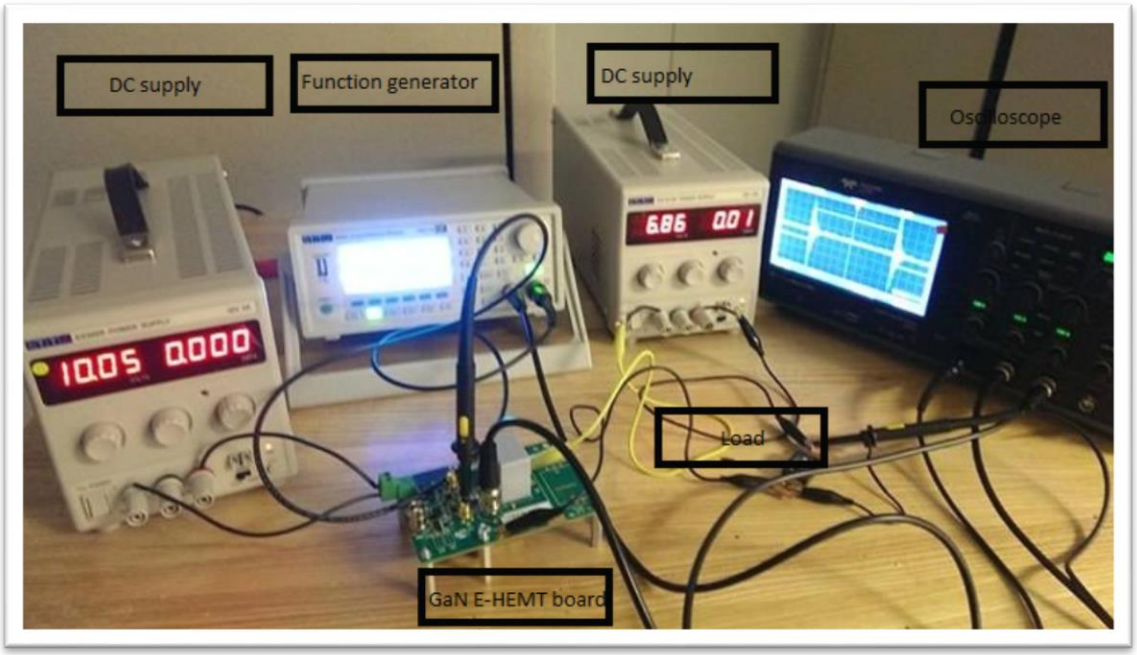

Fig. 6-1. The Experimental setup used for verification of concept with GaN E-HEMT board.

Fig. 6-2 and Fig. 6-4 show the GaN E-HEMT and SiC ACCUFET boards respectively used for verification of WBG power semiconductors high efficiency.

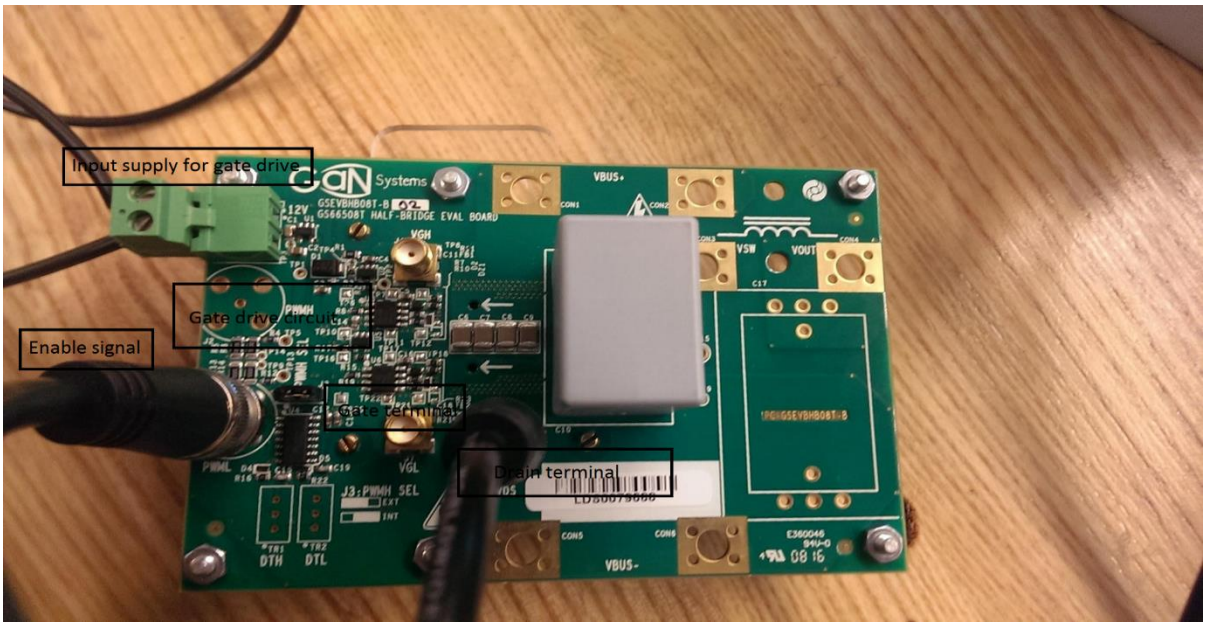

Fig. 6-2. GaN E-HEMT board used for verification of concept from GaN systems [79]

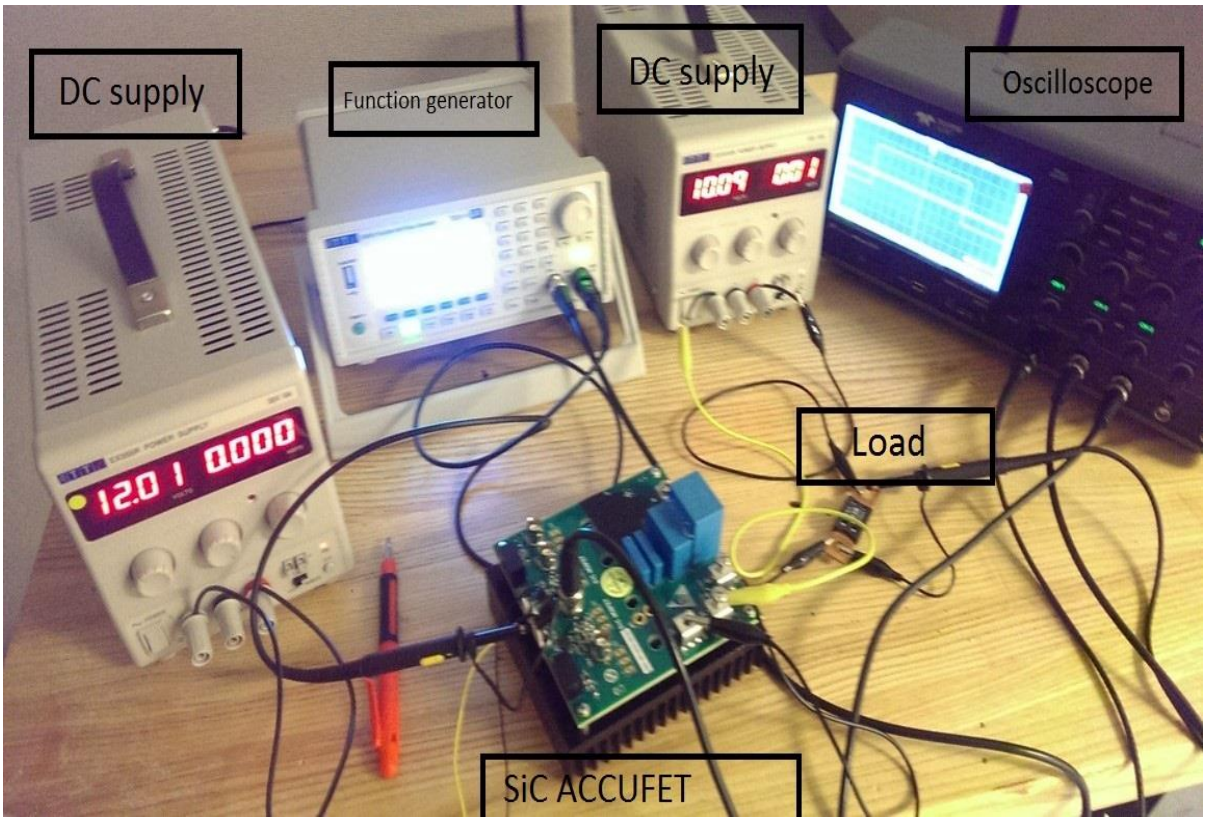

Fig. 6-3. The Experimental setup used for verification of concept with SiC ACCUFET board

Fig. 6-4. SiC ACCUFET evaluation board used for verification of concept from Wolfspeed [31]

6.2 Experimental Results

The following graphs show the gate voltage and the transistor current in a power circuit of a DC supply in series with a 300 W resistor load. The transistors are switched at 10 kHz frequency. These scaled parameters are suitable for lab level tests. Fig. 6-5 presents the oscilloscope snapshot for the GaN E-HEMT gate voltage along with the drain to source voltage. The same waveforms for SiC ACCUFET are seen in **Error! Reference source not found.**. Fig. 6-7 shows the voltage current crossover for the GaN E-HEMT at 10 kHz. As seen, the crossover between the voltage and current waveforms is very small compared to the switching cycle.

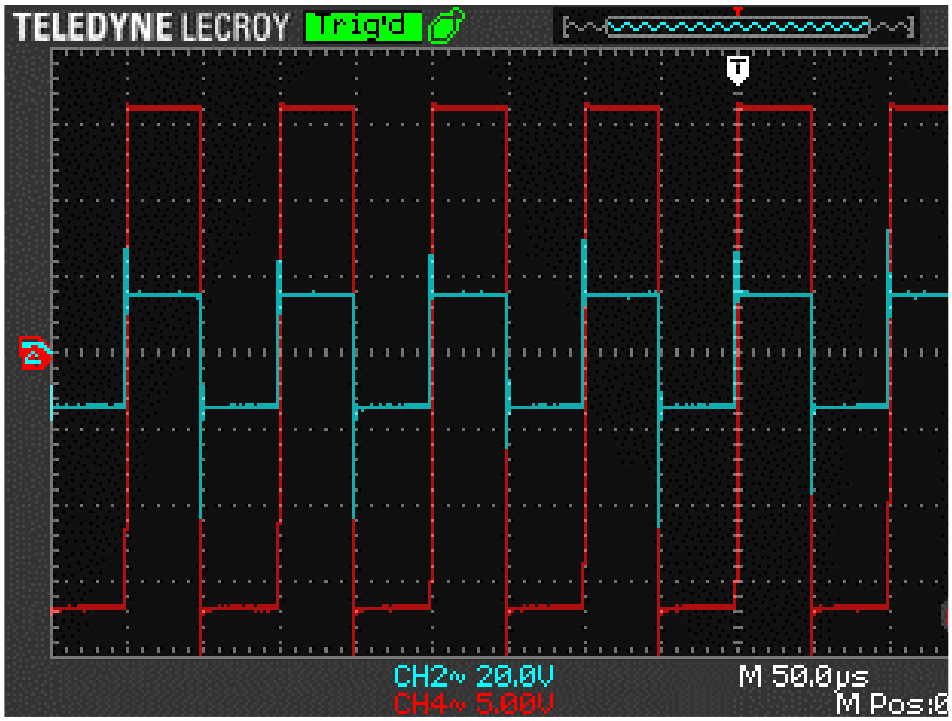

Fig. 6-5. GaN E-HEMT gate voltage (blue) along with the drain to source voltage (Red)

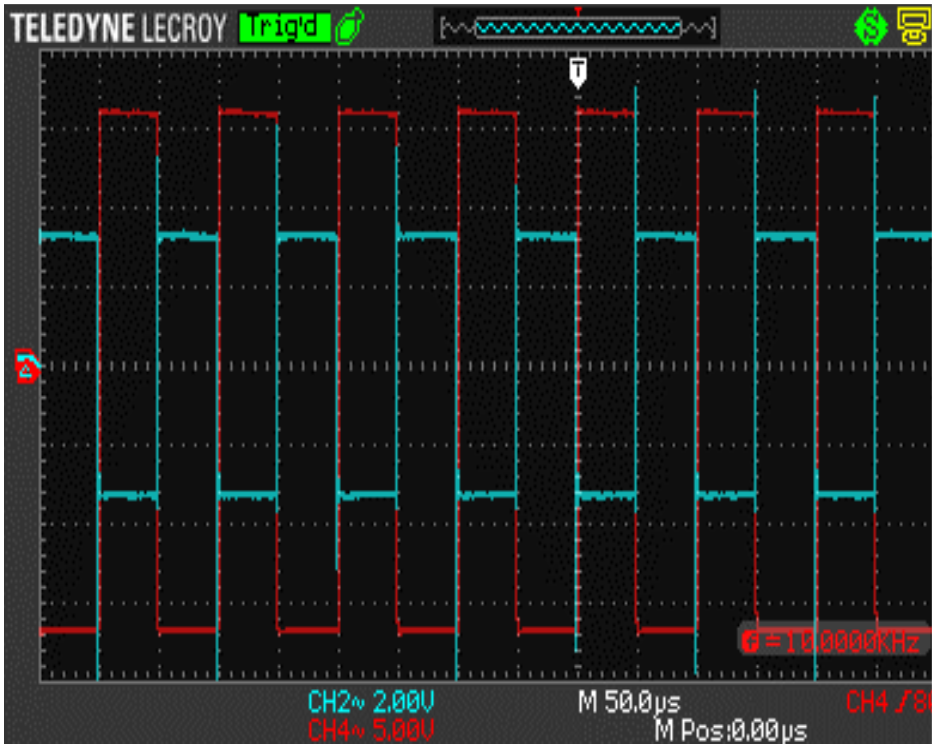

Fig. 6-6. SiC ACCUFET gate voltage (blue) along with the drain to source voltage (Red)

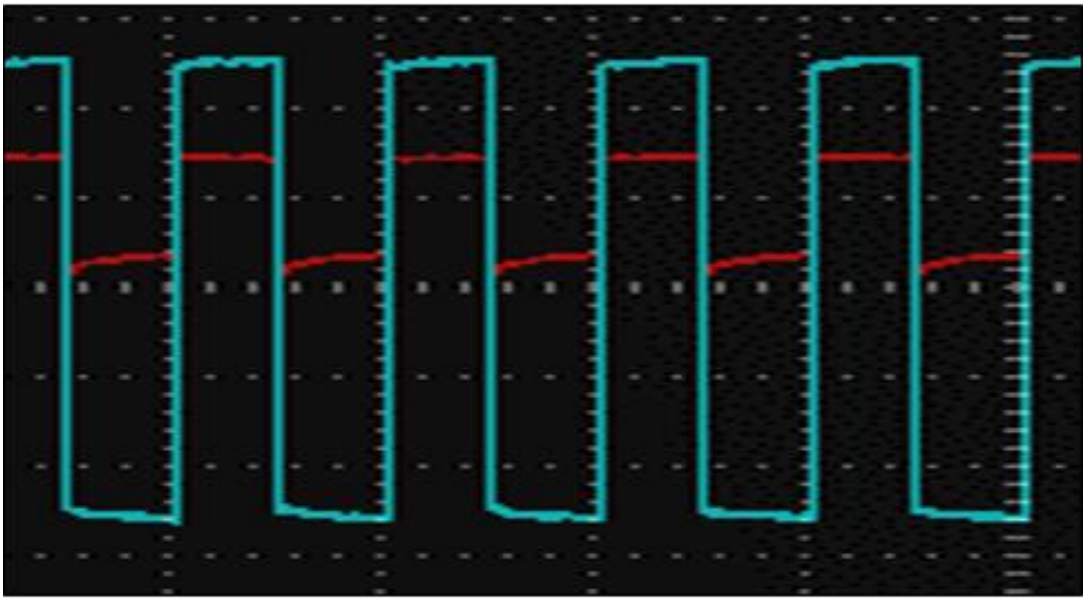

Fig. 6-7. Voltage (Red) current (green) crossover for the GaN E-HEMT at 10 kHz

According to the descaled lab-tested system, the GaN switch can achieve a stable efficiency around 98.7% at 100 kHz switching frequency. SiC ACCUFET can record the same efficiency while switched only at 40 kHz as seen in Table 6-2.

This GaN record efficiency is stable with different switch loading percentages. These findings are in consistence with the simulation results.

Table 6-2.WBG Experimental Efficiencies

	GaN	SiC
f (kHz)	100	40
Efficiency (%)	98.7	98.7

Chapter 7 : Conclusions and Recommendations

Based on the promising characteristics and ratings of GaN and SiC semiconductor devices, at theory, market and applications levels, these Next Generation WBG Semiconductors will change the future of transportation as they concurs the EV motor drive systems replacing the old fashioned Si semiconductors. This thesis presented, for the first time, the utilization of and comparison between GaN E-HEMT cascode, SiC Trench MOSFET(ACCUFET), Hybrid switch of Si IGBT with antiparallel SiC SBD and pure Si MOSFET for the application of DC/DC converter for EV powertrain which have medium to high power and voltage ratings. Using PSIM simulation environment, a successful model of the EV powertrain was built and tested for different load types. According to the case studies carried out in this research, the following conclusions were inferred:

1. Using GaN cascode in the DC/DC converter within the powertrain for road passenger vehicles, an efficiency of 99.65% was achieved with 0.6-0.7% improvement over other options with 60-67% less heat sink footprint.
2. Even at higher junction temperatures, the GaN cascode is still superior with same margin at the same frequency of 50 kHz.
3. The GaN efficiency margin compared to Pure Si MOSFET at 50 kHz go down to 0.13% switching the GaN at 300 kHz, yet, with 83% reduced filtering components and 10% less heatsink size; hence, higher power density.
4. Although more development is needed on lowering the GaN cascode body diode losses, the GaN cascode option has superior efficiency performance compared to other options for road passenger vehicles.
5. The SiC ACCUFET option is not a competitive candidate for road passenger vehicles. This is because its efficiency drops significantly with increased junction temperatures (from 98.99 % down to 98.91%), compared to GaN (99.65 % down to 99.52%) and pure Si MOSFET (99.65 % down to 99.52%).
6. Allowing regenerative braking of traction motors, a regeneration power around 40-45% for road passenger vehicles of motoring power can be returned to the battery for a period that depends on the load inertia. The heavier the load, the more time regeneration will last.

7. The SiC ACCUFET is comparable, in terms of efficiency, to the pure Si MOSFET only while switched at the same frequency of 50 kHz. At higher frequencies, it isn't. However, the SiC ACCUFET can work for higher voltage and higher power applications; e.g. railway, unlike pure Si MOSFET and GaN cascode.
8. Even using SiC SBD in parallel with the Si IGBT in a hybrid module for the DC/DC converter of the railway system, this module couldn't compete with the SiC option that could give higher efficiency up to 100 kHz with an efficiency margin of 0.36% and 54.5% less heatsink size at same switching frequency of 50 kHz.
9. The GaN cascode is a powerful candidate in the DC/DC converter for light road vehicles and similar high voltage medium power applications.
10. The SiC ACCUFET is a powerful candidate in the DC/DC converter for ART and similar high voltage high power applications.
11. Next generation converters will contain WBG devices replacing old fashioned Si devices.

The following sections summarize the claims against and improvements to the WBG semiconductors and the merits of GaN devices over SiC devices where both types are applicable.

7.1 WBG devices Challenges

WBG materials and devices are rapidly gaining acceptance. However, a number of manufacturing challenges was to be addressed to make WBG materials cost effective in more applications according to WBG semiconductors factsheet of the US Energy department at 2013 [9].

- Substrate size and cost: While the quality of GaN and SiC wafers is improving, the cost of producing larger-diameter wafers needs to be reduced. In addition to simpler and cheaper processing than SiC, GaN is grown on cheaper wafers with larger diameters in comparison to SiC wafers. The cost of the substrate could significantly be reduced if the efforts to grow device-quality GaN layers on larger than 150 mm Si wafers, or larger than 150 mm Si wafers covered by monocrystalline SiC, are successful [12].

- Device design and cost: Novel device designs that effectively exploit the properties of WBG materials are needed to achieve the voltage and current ratings required in certain applications. This challenge is addressed already after the appearance of GaN E- HEMT on Si cascode and SiC Trench MOSFETs in the markets last year. This thesis assess these new WBG device designs in the EV powertrain DC/DC converter. Also, alternative packaging materials or designs were also needed to withstand the high temperatures in WBG devices. Architectures that improve manufacturability and affordability are needed to spur commercialization. Many papers tackled this issue [80, 81, 82, 83, 84, 85]. As a result, WBG semiconductor modules and power electronics devices with high current ratings are available in the market.
- Systems integration: The larger, more complex systems must be redesigned to integrate the WBG devices in ways that deliver unique capabilities.

7.2 Merits of GaN over SiC transistors

Presently, Each WBG technology is suited for a specific voltage range as seen in the case studies of this research. GaN-based power devices are being aimed at power supplies in the 200–900 V range, whereas SiC-based power devices are being more tailored for power electronics from 900 to 15,000 V and higher [8]. This can be noticed in the difference between the options available for the NLEV and ART in this study. While SiC devices can withstand higher temperatures and voltages, GaN has the technical advantages of:

1. The potential of GaN for significant cost reduction (cheaper substrates and simpler processing) exceeds SiC. Authors in [12] predict that GaN HEMTs will complement the high voltage applications based on SiC MOSFETs if this advantage is realized.
2. Much higher transconductance and lower gate threshold voltage. According to this fact more gate voltage is needed for SiC to have same current supplied by the counterpart GaN. This is noticed in the available datasheets.
3. Higher Ruggedness (dv/dt): This means faster switching on and off and shorter voltage current cross over even with hard switching and hence lower losses.
4. Inherently small output capacitance and reverse recovery charge: This means improved power efficiency.
5. A very high breakdown field—about 20% higher than in the case of SiC—which also makes it attractive for the development of power switches [12].

References

[1] K. Hamada, M. Nagao, M. Ajioka and F. Kawai, "SiC—Emerging Power Device Technology for Next-Generation Electrically Powered Environmentally Friendly Vehicles," in *IEEE Transactions on Electron Devices*, vol. 62, no. 2, pp. 278-285, Feb. 2015.

[2] F. Luo and H. Ye, Advanced DC/DC Converters, *CRC Press, 2003*.

[3] F. Luo, H. Ye and M. Rashid, Digital Power Electronics and Applications, *Elsevier Academic Press*, 2005.

[4] A. Sandhu, K. Takahashi and A. Yoshikawa, Wide Bandgap Semiconductors: Fundamental Properties and Modern Photonic and Electronic Devices, *Springer*, 2007.

[5] Vincotech, "SiC and GaN Semiconductors in Modules for Higher Efficiency," 2015.

[6] [Online].Available: http://www.fujitsu.com/uk/products/devices/semiconductor/gan/applications

[7] F. Wang, Z. Zhang, T. Ericsen, R. Raju, R. Burgos and D. Boroyevich, "Advances in Power Conversion and Drives for Shipboard Systems," in *Proceedings of the IEEE*, vol. 103, no. 12, pp. 2285-2311, Dec. 2015.

[8] A. Bindra, "Wide-Bandgap-Based Power Devices: Reshaping the power electronics landscape," in *IEEE Power Electronics Magazine*, vol. 2, no. 1, pp. 42-47, March 2015.

[9] U.S. Department of Energy, "Wide Bandgap Semiconductors:Pursuing the Promise," 2013.

[10] X. Huang, Q. Li, Z. Liu and F. C. Lee, "Analytical Loss Model of High Voltage GaN HEMT in Cascode Configuration," in *IEEE Transactions on Power Electronics*, vol. 29, no. 5, pp. 2208-2219, May 2014.

[11] J. Millan, "A review of WBG power semiconductor devices," in *International Semiconductor Conference (CAS)* , Sinai, 2012.

[12] S. Dimitrijeva1, J. Hana2, H. Moghadama and A. Aminbeidokhti, "Power-switching applications beyond silicon: Status and future prospects of SiC and GaN devices," *Materials Research Society (MRS) BULLETIN*, vol. 40, 2015.

[13] - A. Lidow, "Is it the end of the road for silicon in power conversion?," in *6th International Conference on Integrated Power Electronics Systems (CIPS)*, Nuremberg/Germany, 2010.

[14] SANKEN ELECTRIC CO., "Next Generation Power Semiconductors," 2013. [Online]. Available: http://www.semicon.sanken-ele.co.jp/en/guide/GaNSiC.html.

[15] "How to Assemble High Performance GaN Systems," 2014. [Online]. Available:http://www.digikey.ca/en/articles/techzone/2014/apr/how-to-assemble-high-performance-gan-systems.

[16] A. Scharf, "Progress of GaN Transistors," *Power Electronics Europe*, May 2015.

[17] GaN Micro, "Gallium Nitride for 600V operation," *Power Electronics Europe*, 2011.

[18] X. Huang, Z. Liu, Q. Li and F. Lee, "Evaluation and Application of 600 V GaN HEMT in Cascode Structure," *IEEE Transactions on Power Electronics*, vol. 29, no. 5, 2014.

[19] G. Sorrentino, M. Melito, A. Patti and G. Parrino, "GaN HEMT devices: Experimental results on normally-on, normally-off and cascode configuration," in *Industrial Electronics Society, IECON 2013 - 39th Annual Conference of the IEEE,2013.*

[20] S. R. Bahl, "A comprehensive methodology to qualify the reliability of GaN products," *Texas Instruments*, 2015.

[21] S. R. Bahl, D. Ruiz and D. Seup Lee , "Product-level Reliability of GaN Devices," in *IEEE International Reliability Physics Symposium (IRPS)*, 2016.

[22] Y. F. Wu, J. Gritters, L. Shen, R. P. Smith and B. Swenson, "kV-Class GaN-on-Si HEMTs Enabling 99% Efficiency Converter at 800 V and 100 kHz," in *IEEE Transactions on Power Electronics*, vol. 29, no. 6, pp. 2634-2637, June 2014.

[23] Transphorm, "GaN Totem Pole PFC," [Online]. Available: http://www.transphormusa.com/products/#featured-product.

[24] A. Lidow, J. Strydom, R. Strittmatter and C. Zhou, "GaN: A Reliable Future in Power Conversion: Dramatic performance improvements at a lower cost," in *IEEE Power Electronics Magazine*, vol. 2, no. 1, pp. 20-26, March 2015.

[25] C. Liu *et al*., "Breakthroughs for 650-V GaN Power Devices: Stable high-temperature operations and avalanche capability," in *IEEE Power Electronics Magazine*, vol. 2, no. 3, pp. 44-50, Sept. 2015.

[26] Z. Liu, X. Huang, F. C. Lee and Q. Li, "Simulation model development and verification for high voltage GaN HEMT in cascode structure," *2013 IEEE Energy Conversion Congress and Exposition*, Denver, CO, 2013.

[27] EPC, "The Power of a Quarter Brick in the Size of an Eighth Brick - 500 W GaN-based 1/8th Brick DC/DC Converter," *Efficient Power Conversion*, 2015. [Online]. Available: http://epc-co.com/epc/DesignSupport/TrainingVideos/PowerofaQuarterBrickinEighth.aspx.

[28] EPC, "EPC9115 - Development Board," [Online]. Available: http://epc-co.com/epc/Products/DemoBoards/EPC9115.aspx.

[29] Texas Instruments, "LMG3410: 600-V 12-A Single Channel GaN Power Stage," *Texas Instruments*, June 2016. [Online]. Available: http://www.ti.com/product/LMG3410/toolssoftware.

[30] ROHM Semiconductor, "The World's First Trench-Type SiC MOSFET," *ROHM Semiconductor*, [Online]. Available: http://www.rohm.com/web/eu/news-detail?news-title=2015-05-26_ad%3A-trench-type-sic-mosfet&defaultGroupId=false.

[31] Cree, Inc., "Wolfspeed document library," *Cree*, Inc., [Online]. Available: http://www.wolfspeed.com/power/document-library.

[32] Microsemi Semiconductors, "SiC MOSFET," [Online]. Available: http://www.microsemi.com/product-directory/mosfet/3539-sic-mosfet.

[33] ROHM Semiconductors, "Silicon Carbide Schottky Barrier Diodes:acTaking Efficiency to the Next Level for PFC and Other Applications," 2011.

[34] ROHM Semiconductor, "SiC Trench MOSFETs – Performance, Reliability, And Application Examples,"2015.

[35] J. Lu, Q. Tian, K. Bai, A. Brown and M. McAmmond, "An indirect matrix converter based 97%-efficiency on-board level 2 battery charger using E-mode GaN HEMTs," in *IEEE 3rd Workshop on Wide Bandgap Power Devices and Applications (WiPDA)*, Blacksburg, VA, USA, 2015.

[36] L. Xue, M. Mu, D. Boroyevich and P. Mattavelli, "Design of integrated transformer and inductor for high frequency dual active bridge GaN Charger for PHEV," in IEEE Applied Power Electronics Conference and Exposition (APEC), Charlotte, NC, 2015.

[37] L. Xue, M. Mu, D. Boroyevich and P. Mattavelli, "The optimal design of GaN-based Dual Active Bridge for bi-directional Plug-IN Hybrid Electric Vehicle (PHEV) charger," *2015 IEEE Applied Power Electronics Conference and Exposition (APEC)*, Charlotte, NC, 2015.

[38] D. Han, J. Noppakunkajorn and B. Sarlioglu, "Comprehensive Efficiency, Weight, and Volume Comparison of SiC- and Si-Based Bidirectional DC–DC Converters for Hybrid Electric Vehicles," *IEEE Transactions on vehicular technology*, vol. 63, no. 7, 2014.

[39] X. Zhang, C. Yao, C. Li, L. Fu, F. Guo and J. Wang, "A Wide Bandgap Device-Based Isolated Quasi-Switched-Capacitor DC/DC Converter.pdf," *IEEE Transactions on Power Electronics*, vol. 29, no. 5, 2015.

[40] T. E. Salem and R. A. Wood, "1000-H Evaluation of a 1200-V, 880-A All-SiC Dual Module," in IEEE Transactions on Power Electronics, vol. 29, no. 5, pp. 2192-2198, May 2014.

[41] S. Jahdi, O. Alatise, C. Fisher, L. Ran and P. Mawby, "An Evaluation of Silicon Carbide Unipolar Technologies for Electric Vehicle Drive-Trains," *IEEE Journal of emerging and selected topics in Power Electronics*, vol. 2, no. 3, 2014.

[42] G. J. Su and L. Tang, "An integrated onboard charger and accessory power converter using WBG devices," *2015 IEEE Energy Conversion Congress and Exposition (ECCE)*, Montreal, QC, 2015.

[43] B. Whitaker, A. Barkley, Z. Cole, B. Passmore, D. Martin, T. McNutt, A. Lostetter, J. S. Lee and K. Shiozaki, "A High-Density, High-Efficiency, Isolated On-Board Vehicle Battery Charger Utilizing Silicon Carbide Power Devices," *IEEE Transactions on Power Electronics*, vol. 29, no. 5, 2015.

[44] E. A. Jones, F. Wang, D. Costinett, Z. Zhang and B. Guo, "Temperature-dependent turn-on loss analysis for GaN HFETs," *2016 IEEE Applied Power Electronics Conference and Exposition (APEC)*, Long Beach, CA, 2016.

[45] M. Kuzuhara and H. Tokuda, "Low-Loss and High-Voltage III-Nitride Transistors for Power Switching Applications," in *IEEE Transactions on Electron Devices*, vol. 62, no. 2, pp. 405-413, Feb. 2015.

[46] A. Lidow and R. Strittmatter, "Enhancement mode gallium nitride transistor reliability," *DC Microgrids (ICDCM), 2015 IEEE First International Conference on*, Atlanta, GA, 2015.

[47] L. Herrera, C. Li, X. Yao and J. Wang, "FPGA-Based Detailed Real-Time Simulation of Power Converters and Electric Machines for EV HIL Applications," in *IEEE Transactions on Industry Applications*, vol. 51, no. 2, pp. 1702-1712, March-April 2015.

[48] Z. Saif, V. Ahmad and G. E. Town, "Compact SEPIC converter using a GaN HEMT," *2015 9th International Conference on Power Electronics and ECCE Asia (ICPE-ECCE Asia)*, Seoul, 2015.

[49] X. Huang, F. C. Lee, Q. Li and W. Du, "MHz GaN-based interleaved CRM bi-directional buck/boost converter with coupled inductor," *2015 IEEE Applied Power Electronics Conference and Exposition (APEC)*, Charlotte, NC, 2015.

[50] R. Perrin, N. Quentin, B. Allard, C. Martin and M. Ali, "High Temperature GaN Active-Clamp Flyback Converter with Resonant Operation Mode," *IEEE Journal of Emerging and Selected Topics in Power Electronics*, no. 99, 2016.

[51] M. D. Seeman, "GaN Devices in Resonant LLC Converters: System-level considerations," IEEE Power Electronics Magazine, vol. 2, no. 1, 2015.

[52] H. Sarnago, O. Lucia, A. Mediano and J. Burdio, "Full-bridge quasi-resonant class-DE inverter for optimized high frequency operation with GaN HEMT devices," in IEEE Applied Power Electronics Conference and Exposition (APEC), 2014.

[53] E. Gurpinar and A. Castellazzi, "Single-Phase T-Type Inverter Performance Benchmark Using Si IGBTs, SiC MOSFETs, and GaN HEMTs," in *IEEE Transactions on Power Electronics*, vol. 31, no. 10, pp. 7148-7160, Oct. 2016.

[54] J. Liu, K. L. Wong, S. Allen and J. Mookken, "Performance Evaluations of Hard-Switching Interleaved DC/DC Boost Converter with New Generation Silicon Carbide MOSFETs," [Online]. Available: http://www.wolfspeed.com/.

[55] T. Kim, M. Jang and V. G. Agelidis, "Practical implementation of a silicon carbide-based 300 kHz, 1.2 kW hard-switching boost-converter and comparative thermal performance evaluation," in *IET Power Electronics*, vol. 8, no. 3, pp. 333-341, 3 2015.

[56] A. Merkert, T. Krone and A. Mertens, "Characterization and Scalable Modeling of Power Semiconductors for Optimized Design of Traction Inverters with Si- and SiC-Devices," *IEEE Transactions on Power Electronics*, vol. 29, no. 5, 2014.

[57] National Electrical Manufacturers Association (NEMA), "Application Guide for AC Adjustable Speed Drive Systems," July 2015. [Online]. Available: https://www.nema.org/standards/pages/application-guide-for-ac-adjustable-speed-drive-systems.aspx?.

[58] K. Reif, "Regenerative braking system," in Fundamentals of Automotive and Engine Technology, Springer , 2014.

[59] Y. S. Lin, K. W. Hu, T. H. Yeh and C. M. Liaw, "An Electric-Vehicle IPMSM Drive With Interleaved Front-End DC/DC Converter," in *IEEE Transactions on Vehicular Technology*, vol. 65, no. 6, pp. 4493-4504, June 2016.

[60] T. Ishikawa and X. Cao, "Optimum design of a regenerative braking system for electric vehicles based on fuzzy control strategy," in *Ieej Transactions on Electrical and Electronic Engineering*, vol. 11, 2016.

[61] S. Lu, P. Weston, S. Hillmansen, H. B. Gooi and C. Roberts, "Increasing the Regenerative Braking Energy for Railway Vehicles," in *IEEE Transactions on Intelligent Transportation Systems*, vol. 15, no. 6, pp. 2506-2515, Dec. 2014

[62] D. Montesinos-Miracle, M. Massot-Campos, J. Bergas-Jane, S. Galceran-Arellano and A. Rufer, "Design and Control of a Modular Multilevel DC/DC Converter for Regenerative Applications," in *IEEE Transactions on Power Electronics*, vol. 28, no. 8, pp. 3970-3979, Aug. 2013

[63] P. Mendonça, J. F. A. da Silva, D. M. Sousa and S. F. Pinto, "An approach to recover braking energy of a tram," *2014 IEEE 5th International Symposium on Power Electronics for Distributed Generation Systems (PEDG)*, Galway, 2014, pp. 1-6.

[64] G. Zulauf, W. Treichler and J. Castelaz, "System, method, and results for the regenerative burn-in testing of high-power DC-DC converters," *Transportation Electrification Conference and Expo (ITEC), 2015 IEEE*, Dearborn, MI, 2015, pp. 1-6

[65] A. Caratti, G. Catacchio, C. Gambino and N. C. Kar, "Development of a predictive model for Regenerative Braking System," *Transportation Electrification Conference and Expo (ITEC), 2013 IEEE*, Detroit, MI, 2013, pp. 1-6.

[66] H. A. Yavasoglu, J. Shen, C. Shi, M. Gokasan and A. Khaligh, "Power Split Control Strategy for an EV Powertrain With Two Propulsion Machines," in *IEEE Transactions on Transportation Electrification*, vol. 1, no. 4, pp. 382-390, Dec. 2015.

[67] B. Wang, M. Xu and L. Yang, "Study on the economic and environmental benefits of different EV powertrain topologies," *Energy Conversion and Management*, vol. 86, pp. 916-926, 2014.

[68] G. Wu, X. Zhang and Z. Dong, "Powertrain architectures of electrified vehicles: Review, classification and comparison," *Journal of the Franklin Institute*, vol. 352, p. 425–448, 2015.

[69] M. Hu, J. Zeng, S. Xu, C. Fu and D. Qin, "Efficiency Study of a Dual-Motor Coupling EV Powertrain," in *IEEE Transactions on Vehicular Technology*, vol. 64, no. 6, pp. 2252-2260, June 2015.

[70] H. Mejbri, K. Ammous, S. Abid, H. Morel, and A. Ammous, "Bi-objective sizing optimization of power converter using genetic algorithms,"*COMPEL - The international journal for computation and mathematics in electrical and electronic engineering*, vol. 33, no. 1/2, pp. 398–422, Dec. 2013.

[71] D. J. Perreault, "In Search of Powerful Circuits: Developments in Very High Frequency Power Conversion," *AndlingerCenter at Princeton University*, 2014.

[72] Infineon, 2012. [Online]. Available: http://www.infineon.com/cms/en/product/power/power-mosfet/20v-650v-automotive-osfet/650v-n-channel-automotive-mosfet/IPW65R048CFDA/.

[73] NISSAN, "Nissan Leaf 2016," [Online]. Available: http://www.nissanusa.com/electric-cars/leaf/versions-specs/.

[74] NISSAN, "Nissan Leaf 2016," 2016. [Online]. Available: http://experience.nissan.it/dam/services/gb/brochure/Nissan_Leaf.pdf.

[75] Infineon, "650 V N-Channel Automotive MOSFET," 2012. [Online]. Available: http://www.infineon.com/cms/en/product/power/power-mosfet/20v-650v-automotive-mosfet/650v-n-channel-automotive-mosfet/IPW65R048CFDA/.

[76] Transphorm, "Products," 2015. [Online]. Available: http://www.transphormusa.com/products.

[77] SEMIKRON, Inc., "SEMIKRON Hybrid SiC modules," SEMIKRON, Inc., [Online]. Available: http://www.semikron.com/products/product-classes/sic/hybrid-sic.html.

[78] KOKAM, "Kokam EV Module Structure," [Online]. Available: http://kokam.com/electric-vehicle-2-2/.

[79] GaN Systems Inc, "Gallium Nitride Power Conversion Semiconductors Tomorrow's Power Today," [Online]. Available: http://www.gansystems.com/gs66508t-evbhb.php.

[80] L. Kumar, K. K. Gupta and S. Jain, "Architecture and configuration of electrified vehicles: A review," *Industrial Electronics (ISIE), 2013 IEEE International Symposium on*, Taipei, Taiwan, 2013, pp. 1-6.

[81] F. C. Lee, W. Zhang, X. Huang, Z. Liu, W. Du and Q. Li, "A new package of high-voltage cascode gallium nitride device for high-frequency applications," *Integrated Power Packaging (IWIPP), 2015 IEEE International Workshop on*, Chicago, IL, 2015, pp. 9-15.

[82] Z. Liu, X. Huang, F. Lee and Q. Li, "Package Parasitic Inductance Extraction and Simulation Model Development for the High-Voltage Cascode GaN HEMT," *IEEE Transactions on Power Electronics*, vol. 29, no. 4, 2015.

[83] Z. Liu, X. Huang, W. Zhang, F. Lee and Q. Li, "Evaluation of high-voltage cascode GaN HEMT in different packages," in *IEEE Applied Power Electronics Conference and Exposition (APEC), 2014*.

[84] D. Murthy-Bellur, E. Ayana, S. Kunin and B. Palmer, "WBG inverter for commercial power generation and vehicle electrification," in *IEEE International Workshop on Integrated Power Packaging (IWIPP)*, Chicago, IL.

[85] K. Shenai, "Wide bandgap (WBG) semiconductor power device datasheets and circuit models," in *IEEE International Workshop on Integrated Power Packaging (IWIPP)*, Chicago, IL, 2012.

[86] J. F. Gieras, Permanent magnet motor technology : design and applications, 3rd ed., *CRC Press, Taylor & Francis Group*, 2010.

[87] C. C. Chan and K. T. Chau, "An advanced permanent magnet motor drive system for battery-powered electric vehicles," in *IEEE Transactions on Vehicular Technology*, vol. 45, no. 1, pp. 180-188, Feb 1996.

[88] B. Bilgin and A. Sathyan, "Fundamentals of Electric Machines," in *Advanced Electric Drive Vehicles, CRC Press*, Oct 2014, pp. 107 -186 .

[89] Y. Le, J. Fang and J. Sun, "Design of a Halbach Array Permanent Magnet Damping System for High Speed Compressor With Large Thrust Load," in *IEEE Transactions on Magnetics*, vol. 51, no. 1, pp. 1-9, Jan. 2015.

[90] C. Choi, W. Lee, S. O. Kwon and J. P. Hong, "Experimental Estimation of Inductance for Interior Permanent Magnet Synchronous Machine Considering

Temperature Distribution," in *IEEE Transactions on Magnetics*, vol. 49, no. 6, pp. 2990-2996, June 2013.

[91] H. K. Jussila, A. V. Mityakov, S. Z. Sapozhnikov, V. Y. Mityakov and J. Pyrhönen, "Local Heat Flux Measurement in a Permanent Magnet Motor at No Load," in *IEEE Transactions on Industrial Electronics*, vol. 60, no. 11, pp. 4852-4860, Nov. 2013.

[92] M. Ganchev, C. Kral and T. M. Wolbank, "Compensation of Speed Dependence in Sensorless Rotor Temperature Estimation for Permanent-Magnet Synchronous Motor," in *IEEE Transactions on Industry Applications*, vol. 49, no. 6, pp. 2487-2495, Nov.-Dec. 2013.

[93] J. M. Miller, Propulsion systems for HEV, *The Institution of Engineering and Technology*, 2010.

[94] J. R. Hendershot, "Electric traction machine choices for hybrid & electric vehicles" 2014. [Online]. Available: sites.ieee.org/miami/files/2014/11/Hendershot-FIU-Lecture.pdf.

[95] Malcolm Burwell, "Performance/cost comparison of induction-motor & permanent-magnet-motor in a hybrid electric car," *International Copper Association*, Tokyo, 2013.

[96] M. Burwell, J. Goss and M. Popescu, "Performance/cost comparison of induction motor & permanent magnet motor in a hybrid electric car," *International Copper Association*, Tokyo, 2013.

[97] Toshiba Corporation, "Permanent Magnet Synchronous Motor for Traction Systems," August 2014. [Online]. Available: http://toshiba-railway.com.

[98] P. Magne, X. Shi and M Krishnamurthy , "Fundamentals of Power Electronics," in Advanced Electric Drive Vehicles, CRC Press, Oct 2014, pp. 45-106.

[99] Research and Markets, "Advanced Batteries Market to 2020 - Demand for Electric Vehicles to Drive Growth, Asia Pacific to Remain the Major Producer," Energy business journal, vol. 42, 2012.

[100] "A Tutorial on Hybrid Electric Vehicles: EV, HEV, PHEV and FCEV," IEEE Proceedings Summary.

[101] Automotive Energy Supply Corporation (AESC), "Definition of Lithium-ion Batteries," Automotive Energy Supply Corporation (AESC), 2013. [Online]. Available: http://www.eco-aesc-lb.com/en/about_liion/.

[102] Robert Bosch GmbH, "An Innovative leap: On the cutting edge with solid state technology," Robert Bosch GmbH, September 2015. [Online]. Available: http://www.bosch.com/en/com/boschglobal/csr_battery_technology/an_innovative_leap/an-innovative-leap.html.

[103] Bombardier, "MITRAC Converter brochure," [Online]. Available: http://www.bombardier.com/content/dam/Websites/bombardiercom/supporting-documents/BT/Bombardier-Transportation-MITRAC.pdf.

[104] S. H. Jr., "SiC Schottky Diodes in Power Factor Correction," *Power Electronics Technology*.

[105] Y. Zhang, M. Rodriguez and D. Maksimovic, "Very High Frequency PWM Buck Converters Using Monolithic GaN Half-Bridge Power Stages with Integrated Gate Drivers," *IEEE Transactions on Power Electronics*, no. 99, 2015.

[106] M. Ando and K. Wada, "A normalization procedure of DC-side stray inductance for high-speed switching circuit," *2016 IEEE Applied Power Electronics Conference and Exposition (APEC)*, Long Beach, CA, 2016, pp. 2986-2991.

[107] R. Perrin, N. Quentin, B. Allard, C. Martin and M. Ali, "High-Temperature GaN Active-Clamp Flyback Converter With Resonant Operation Mode," in *IEEE Journal of Emerging and Selected Topics in Power Electronics*, vol. 4, no. 3, pp. 1077-1085, Sept. 2016.

[108] N. K. Subramani *et al*., "Characterization of Parasitic Resistances of AlN/GaN/AlGaN HEMTs Through TCAD-Based Device Simulations and On-Wafer Measurements," in *IEEE Transactions on Microwave Theory and Techniques*, vol. 64, no. 5, pp. 1351-1358, May 2016.

[109] E. A. Jones, F. Wang, D. Costinett, Z. Zhang and B. Guo, "Temperature-dependent turn-on loss analysis for GaN HFETs," *2016 IEEE Applied Power Electronics Conference and Exposition (APEC)*, Long Beach, CA, 2016, pp. 1010-1017.

[110] B. M. Paine, T. Rust and E. A. Moore, "Measurement of Temperature in GaN HEMTs by Gate End-to-End Resistance," in *IEEE Transactions on Electron Devices*, vol. 63, no. 2, pp. 590-597, Feb. 2016.

[111] Transphorm, 2015. [Online]. Available: http://www.transphormusa.com/products.

[112] B. J. Baliga, Advanced Power MOSFET Concepts, Springer, 2014.

[113] "Battery module packaging," [Online]. Available: http://www.enginetechnologyinternational.com/akasol.php.

[114] Texas Instruments, "Choosing Inductors and Capacitors for DC/DC Converters," 2001. [Online].

[115] R. Grezaud, F. Ayel, N. Rouger and J. C. Crebier, "A Gate Driver With Integrated Deadtime Controller," in *IEEE Transactions on Power Electronics*, vol. 31, no. 12, pp. 8409-8421, Dec. 2016.

[116] Y. Zhang, M. Rodríguez and D. Maksimović, "Very High Frequency PWM Buck Converters Using Monolithic GaN Half-Bridge Power Stages With Integrated Gate Drivers," in *IEEE Transactions on Power Electronics*, vol. 31, no. 11, pp. 7926-7942, Nov. 2016.

[117] E. Gurpinar and A. Castellazzi, "Single-Phase T-Type Inverter Performance Benchmark Using Si IGBTs, SiC MOSFETs, and GaN HEMTs," in *IEEE Transactions on Power Electronics*, vol. 31, no. 10, pp. 7148-7160, Oct. 2016.

[118] P. Czyż, "Performance evaluation of a 650V E-HEMT GaN power switch," *Industrial Electronics Society, IECON 2015 - 41st Annual Conference of the IEEE*, Yokohama, 2015

[119] J. Shen and J. Wang, "Guest Editorial Special Issue on Wide Bandgap Power Devices and Applications," in *IEEE Journal of Emerging and Selected Topics in Power Electronics*, vol. 4, no. 3, pp. 705-706, Sept. 2016.

.

[120] https://ei.uni-paderborn.de/en/lea/research/forschungsprojekte/electrical-drives-and-mechatronic-systems/control-of-permanent-magnet-synchronous-motors-for-automotive-applications/

[121] Mohanty, M. K. (2014). Direct torque control of permanent magnet synchronous motor drives with conventional and svm approach . Rourkela: National Institute of Technology.

[122] http://vancouversun.com/news/local-news/evergreen-line-between-burnaby-and-coquitlam-to-be-operating-before-christmas

[123] Y. Attia, A. Abdelrahman, M. Hamouda and M. Youssef, "SiC devices performance overview in EV DC/DC converter: A case study in a Nissan Leaf," 2016 *IEEE Transportation Electrification Conference and Expo*, Asia-Pacific (ITEC Asia-Pacific), Busan, 2016, pp. 214-219.

[124] Y. Attia and M. Youssef, "GaN on Silicon E-HEMT and Pure Silicon MOSFET in High Frequency Switching of Electric Vehicle DC/DC," 2*016 IEEE 38th International Telecommunications Energy Conference (INTELEC)*, Austin, TX, 2016.

[125] A. Abdelrahman; Y. Attia; K. Woronowicz; M. Z. Youssef, "Hybrid Fuel Cell/Battery Rail Car: A Feasibility Study," in *IEEE Transactions on Transportation Electrification* , vol.PP, no.99. Early access.

Chapter 8 : Appendix I: EV Powertrain System Background

8.1.1 EV Traction Motor Drive

Recent EV Motor drives are selected to be an AC bidirectional drive that permits four quadrant operation. They consists of a 3-phase inverter, a traction motor, and the traction motor controller. This controller guide the motor to follow the torque and speed commands of the vehicle load. At the same time, the 3-phase inverter converts the DC bus voltage supply coming from the battery through a DC/DC converter into 3-phase supply for the traction AC motor. Below is the illustration for the EV drive parts in detail.

8.1.2 Permanent Magnet Synchronous Motor (PMSM)

The PMSM is a synchronous motor with PMs for excitation replacing the field circuit. This modification mitigates the rotor copper loss and maintenance. PM motors cover a wide variety of applications, from small stepping motors, through industrial drives traction motors for vehicles and ships [86]. Availability of high-energy neodymium-iron-boron (Nd-Fe-B) permanent magnet (PM) material has focused attention in 1996 on the use of the PMSM drive for electric vehicles (EVs). The authors in [87] presented a Nd-Fe-B PMSM for a 3.2 kW mini-EV prototype in 1996. This drive system had high efficiency and power density.

PM motors possess many advantages over its peers as follow:

1. Higher efficiency compared to induction motors because of no excitation field current and associated loss.
2. Simpler construction and lower maintenance compared to brush machines.
3. Lower cooling demand compared to wound rotor machines.
4. Lower noise and vibration than induction machines and switched reluctance.
5. Fast response due to less rotor inertia and higher air gab flux density.
6. Savings in energy and size because of high power and torque densities motivated by higher flux density.

The main disadvantage of PMSM is the high cost of the PMs, and its sensitivity to temperature and load conditions. Many recent research was dedicated to mitigating the effect of these disadvantages [88] [89] [90] [91] [92].

8.1.2.1 PMSM Construction

Similar to synchronous machines, PMSM consists of a stator and a rotor as seen in Fig. 8-1.

8.1.2.1.1 The stator

This is a mechanically fixed part connected to the external terminals, output for generator and input for motor. Usually in propulsion applications, the stator is wound as a 3 phase star-connection. The stator an iron part and windings producing the stator magnetic flux.

8.1.2.1.2 The rotor

The rotor is a mechanical part that is free to rotate around a shaft. It contains two parts: magnetically conductive iron part, and PMs which is the source of the rotor's magnetic field. These magnets are organized in north and south pattern alternately. MMF produced by the stator currents crosses the air gap and links the PM flux.

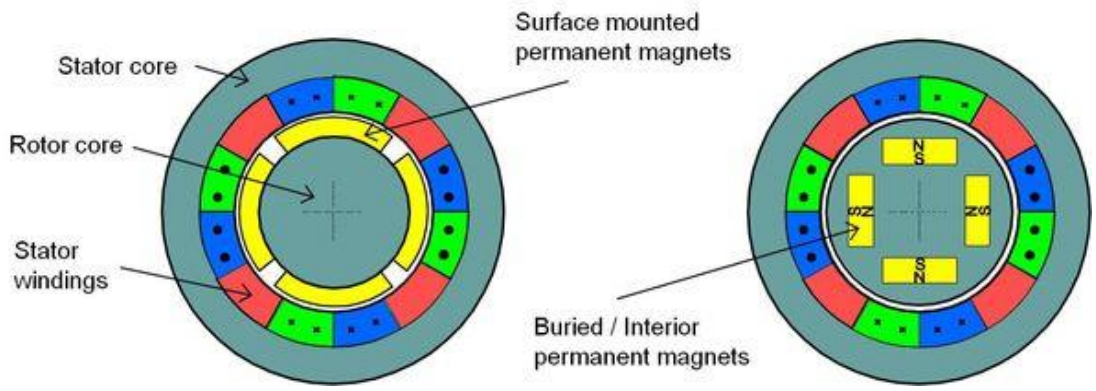

Fig. 8-1. Cross section view of permanent magnet machines (a) surface permanent magnet machine (SPM) (b) interior permanent magnet machine (IPM) [120]

8.1.2.2 PMSM Operation

The rotor rotates as a response to the interaction between stator and rotor fluxes. The EMF induced back in the stator windings as a result of the flux linkage variation due to rotation cause stator phase currents. These currents interact with the corresponding back EMFs producing the electromagnetic torque. As a synchronous motor, the rotor of PMSM has no electrical connections to the stator. A position sensor senses and feedback the rotor position to the motor control circuit to manage the motor operation. In case of sensorless control, these positions are estimated through an estimation algorithm. In this research, sensors provide the positions feedback to the control circuit. Fig. 8-2 presents the torque-speed characteristics for a PMSM traction motor. The region below the base speed, ω_b, is a constant torque region where MTPA algorithm can be applied. From ω_b to ω_{max}, is a constant power region that is obtained by rotor's field weakening; the torque decreases inversely with the speed by means of field weakening.

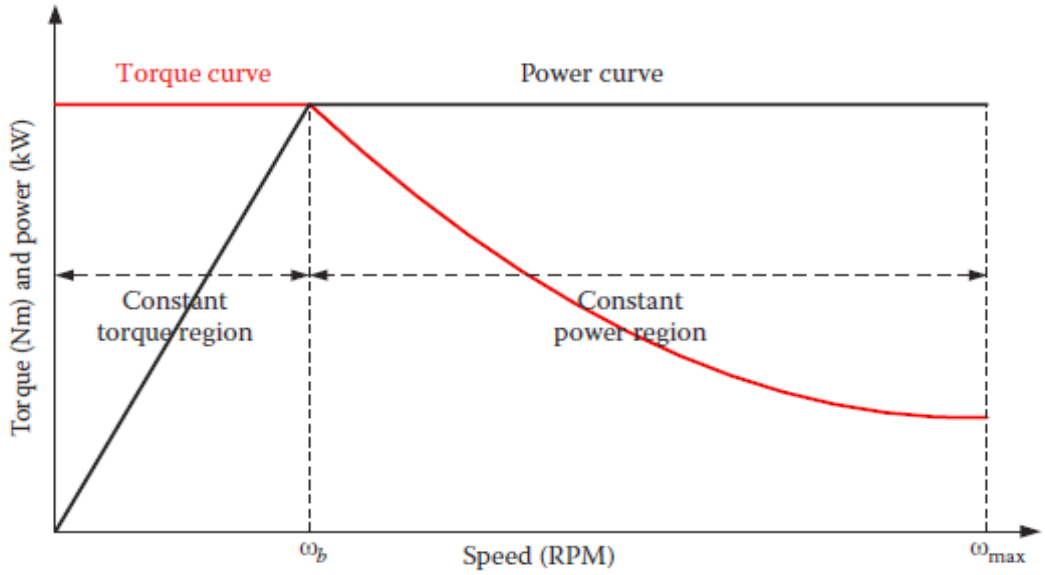

Fig. 8-2. Torque-speed characteristics for a PMSM traction motor [88]

Fig. 8-3 describes the four quadrant operation of a PMSM machine. Each quadrant has the torque-speed characteristics of Fig. 8-2. Quadrant I represents forward motoring (Traction) and Quadrant II is the forward braking. Quadrants III and IV represent the reverse traction and braking respectively. The output motor torque is negative for braking.

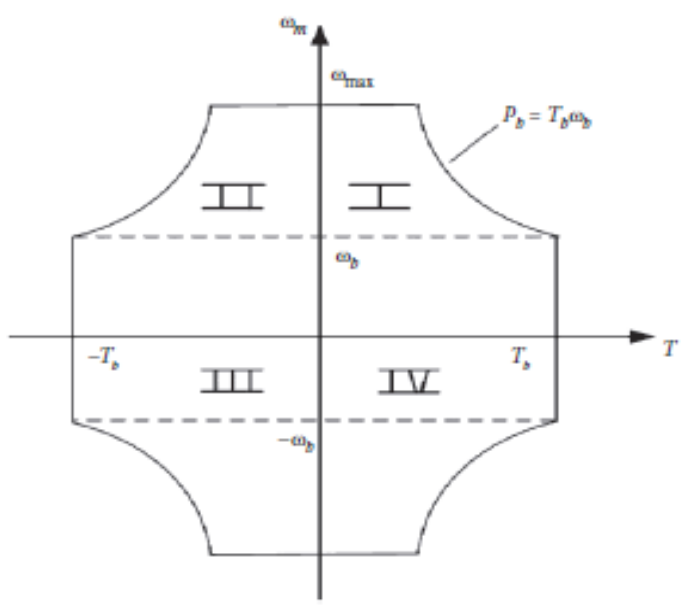

Fig. 8-3. Four-quadrant operation of a PMSM [88]

8.1.2.3 Classification of PM Machines

Based on the back EMF shape, PMSM machines are divided into sinusoidal (PMSM) and trapezoidal (Brushless DC) machines. This difference in back EMF shape is caused by the different PMs magnetization orientation. Permanent magnets used in electric machines are invariably parallel magnetized with the magnetic flux lines oriented across the length of each magnet. The magnet length is around 4–7 mm for rare earth magnets and 8–15 mm for ceramic magnets. Fig. 8-4 illustrates the effect of magnetization orientation on back EMF shape. As the magnetic flux lines orientation change from parallel to radial, the back EMF shape proceeds from sinusoidal waveform, found in PMSM, to trapezoidal waveform, existing in BLDC machines [93].

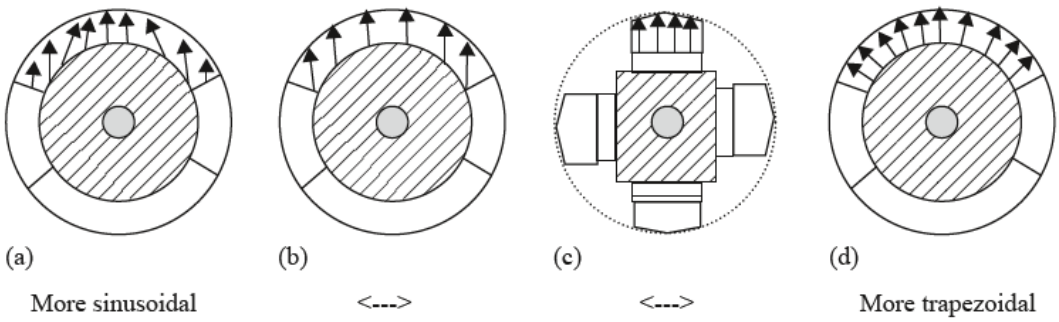

Fig. 8-4. Illustration of PM magnetization orientation:

(a) Halbach, (b) parallel, (c) tapered (bread loaf) and (d) radial [93]

Sinusoidal PMSMs, known as PMSM, are divided further into surface mount (SPM), surface inset, or interior permanent magnet (IPM) types depending on the PMs placement in the rotor as seen in Fig. 8-5. Fig. 8-6 classifies PM machines into the mentioned categories.

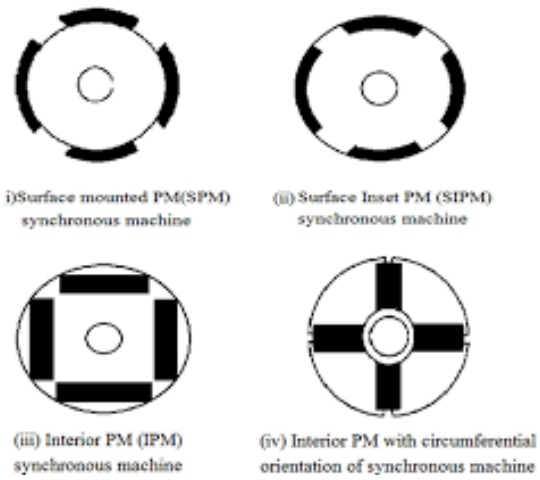

Fig. 8-5. Different types of PMSM rotor construction. (i) Surface PMSM. (ii) Surface inset PMSM. (iii) Interior PMSM. (iv) Interior PMSM with circumferential alignment [121].

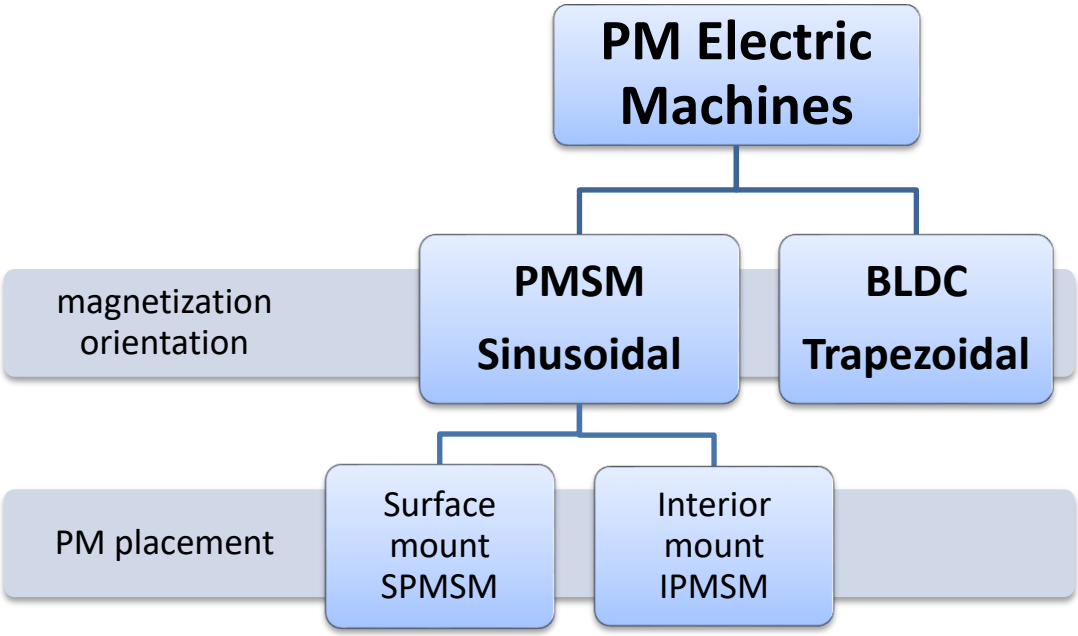

Fig. 8-6. PM machine classification [88]

8.1.2.3.1 IPMSM Saliency feature

As seen in Fig. 8-5, the IPM rotor is different in PM placement than SPMSM. As a result, the q-axis magnetic flux can pass through the steel pole pieces without crossing the PMs. This provides difference in the d- axis and q-axis inductances, which is the saliency feature. The synchronous inductance in d-axis is smaller than that in q-axis for IPMSM. This inductance gap results in additional reluctance torque, in addition to the flux linkage torque produced through the air gap. Moreover, saliency help with field weakening in the constant power region. A wider constant power range without excessive back EMF is easier got the higher the saliency ratio. This is favorable for applications of high frequency high speed like electric vehicles [86].

8.1.3 Operational Characteristics of IPMSM

The voltage equations of the IPMSM at steady state are expressed in d–q frame as:

$$v_{sd} = R_s i_{sd} - \omega L_q i_{sq} \qquad (1)$$

$$v_{sq} = R_s i_{sq} - \omega (L_d i_{sd} - \Psi_m) \qquad (2)$$

Where $\Psi_m$is the air gap flux and is calculated as follow:

$$\Psi_m = 60 \,.\, \text{Line} - \text{to} - \text{line back EMF constant} \,/\, (\sqrt{3}\ .\pi\,.\,p\,.\,1000) \qquad (3)$$

It can be observed from Equations (1) and (2) that a higher voltage is required to increase the speed. The maximum output torque and power developed by PMSM is determined by the maximum current and voltage that the inverter can supply to the motor. The maximum stator voltage is dependent on the DC bus voltage and also on the PWM scheme applied, and it can be expressed as

$$v_{sd}^2 + v_{sq}^2 \le V_{s\,max}^2 \qquad (4)$$

Neglecting the voltage drop due to the stator resistance while merging Equations (1), (2) and (4) leads to the following equation:

$$(\omega L_q i_{sq})^2 + (\,\omega L_d i_{sd} - \omega\, \Psi_m)^2 \le V_{s\,max}^2 \qquad (5)$$

$$\left(\frac{I_{sq}}{L_d/L_q}\right)^2 + \left(I_{sd} + \frac{\Psi_m}{L_d}\right)^2 \leq \left(\frac{V_{s\,max}}{\omega L_d}\right)^2 \qquad (6)$$

For a motor with certain Ψ_m, L_d *and* L_q and for a given $V_{s\,max}$ and ω, Equation (6) represents an ellipse in d–q current frame as shown in Fig. 8-7. This ellipse has properties as follow, as shown in Fig. 8-7,

- The center of the ellipse is located at $(\frac{-\Psi_m}{L_d}, 0)$; $\frac{\Psi_m}{L_d}$ is the PMSM characteristic current.
- The eccentricity of the ellipse can be represented as:

$$e = \frac{\sqrt{b^2 - a^2}}{a} = \frac{\sqrt{(v_{s\,max}/\omega L_d)^2 - (v_{s\,max}/\omega L_q)^2}}{v_{s\,max}/\omega L_d} = \sqrt{1 - \left(\frac{L_d}{L_q}\right)^2} \qquad (7)$$

- The ellipse shrinks inversely with the rotor speed, ω.
- The shape of the ellipse depends on the saliency ratio; $\frac{L_d}{L_q}$.

In addition, the d-and q-axis currents must satisfy:

$$i_{sd}^2 + i_{sq}^2 \leq I_{s\,max}^2 \qquad (8)$$

Equation (8) represents a current circle centered at the origin with a radius of $I_{s\,max}$ as shown in Fig. 8-7. Unlike the voltage-limiting ellipses, current-limiting circles remain constant for any speed.

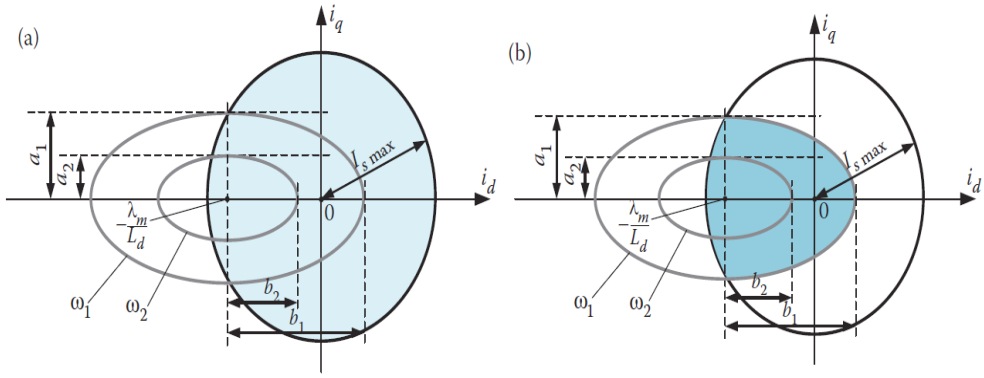

Fig. 8-7. (a) Voltage-limiting ellipses and current-limiting circles for IPM machines and (b) overlap area between voltage limiting ellipses and current-limiting circles [88]

Since both Equations (6) and (8) should be satisfied during the operation. For a given rotor speed, the current vector can be located anywhere inside or on the boundary of the overlap area between the voltage-limiting ellipse and current-limiting circle as shown in Fig. 8-7b. The overlap area becomes smaller when the rotor speed keeps increasing indicating progressively smaller changes for current vector in the flux-weakening region.

Below base speed, where the phase voltage is less than $V_{s\,max}$ for the rated current, the operation of the IPMSM is based on the control of q-axis current as shown in Fig. 8-8a. In the flux-weakening region, negative d-axis current is applied as shown in Fig. 8-8b. This creates a negative voltage vector on the d-axis, which opposes the one induced by the PM flux linkage, so that the motor can speed up. In this case, the stator current vector has both d- axis and q-axis components, and the magnitude of the q-axis current vector reduces resulting in lower torque.

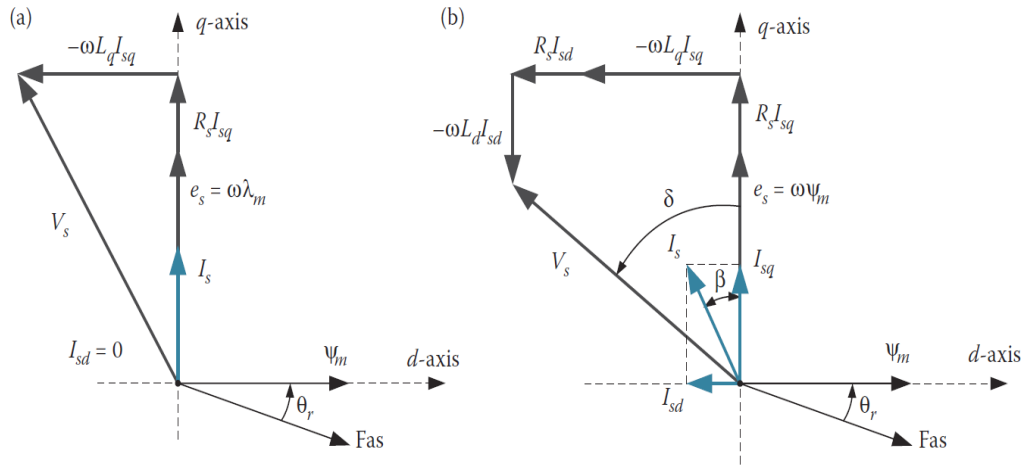

Fig. 8-8. Vector diagrams for IPM machine for (a) speed lower than base speed and (b) speed higher than base speed [88]

8.1.4 Maximum efficiency operation of IPMSM

The maximum torque and output power developed by PM machines is ultimately dependent on the allowable inverter current rating and maximum output voltage that the inverter can supply to the machine. In a PM operating at a given speed and torque, optimal efficiency can be obtained by applying optimal voltage that minimizes the power loss. At low speeds; lower than base speed, this optimum efficiency will coincide with the condition of MTPA control.

8.1.5 Maximum Torque per Ampere (MTPA) Control

MTPA operation of PMSM leads to minimal copper losses in the stator windings and also minimum power loss in the semiconductor switches of the inverter for a given torque demand. The MTPA is based on the following equations. The following couple of equations relates the d-axis and q-axis current components, i_{sd} and i_{sq}, to the stator current vector, magnitude and phase angle

$$i_{sq} = I_s \cos\beta \qquad (9)$$

$$i_{sd} = -I_s \sin\beta \qquad (10)$$

where β is the current phase angle as shown in Fig. 8-8b. The motor developed torque is given as follow

$$T_e = \frac{3}{2}\, p\, (\Psi_m\, i_{sq} + \left(L_q - L_d\right) i_{sq}\, i_{sd} \qquad (11)$$

Combining Equations (8) and (9) with the torque equation in (10) results in:

$$T_e = \frac{3}{2}\, p\, \Psi_m\, I_s \cos\beta + \frac{3}{4}\, p\left(L_q - L_d\right) I_s^2\, \sin 2\,\beta \qquad (12)$$

8

Equations (11) and (12) show that the motor electromagnetic torque has two components. The first term is the excitation torque resulting from the air gap flux. The second term is the reluctance torque component resulting from the rotor saliency. These torque components are proportional to the stator current and its square respectively but vary with this current phase angle β as shown in Fig. 8-9. For β = 0, when no d-axis current component exists, there is no reluctance component but the excitation torque will be maximum. However, maximum reluctance torque component will occur for β = 45°. Therefore, the maximum total torque will be achieved within the range 0 < β < 45°. As mentioned before, Reluctance torque cannot be neglected for IPMSM due to remarkable inductance difference $L_q - L_d$. The current phase angle β, at a certain current I_s. limit, can be controlled optimally using a MTPA algorithm to operate the IPMSM at both high torque and high efficiency.

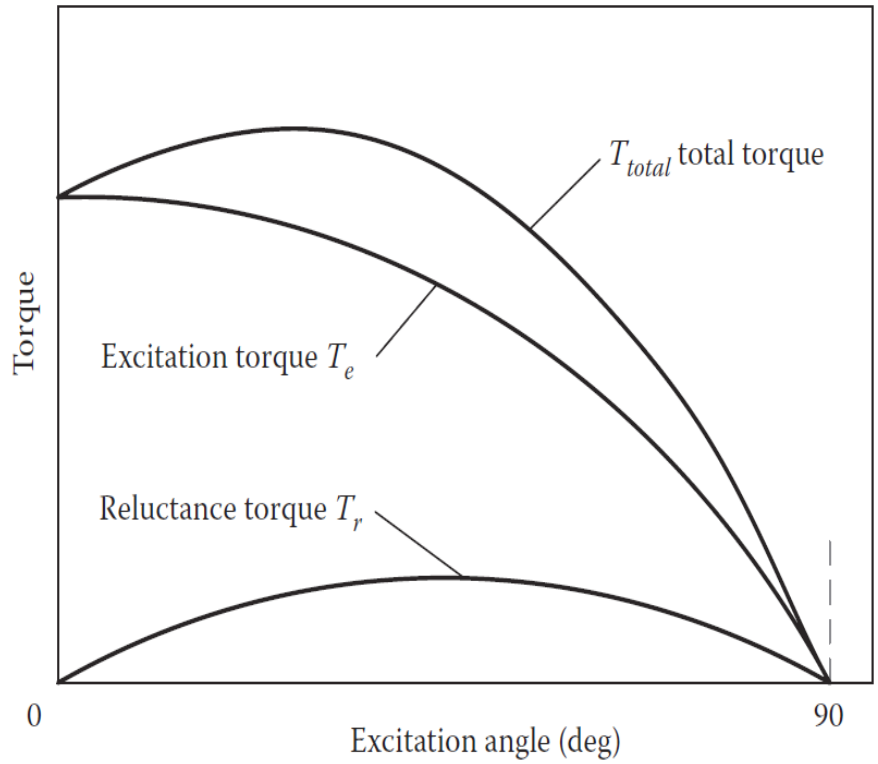

Fig. 8-9. Excitation and reluctance torque components as a function of current phase angle [88]

Using equations (8) to (12), the minimum current magnitude and phase angle corresponding to a given torque can be determined while satisfying the MTPA optimality condition. This is illustrated in Fig. 8-10 which shows the constant torque value line and the corresponding minimum current and phase angle on the d-q coordinates. The minimum current vector shown in Fig. 8-10 for each torque value contribute to the MTPA locus seen in Fig. 8-11. This MTPA locus is dependent on the reluctance torque peak value which is sensitive for variations in L_q and L_d as seen in Fig. 8-12 and Fig. 8-13 respectively. The current vector output of this curve determine the value of the excitation torque component.

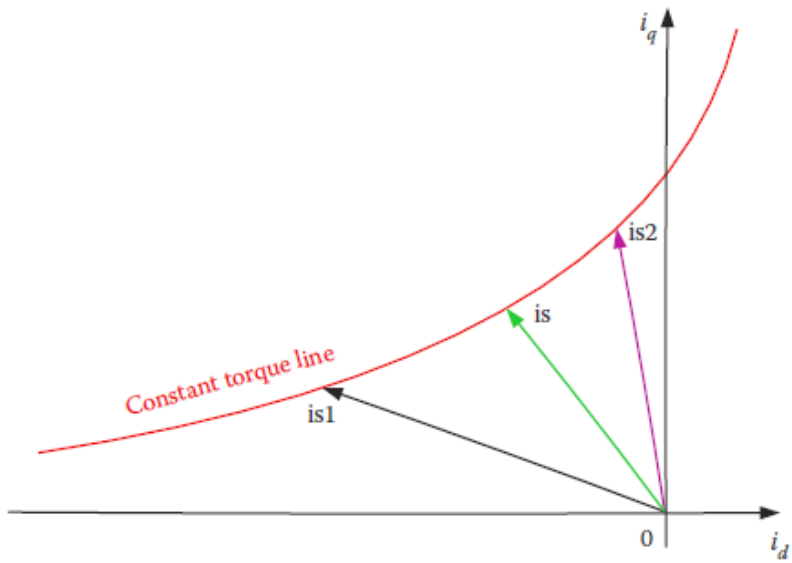

Fig. 8-10. Minimum stator current for a required torque level [88]

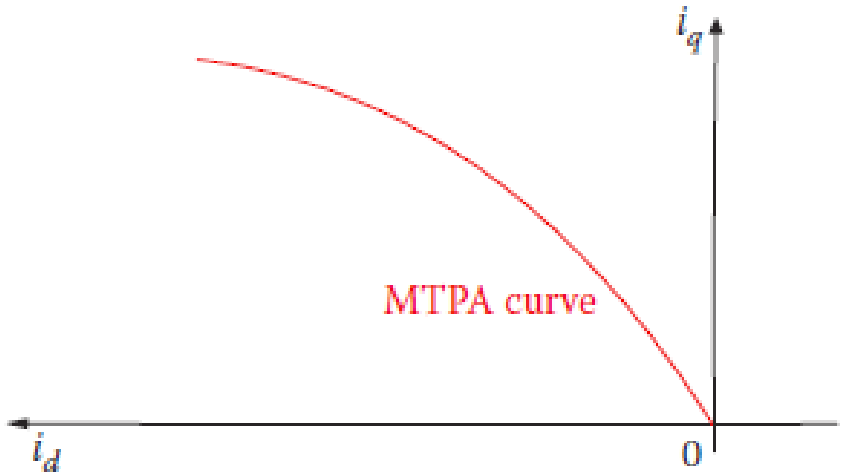

Fig. 8-11. MTPA curve in the d–q plane [88]

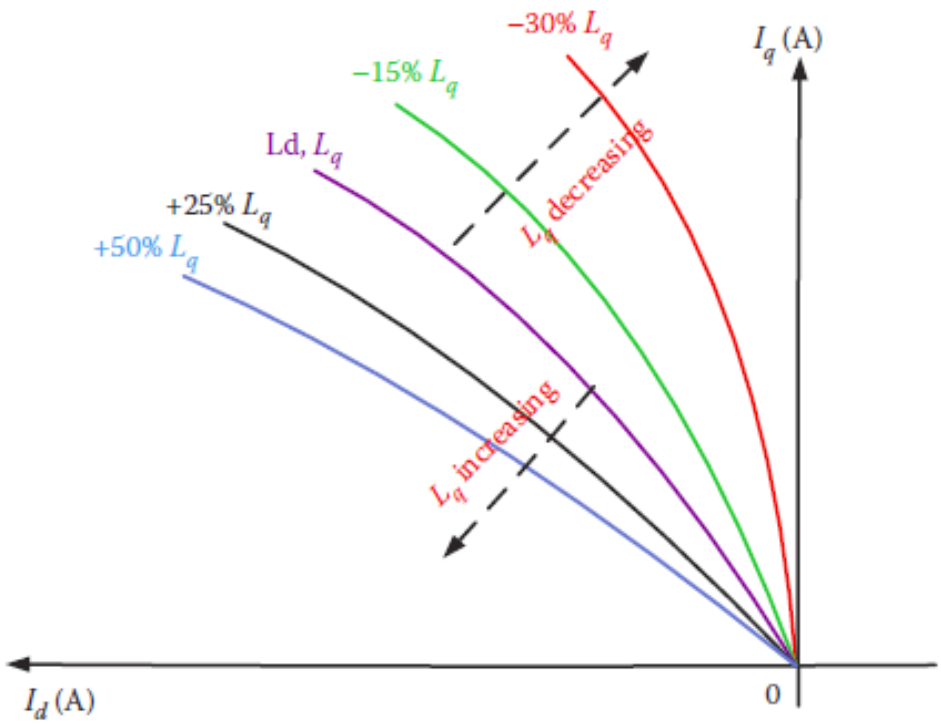

Fig. 8-12. Sensitivity of MTPA curve for variations in L_q [88]

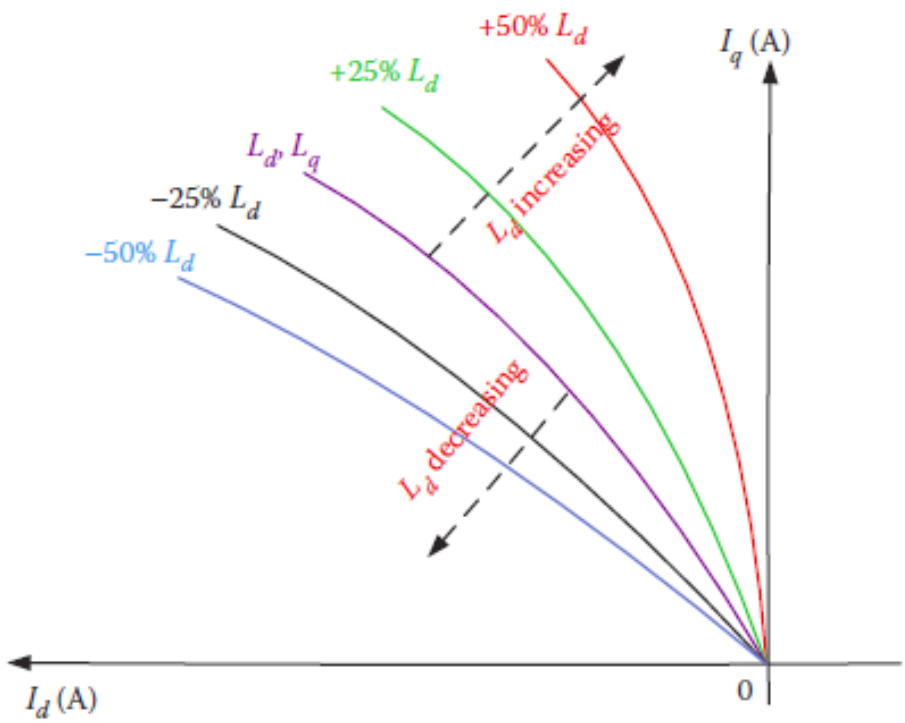

Fig. 8-13. Sensitivity of MTPA curve for variations in L_d [88]

8.1.6 Traction Motor selection

Fig. 8-14 shows the vehicle traction motors' suppliers division between synchronous and asynchronous motors.

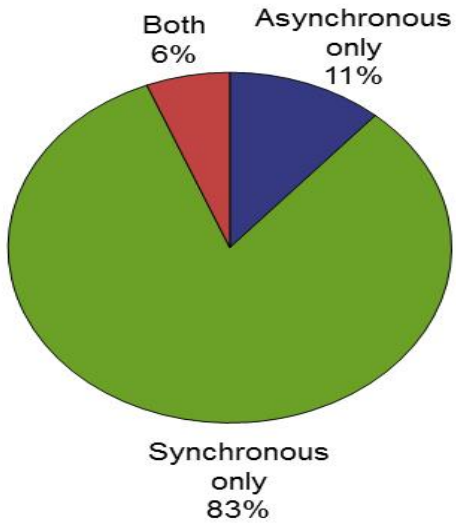

Fig. 8-14. Motor-types sold by suppliers of vehicle traction motors [96]

8.1.6.1 Merits and challenges of PMSM

Today, the PM motor is the common choice for powertrains in HEV and EV [94]. However, some challenges face PM machines. Despite these challenges, PMSMs have many advantages over asynchronous induction motors (IMs). These challenges are:

- Relatively higher costs.
- Uncertainty regarding rare earth PMs availability for wide time horizon [95].

8.1.6.2 PMSM vs IM Comparison

Speaking of technical specifications, comparing a 50 kW copper-rotor IM to a 50 kW PMSM [95] as presented in Table 8-1 leads to the following inferences.

- Torque density: 25% higher.
- Weight: 40% less.
- Peak inverter current: 10-15% less.

Table 8-1. PMSM compared to Cage IM [50 kW] [96]

Permanent Magnet Motor		Copper Rotor Induction Motor
92%	Efficiency	88%
780 W	Stator Copper Loss	940 W
0 W	Rotor Loss	230 W
0 W	Stray Load Loss	140 W
100 W	Iron Loss	180 W
880 W	Total Loss	1490 W
105°C	Coolant Temperature	105°C
2.4 gallons/min	Coolant Flow Rate	2.4 gallons/min
156°C	Maximum Winding Temp	156°C

Fig. 8-15 represents a comparison between loss of PMSM and IM in railway traction by Toshiba [97]. The IM under comparison is of 120 kW output power and manufactured in 1996. On the other hand of the comparison, the PMSM is manufactured in 2009 with 120 kW output power too. Fig. 8-16 summarizes Toshiba's comparison between the energy consumption of the two motors.

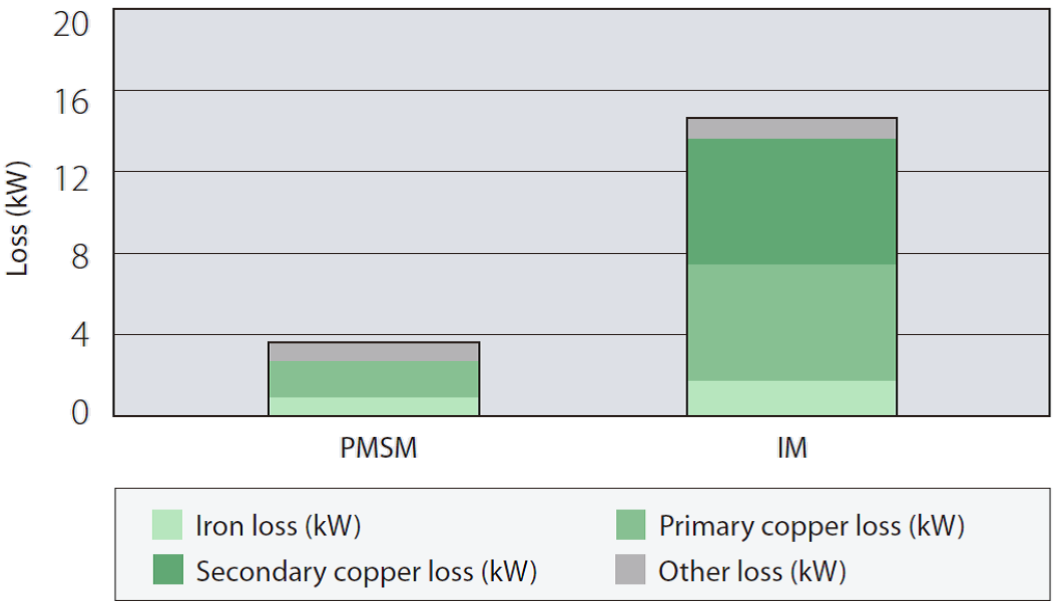

Fig. 8-15. Comparison between loss of PMSM and IM in railway traction [97]

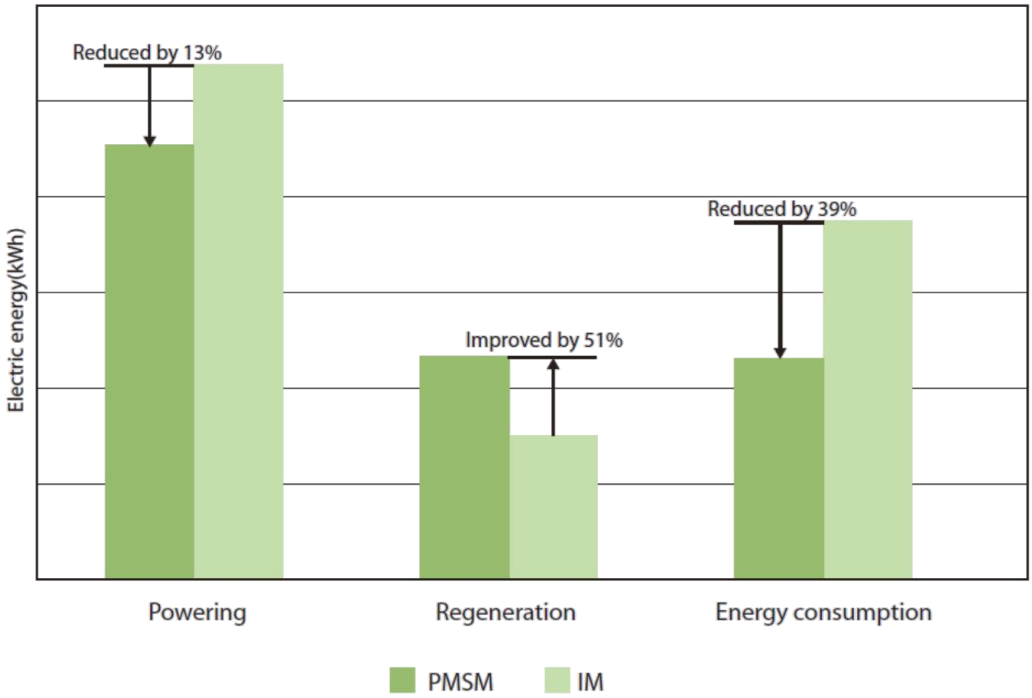

Fig. 8-16. Comparison between energy consumption of PMSM and IM [97]

8.2 DC-DC Converter

DC/DC converter enables the generation of a controlled output dc voltage from any input dc voltage. In other words, using a DC/DC converter gives the possibility to transform a dc input voltage into a different DC output voltage. According to the used converter (Boost, Buck, and Buck–Boost), the input voltage can be either stepped up or stepped down. In an electrified vehicle, a high-voltage battery is conventionally used as the electrical energy source of the vehicle. This battery can be sized differently according to the type of vehicle. The more the battery capacity, the more the electrical energy that can be stored within the vehicle and used to power it. i.e. the higher car mileage. In some cars, the battery is directly connected to the traction inverter. In this configuration, battery output is imposed to the drive system, which can be, in some cases, a constraint as it limits the performances of the electric motor (especially in terms of maximum speed). To avoid this, other configurations have a DC/DC converter between the battery and the traction inverter. The DC/DC converter steps up the battery voltage to obtain the required DC bus voltage. [98]

8.3 Li-Ion Battery

Electric vehicles require different energy storage devices to run, and this will fuel the demand for advanced batteries in the future. The following section discuss EV battery market.

8.3.1 Market Overview

The current Electric Vehicles (EV) market Rechargeable batteries held a share of approximately 76% of the total batteries market in 2011, and primarily included include Li-ion batteries, Nickel Metal Hydride (NiMH) batteries, and Nickel Cadmium (NiCd) batteries. Li-ion batteries are currently dominating the energy storage market compared to the other two nickel-based batteries, as they are the most modern technology in the market, offering higher energy density and better performance than other battery types. [99]

Two battery types are preferred for EVs, Nickel Metal Hydride (NiMH) and Lithium Ion. The following are their main characteristics. [100]

- NiMH main characteristics
    - Introduced near end of 20th century.
    - Similar performance to NiCad battery but its energy and power densities are higher and it charges faster.
    - The metals into which hydrogen is adsorbed are proprietary.
    - The cell must be sealed in order to keep air from reacting with the hydride.
    - Battery can require cooling if charged fast.
- Lithium Ion (Li-ion) main characteristics
    - Introduced in early 1990s.
    - Precise voltage control is needed when charging battery because if too high, battery can be damaged and if too low, battery will be undercharged.
    - Because of its considerable weight advantage over other battery types, it is highly attractive for future hybrid electric vehicles.
    - Large batteries are prohibitively expensive.

8.3.2 Superiority of Li-ion Batteries

The basic performance (energy density, power density, etc.) of a battery including the voltage is determined almost entirely by the combination of metals used in the cathode and anode.

Comparing voltages, as seen in Fig. 8.17, the lead-acid storage battery used in vehicles has a voltage of 2V with a combination that includes the use of lead dioxide in the cathode and lead in the anode. (Vehicles use 12 V batteries that are configured by connecting six of these 2 V batteries in a series.) NiCad (Ni-Cd) batteries have a voltage of 1.2 V using a combination of nickel hydroxide in the cathode and cadmium hydroxide in the anode, and nickel-metal hydride (Ni-MH) batteries have a voltage of 1.2 V using a combination of nickel hydroxide in the cathode and a hydrogen storage alloy in the anode.

In contrast, the voltage of lithium-ion batteries is in a range of 3.2~3.8V, which means that a voltage that is three times higher than that of NiCad batteries and Ni-MH batteries can be obtained.

Fig. 8-17. Li-ion cell has a voltage 3 times that of Ni based cells [101]

In addition, the energy density of lithium-ion batteries is also superior, as seen in Fig. 8.18, with a volume energy density that is roughly 1.5 times that of Ni-MH batteries and a weight energy density that is roughly double. Therefore, if the batteries are of the same capacity, the rechargeable lithium-ion battery can be fabricated with a more compact, lightweight design with just two-thirds the volume of the Ni-MH battery and half the weight. [101]

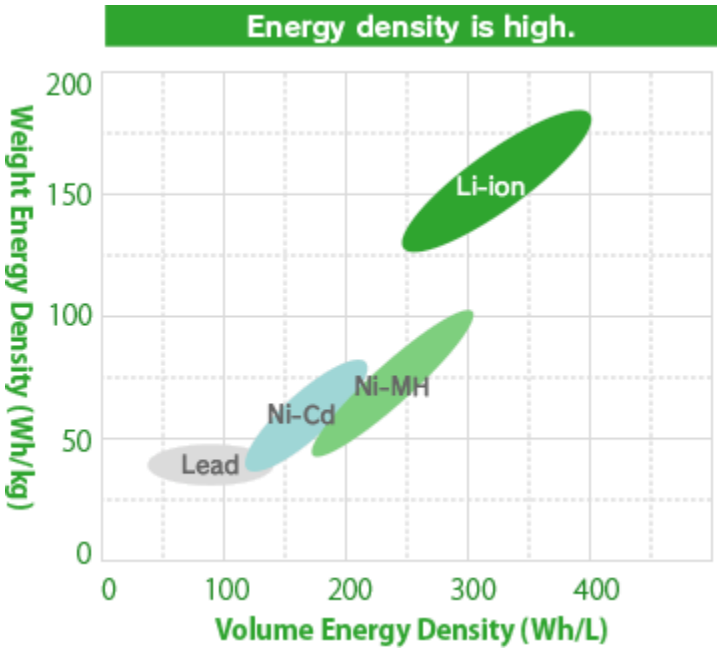

Fig. 8-18. Energy density of lithium-ion batteries compared to other types [101]

8.3.3 Future of EV batteries

Bosch has presented its current solid-state during 2015 at the Frankfurt Motor Show, according to recent reports, claiming that the new solid-state battery cells could double energy density, while actually lowering costs, not increasing them. The company claims that these electric vehicle (EV) batteries could be ready for production in only 5 years, or less. [102]

Chapter 9 : Appendix II: Nissan Leaf components

The Electric powertrain's main components of motor and inverter were developed by Nissan in order to withstand use in a variety of environments around the world, implementing high performance and high durability. Further, from 2013 onward, Nissan LEAF was upgraded with the main components integrated into one unit, making for a lighter and more compact e-Powertrain [73].

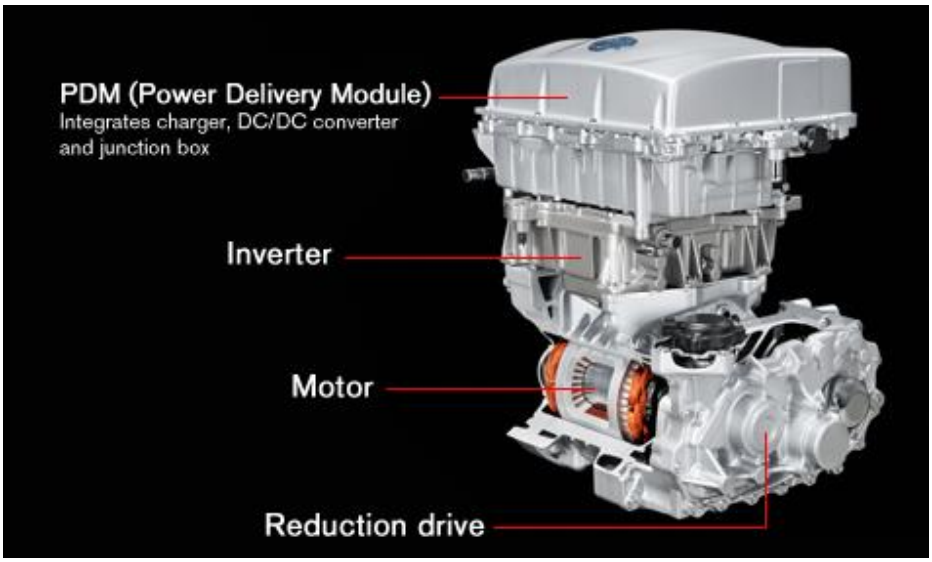

Fig. 9-1. Compact electric powertrain of NLEV [73]

Fig. 9-2. NLEV battery module from AESC [101]

Fig. 9-3. NLEV battery pack from AESC [101]

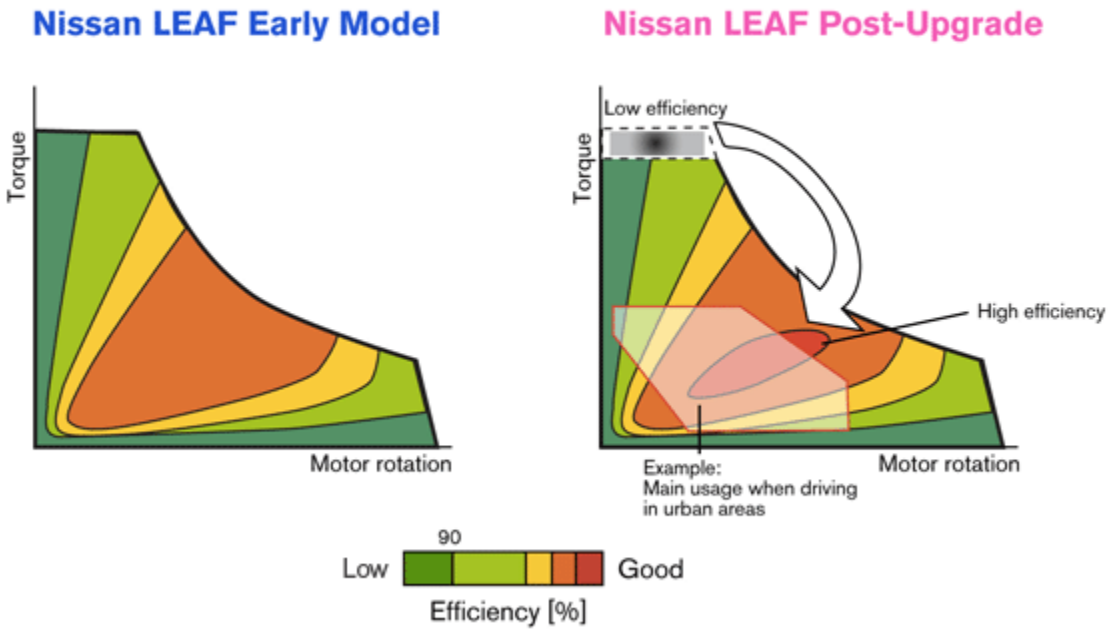

Fig. 9-4. The NLEV efficiency mapping on the Torque-Speed characteristics [73]

Chapter 10 : Appendix III: ART components in Vancouver

Fig. 10-1. Vancouver's ART, SkyTrain [122]

Fig. 10-2. MITRAC TC 1410 – Traction Converter for ART [103]

Fig. 10-3. Kokam Intelligent Battery module for ART [78]